

Visualising Feature Learning in Deep Neural Networks by Diagonalizing the Forward Feature Map

Yoonsoo Nam

*Department of Theoretical Physics
University of Oxford*

Chris Mingard

*Department of Theoretical Physics/Department of Chemistry
University of Oxford*

Seok Hyeong Lee

*Center for Quantum Structures in Modules and Spaces
Seoul National University*

Soufiane Hayou

*Simons Institute
UC Berkeley*

Ard Louis

*Department of Theoretical Physics
University of Oxford*

YOONSOO.NAM@PHYSICS.OX.AC.UK

CHRISTOPHER.MINGARD@QUEENS.OX.AC.UK

LSHYEONG@SNU.AC.KR

HAYOU@BERKELEY.EDU

ARD.LOUIS@PHYSICS.OX.AC.UK

Abstract

Deep neural networks (DNNs) exhibit a remarkable ability to automatically learn data representations, finding appropriate features without human input. Here we present a method for analysing feature learning by decomposing DNNs into 1) a forward feature-map $\Phi : \mathcal{X} \rightarrow \mathbb{R}^p$ that maps the input dataspace \mathcal{X} to the p post-activations of the penultimate layer, and 2) a final linear layer that classifies the data. We diagonalize Φ with respect to the gradient descent operator and track feature learning by measuring how the eigenfunctions and eigenvalues of Φ change during training. Across many popular architectures and classification datasets, we find that DNNs converge, after just a few epochs, to a minimal feature (MF) regime dominated by a number of eigenfunctions equal to the number of classes. This behaviour resembles the neural collapse phenomenon studied at longer training times. For other DNN-data combinations, such as a fully connected network on CIFAR10, we find an extended feature (EF) regime where significantly more features are used. Optimal generalisation performance upon hyperparameter tuning typically coincides with the MF regime, but we also find examples of poor performance within the MF regime. Finally, we recast the phenomenon of neural collapse into a kernel picture which can be extended to broader tasks such as regression.

1. Introduction

The pioneers of deep learning designed deep neural networks (DNNs) with layer-wise modules, crafted to automatically learn representations of the raw data that can easily be separated with a relatively small final linear layer [LeCun et al., 2015; Schmidhuber, 2015; Bengio et al., 2013]. In Figure 1(a) we schematically depict this basic architecture, which is shared by most DNNs. DNNs are characterised by their feature maps Φ , which create a non-linear transformation from the data space \mathcal{X} into a representation \mathbb{R}^p : which are the post-activations of the penultimate layer. These, in turn, serve as the inputs (or features) for the final linear layer. Most DNNs share this abstract structure and differ mainly in how they create their feature maps. Examples of feature maps include a series of fully-connected layers, as in an FCN, a combination of convolutional and pooling layers, as in a CNN [LeCun et al., 1989], including very deep CNNs such as a VGG [Simonyan and Zisserman, 2014], or a combination of convolutional layers and skip connections, as in a ResNet [He et al., 2016], or an encoder-decoder architecture, as in the original transformers [Vaswani et al., 2017], and many more. Within this simple schema, feature learning can be defined as any changes in the feature map Φ due to the training process.

It is also possible to fix the feature map – by randomly selecting its parameters – and to only learn the final layer weights. Since only the last layer can be trained, such a network is typically much less expressive than a standard DNN of the same width. In order to reach zero training error, the final layer for a frozen

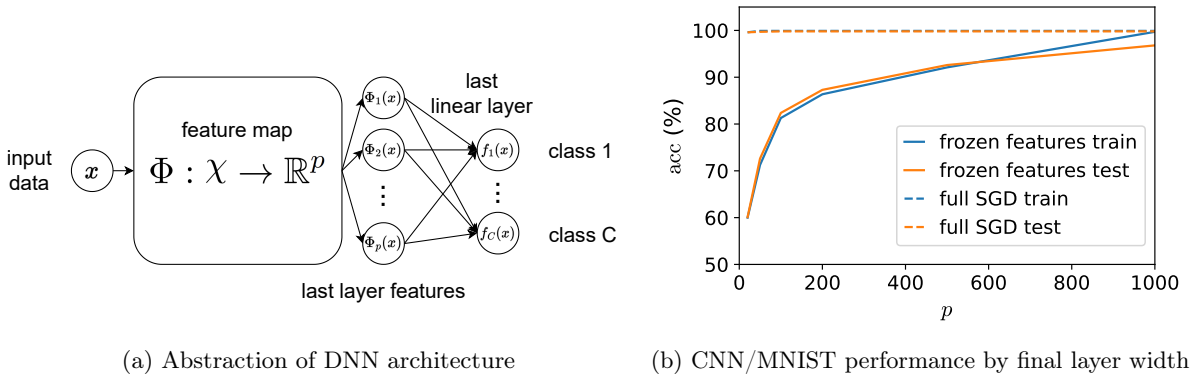


Figure 1: **A DNN can be decomposed into a feature map and a linear last layer of width p**

(a) An abstract diagram depicting a DNN architecture as a combination of the forward feature-map $\Phi : \mathcal{X} \rightarrow \mathbb{R}^p$ from the input dataspace \mathcal{X} to the p inputs of the final layer, and a final linear classifier for C -way classification. Within this picture, we define feature learning (Definition 1) as any change to the feature map Φ upon training, reflected in changes to the p ‘features’ compared to initialization. An important aspect of modern DNN practice is that the final layer is typically small compared to the training set size n so that zero training error can only be reached by changing Φ , that is by feature learning. (b) Training (blue) and test error (orange) for a 5-layer CNN on the full MNIST dataset as a function of the width p of the final linear layer for the case of no feature-learning, where the feature map fixed (frozen) at initialization (solid lines) and for standard SGD with backpropagation on all layers (dashed lines). For this simple example, one still needs a final layer of at least $p = 1,000$ to achieve zero training error with a fixed feature map, whereas if full feature learning is allowed, a width of just $p = 20$ is sufficient. For more complex datasets, much wider final widths, closer in size to the training set size n , would be needed for a random (frozen) feature map to achieve zero training error.

feature map must be significantly wider than what is typical of DNNs in modern practice. For example, in Figure 1(b) we show that even for the relatively simple task of separating the training set of the MINST image dataset, a CNN with fixed random convolutional layers needs a width of at least $p = 1000$ to obtain zero training error. For more complex datasets, much wider layers are needed to achieve zero training error for frozen feature maps. For CIFAR10, for example, widths on the order of $p \approx n$ are needed to achieve zero training error for a frozen feature map (see Appendix A). By contrast, if the hidden layers are allowed to change under training, i.e. if feature-learning is allowed, then a width of just $p = 20$ is sufficient to achieve zero training error for MNIST, and very modest final layers can achieve this for more complex datasets. In other words, the practice of choosing a relatively narrow final layer with $p \ll n$ and training to zero-training error or small loss means the DNN must learn new representations in the hidden layers that are relatively easy to linearly separate by the final layer.

The ability of DNNs to automatically feature learn has long been thought to play a key role in the impressive performance of DNNs over a wide range of tasks [Bengio et al., 2013; LeCun et al., 2015; Schmidhuber, 2015; Simonyan and Zisserman, 2014; Goodfellow et al., 2014; He et al., 2016; Devlin et al., 2018]. On the other hand, more recent work investigating the infinite width limits of DNNs, where they can reduce to a Gaussian process (NNGP) [Neal, 1994; Lee et al., 2018; Matthews et al., 2018] or a Neural Tangent Kernel (NTK) [Jacot et al., 2018] has also demonstrated impressive performance on some key model tasks [Lee et al., 2020; Arora et al., 2019]. Since these are limits where no feature learning occurs, this good performance complicates the hypothesis that feature learning is a necessary characteristic of DNNs. The theoretical simplifications that these infinite width limits bring has stimulated a great deal of research see e.g. [Allen-Zhu and Li, 2019; Daniely and Malach, 2020; Refinetti et al., 2021; Lee et al., 2020; Arora et al., 2019; Ba et al., 2022; Atanasov et al., 2021; Damian et al., 2022; Jacot et al., 2022; Malach et al., 2021; Mousavi-Hosseini et al., 2022; Daniel A. Roberts, 2021; Mei et al., 2018; Rotskoff and Vanden-Eijnden, 2018; Chizat et al., 2019; Geiger et al., 2020, 2021; Yang and Hu, 2021; Yang et al., 2021; Naveh and Ringel, 2021; Bordelon and Pehlevan, 2022, 2023; Vyas et al., 2022; Petrini et al., 2023; Seroussi et al., 2023; Vyas et al., 2023]. Nevertheless, although state-of-the-art (SOTA) performance for most tasks is still achieved by a suitably optimised finite-width DNN where feature learning must occur in order to reach low training errors, the precise role that feature learning plays in optimising the generalisation performance of DNNs remains an open question.

While to 1st order, the idea that changes in the feature map Φ under training signal feature learning is widely shared, there are many different proposals in the literature for how to measure and quantify this phenomenon. These include direct visualization of hidden layer representations [Zeiler and Fergus, 2014; Girshick et al., 2014; Molnar, 2020], or measuring changes to certain kernels that should be constant without feature learning such as the NTK [Jacot et al., 2018; Atanasov et al., 2021] and the forward feature kernel [Yang and Hu, 2021; Canatar and Pehlevan, 2022]. The learned representations, or features, are exploited in algorithms such as Google Deep Dream [Mordvintsev et al., 2015], style transfer [Jing et al., 2019], and transfer learning more broadly [Weiss et al., 2016]. Sometimes, these features are human-interpretable, as is thought to be the case for CNN filters (see [Goodfellow et al., 2016], for example).

We begin by considering the simpler case of linear models, where features are mathematically well-defined as the basis functions in which one expands the learned function. To be more precise, any datapoint of an input dataspace, $x \in \mathcal{X}$ can be mapped to a vector or tensor (e.g. vectors of tokens) via a feature map $\Phi : \mathcal{X} \rightarrow \mathbb{R}^p$. Then, a linear model can be defined with respect to the parameters θ as:

$$f(x) = \sum_{k=1}^p \theta_k \Phi_k(x), \quad x \sim q, \quad \Phi : \mathcal{X} \rightarrow \mathbb{R}^p, \quad (1)$$

where q is the true distribution of the data, p is the number of parameters of the linear model, and $\Phi_k(x)$ is the k^{th} entry of the feature vector. Since the features $\Phi_k(x)$ are fixed for linear models, the training task simply means learning the coefficients θ_k .

Next, we note that the linear formalism of Equation (1) can also be used to describe a snapshot of a DNN at a given time during the training process where θ_k are the parameters of the last layer (for simplicity we have ignored bias terms), and $\Phi(x)$ is its feature-map at that time, which outputs the post-activations of the penultimate layer of the DNN. The difference with the linear model is that a DNN can go beyond merely learning the coefficients θ_k and change the features $\Phi_k(x)$ upon further training, as illustrated, for example, in Figure 2.

Since DNNs are typically trained with stochastic gradient descent (SGD), we diagonalize the feature map $\Phi(x)$ at any given time-step with respect to the gradient descent (GD) operator, and define features at each time-step in terms of the eigenfunctions of this operator. We visualise and quantify feature learning by monitoring changes to projection operators of the eigenfunctions onto the target function and the learned function, and changes to the eigenvalue spectrum under training. Formal definitions and further details of these measures are given in the next section.

There are, of course, many other ways to analyse how DNNs learn features besides the schema depicted in Figure 1(a). In particular, this method ignores the details of how the features evolve in earlier layers (see however Appendix D) that make up the feature map. However, defining features in terms of the forward-feature map, as we do here, abounds in the literature. Moreover, our measures are computationally relatively efficient to calculate, allowing us to empirically explore feature learning from initialization to convergence for a set of popular DNN architectures (FCN, CNN, ResNet18, and VGG) and image datasets (MNIST, CIFAR-10, and CIFAR100), and for different hyperparameters.

1.1 Our contributions

1. We introduce a computationally efficient method for monitoring feature learning in DNNs, based on projections of eigenfunctions of the forward feature-map Φ on the target function and the learned function, as well as measures of the effective dimension of the eigenvalue distribution (Section 2).
2. We distinguish coefficient learning, when no feature learning occurs and only final layer parameters are learned, from a minimal feature (MF) regime (where the number of features describing the learned function equals the number of classes) and an extended feature (EF) learning regime that covers behaviour between the two extremes (Section 2).
3. We find that upon increasing the training set size n , feature learning can change from the EF regime to the MF regime. Moreover, the scaling exponent of the test error and loss with training set size n increases upon the emergence of the MF regime from the EF regime (Section 3.1).
4. We show that the MF regime can arise early in training, even after just a few epochs (Section 3.2).
5. We find that multiplying the output by a constant, as is done to enter the so-called lazy regime—where DNN training can be described by a linear model [Chizat et al., 2019; Geiger et al., 2020; Bordonon

and Pehlevan, 2022; Petrini et al., 2023]—shifts feature learning from the MF regime to the EF regime for typical DNN widths where $p \ll n$. To completely eliminate feature learning, DNNs must be much wider, with $p \gtrsim n$ for more complex datasets (Section 3.3).

6. Our measures allow us to visualise and analyse the quality of features in the context of transfer learning (Section 3.4)
7. We find that the MF regime can be obtained even on random data, suggesting that its origin lies in the training dynamics (Section 4.1).
8. Upon hyperparameter tuning, we find that typically, but not always, a tighter MF regime gives better performance (Section 4.2).
9. An important body of recent work has shown that for balanced classification problems, the penultimate layer post-activations can collapse to a symmetric and geometrically simple minimal representation, typically upon overtraining well past zero training error. This phenomenon has been called neural collapse (NC) [Papayan et al., 2020; Han et al., 2021] and is closely related to our MF regime. We introduce a minimum projection operator with which we can analyse the phenomenon of NC within a kernel picture. This formalism allows us to extend the concept of NC to regression (Section 5).

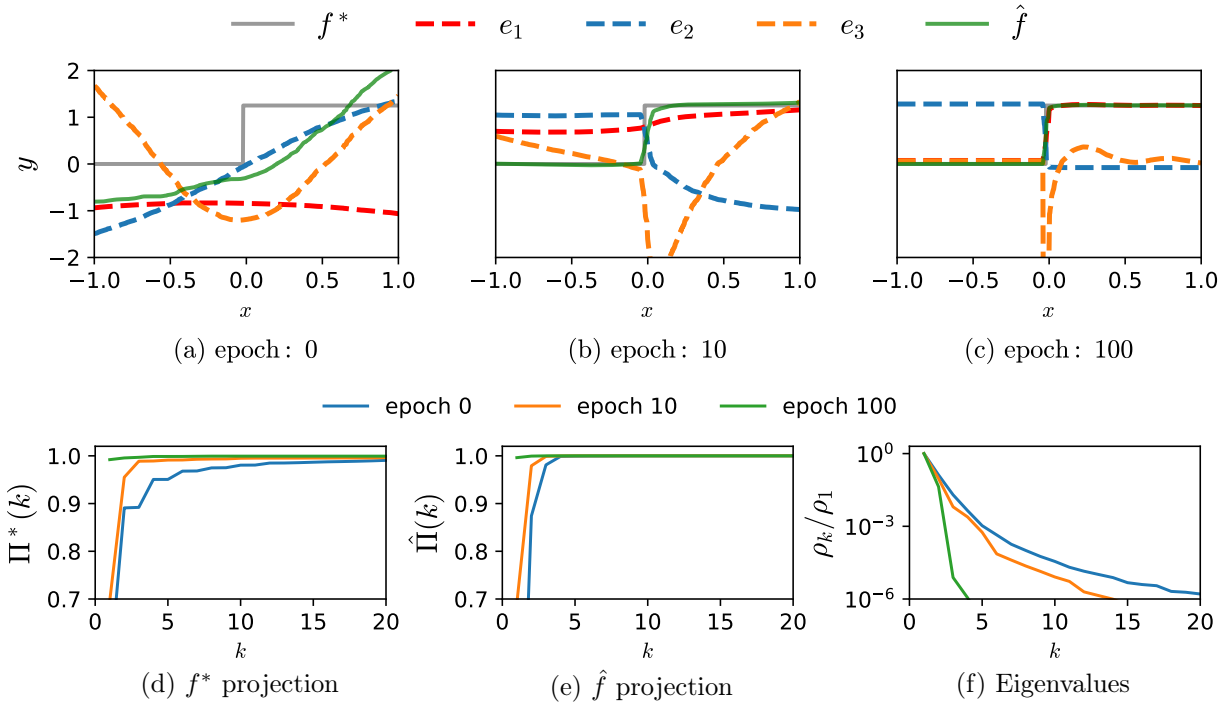


Figure 2: **Toy model demonstrating feature learning by a DNN** A 4-layer FCN with width 1000 and scalar input and output, is trained to learn the Heaviside step function f^* over the domain $[-1, 1]$. (a) At initialization (epoch 0), the first three eigenfunctions e_i (dashed) of the feature map Φ are shown in order of their eigenvalues. If Φ and thus the features are fixed, about 20 features are needed to accurately approximate the target function f^* (solid grey) to an MSE loss less than 10^{-5} . (b,c) During training with SGD, the DNN learns new features with better quality Q_K^* , greatly reducing the number needed to express the target function f^* and the learned function \hat{f} . To visualise how feature learning develops with epochs during training, the target function f^* (d), and the learned function \hat{f} (e), are projected onto the first k eigenfunctions using Equation (7) and Equation (9) respectively, illustrating that fewer features are needed after training. (f) The eigenvalues ρ_i decay significantly faster post-training.

2. Definitions and methodology

In this section, we define the series of measures we will use to quantify and visualise feature learning, and explain how to calculate them efficiently. Then, we illustrate how our measures work using two simple examples, a toy FCN on a 1-dimensional function, where the full eigenfunctions can be visualised, and a CNN on MNIST with large enough p so that both coefficient learning and SGD on all layers can reach zero training error.

2.1 Feature learning and coefficient learning

As illustrated in Figure 1(a), a DNN can be decomposed into a forward feature map $\Phi : \mathcal{X} \rightarrow \mathbb{R}^p$ that maps the raw data (e.g. an image) to a p -dimensional vector, and a final linear layer of finite width p . We will assume the data $x \in \mathcal{X}$ are sampled from a true distribution q (i.e. $x \sim q$). From this simple decomposition it follows that feature learning occurs when the forward feature map changes. More formally:

Definition 1 (Feature learning). *A DNN is said to undergo feature learning if at any time t during training, $\Phi_{(t)} : \mathcal{X} \rightarrow \mathbb{R}^p$ differs from the forward feature map $\Phi_{(0)}$ at initialization ($t = 0$). The feature maps are considered distinct if there exists an $x \in \mathcal{X}$ such that $\Phi_{(0)}(x) \neq \Phi_{(t)}(x)$.*

From this definition, it follows that if the feature map Φ remains fixed and does not change during training, no feature learning takes place. In this case, only the coefficients (parameters) of the final linear layer are adjusted during training, a scenario we define as follows:

Definition 2 (Coefficient Learning). *A DNN is said to undergo coefficient learning if the forward feature map $\Phi_{(t)} : \mathcal{X} \rightarrow \mathbb{R}^p$ remains fixed at all times t during training such that $\forall x \in \mathcal{X}, \Phi_{(0)}(x) = \Phi_{(t)}(x)$. In this case, no feature learning occurs, and only the parameters (coefficients) of the final linear layer of the DNN are updated during training.*

Coefficient learning occurs in the much-studied case of random features, where the parameters of Φ are set by a random sample over a distribution, and then not allowed to change under training. In the infinite width limit, it is equivalent to taking a sample from the NNGP [Radhakrishnan, 2022].

2.2 Features from the eigenfunctions of forward feature map

To define features, we begin by calculating the eigenfunctions $e_k : \mathcal{X} \rightarrow \mathbb{R}$ and eigenvalues ρ_k of Φ using a standard analysis from the kernel literature [Smola and Schölkopf, 1998; Williams and Rasmussen, 2006] in terms of the integral operator $T : L^2(\mathcal{X}) \rightarrow L^2(\mathcal{X})$:

$$T[f](x') := \int_{\mathcal{X}} \Phi(x)^T \Phi(x') f(x) q(x) dx, \quad T[e_k] = \rho_k e_k, \quad (2)$$

where $\langle e_i | e_j \rangle = \delta_{ij}$, and the bra-ket notation in $\langle \cdot | \cdot \rangle$ denotes the L^2 inner product defined on measure q (i.e. $\langle f | g \rangle = \int_{\mathcal{X}} f(x) g(x) q(x) dx$). The integral operator T and its eigenfunctions $[e_1, e_2, \dots, e_p]$ are of particular interest because T diagonalizes the dynamics of the linear model trained with gradient descent (GD) and mean square error (MSE) loss¹. Then the learning dynamics decompose into p independent dynamical equations, one for each eigenfunction:

$$f(x) = \sum_{k=1}^p \langle f | e_k \rangle e_k(x), \quad \langle f | e_k \rangle (t) = \langle f^* | e_k \rangle (1 - e^{-\eta \rho_k t}). \quad (3)$$

Here, we have assumed that all coefficients $\langle f | e_k \rangle$ are initialized to zero at $t = 0$, and that the MSE loss is calculated with respect to a target function $f^*(x)$. Note that for fixed Φ , the speed at which each coefficient $\langle f | e_k \rangle$ is learned depends on the eigenvalues ρ_k and the learning rate η of the GD algorithm used. The larger the eigenvalue, the faster the coefficient is learned.

In the context of a DNN, the dynamics of Equation (3) describe what would happen if one were to fix at a given time t' , the hidden layers, and thus the feature map $\Phi_{(t')}(x)$ (with eigenfunctions e'_k), and subsequently train only the final layer. This picture is equivalent to interpreting the feature map at $t = t'$ as the one fixed at initialization so that there is no feature learning, and the DNN only learns the coefficients $\langle f^* | e'_k \rangle$

1. Technically, these equations are obtained under a continuous limit of gradient flow. For completeness, we provide a full derivation of the dynamics of linear models in Appendix E

(although we might hope $\Phi_{(t')}(x)$ is better than $\Phi_{(t)}(x)$). Indeed, Equation (3) describes the full dynamics of learning the coefficients for GD with MSE loss under the coefficient learning regime from Definition 2.

DNNs are not normally trained with a fixed feature map. Indeed, since DNNs are non-linear, they can change their feature maps by parameter updates in the intermediate layers, making Φ , and therefore also the eigenfunctions and eigenvalues defined in Equation (2), time-dependent. This suggests we can monitor (non-linear) feature learning by analysing changes in the eigenvalues and eigenfunctions defined by the above procedure. Within this picture, it is therefore natural to formally define our features as follows:

Definition 3 (Features). *Given the true data distribution q and a forward feature map $\Phi : \mathcal{X} \rightarrow \mathbb{R}^p$ mapping data to the input of the last layer of DNN, the p eigenfunctions $[e_1, e_2 \dots e_p]$ of the feature map are obtained by diagonalizing the integral operator T in Equation (2). These eigenfunctions are indexed in descending order according to their corresponding eigenvalues ρ_k . The k^{th} feature is defined as a scalar-valued function on the input probability space, denoted as $e_k(x)$ for $x \sim q$. Since x is normally chosen at random, the features are scalar random variables.*

An intuitive way of thinking about this definition of the k^{th} feature is as a linear combination of the p entries of the input to the final layer, chosen such that it reflects the natural direction of the data after the transform via the feature-map Φ , similar in spirit to how SVD finds the ‘‘natural direction’’ of the matrix. Variations of the definition above are also possible, see Appendix B.

2.3 Measuring feature learning by projecting onto the learned function and the target function

While using Definition 3 for features has certain practical advantages which we will explore further in this paper, the eigenfunctions (features) are typically hard to visualise directly for high-dimensional problems. To make progress in analysing and visualising feature learning, we will define measures based on projecting the eigenfunctions onto either the target function f^* , which describes the target function on all the data $x \in \mathcal{X}$, or else the learned function \hat{f} that the DNN expresses once training on a training set $S_{tr} \in \mathcal{X}$ is complete.

Before defining our measures, we note that for the sake of simplicity, we considered DNNs with scalar output functions f in the previous sections. For a balanced C -way classification task, the target function is a vector function (i.e. $f^* : \mathcal{X} \rightarrow \mathbb{R}^C$), and the dataspace \mathcal{X} can be partitioned into subspaces $\{A_1, \dots, A_C\}$ by class. The components $f_i^* : \mathcal{X} \rightarrow \mathbb{R}$ for $i \in [1, \dots, C]$ of $f^* = [f_1^*, \dots, f_C^*]$ can be written down as:

$$f_i^*(x) = \mathbf{1}_{A_i}(x) \quad (A_i = \{x : x \text{ is in class } i\}) \quad (4)$$

where $\mathbf{1}_{A_i}$ is the indicator function for A_i . Note that because all the classes are mutually exclusive, we have

$$\langle f_i^* | f_j^* \rangle = \int_{\mathcal{X}} f_i^*(x) f_j^*(x) q(x) dx = \frac{1}{C} \delta_{ij}, \quad (5)$$

where the C^{-1} on the right-hand side comes from the probability measure for each class i . Then it follows that at least C orthogonal scalar output functions are needed to express f^* . We define the target function space \mathcal{H}^* as the function space spanned by $[f_1^*, \dots, f_C^*]$.

Given a C -class vector target function f^* and a projection operator $P_{\mathcal{H}^*} : L^2(\mathcal{X}) \rightarrow L^2(\mathcal{X})$ onto the target function space \mathcal{H}^* , we define the *quality* Q_k^* of a feature e_k as follows:

$$P_{\mathcal{H}^*}[g] := \sum_{j=1}^C \frac{1}{\|f_j^*\|^2} |f_j^* \rangle \langle f_j^* | g \rangle, \quad Q_k^* := \frac{\langle e_k | P_{\mathcal{H}^*}[e_k] \rangle}{C} = \sum_{i=1}^C \langle e_k | f_i^* \rangle^2. \quad (6)$$

The range of Q_k^* is given by $0 \leq Q_k^* \leq C^{-1}$. We use the word quality because Q_k^* measures how much e_k overlaps with the C dimensional target function space \mathcal{H}^* . The higher the quality the more of the target function is captured by the feature. We also define a cumulative measure of the quality of the first k eigenfunctions, ordered by the size of their eigenvalues:

$$\Pi^*(k) := \sum_{j=1}^k Q_k^* = \sum_{j=1}^k \sum_{i=1}^C \langle e_j | f_i^* \rangle^2. \quad (7)$$

We will call this measure the *cumulative quality*. Its range is given by $0 \leq \Pi^*(k) \leq 1$. Assuming the f_j are linearly independent, $\Pi_f^*(k)$ measures how much of the C dimensional function space spanned by f is

captured by the first k eigenfunctions or features. Another way of expressing this concept is to say that $\Pi^*(k)$ measures how well the first k eigenfunctions are *aligned* with f^* . For a DNN with a final layer width p , there are p features (eigenfunctions). We expect that *total alignment* or *total quality* of all the features, $\Pi^*(p)$, will typically increase under training. The highest possible total alignment/quality, when the DNN expresses the true-function f^* is $\Pi^*(p) = 1$. The minimum number of features for which $\Pi^*(k) = 1$ can be attained is at $k = C$, which would occur when the quality of Q_k of each feature is at its maximum value of $1/C$. Related cumulative measures of alignment/quality in the context of deep learning can be found for example in [Cristianini et al., 2001; Raghu et al., 2017; Canatar et al., 2021; Canatar and Pehlevan, 2022]. In particular, recent studies [Canatar et al., 2021; Jacot et al., 2020; Cui et al., 2021; Harzli et al., 2021; Simon et al., 2021] have linked better alignment at lower k to better generalization performance in overparameterized linear models. Due to the narrow final layer widths, the learning problem described here is underparameterized, but the idea that good generalisation correlates with large $\Pi^*(p)$ should be robust.

Analogous measures to those above for the target function f^* can also be defined for the vector function $\hat{f} : \mathcal{X} \rightarrow \mathbb{R}^C$ expressed by the DNN after training, which we call the ‘learned function’. The learned function space is given by $\hat{\mathcal{H}} = \text{span}\{\hat{f}_1, \dots, \hat{f}_C\}$. Similarly, a projection operator $P_{\hat{\mathcal{H}}}$ onto the learned function space can be defined as in Equation (6). This can then be used to define the *utility* \hat{Q}_k of the k th feature which measures how much the trained DNN uses that feature to express \hat{f} :

$$\hat{Q}_k = \frac{\langle e_k | P_{\hat{\mathcal{H}}}[e_k] \rangle^2}{\dim(\hat{\mathcal{H}})}. \quad (8)$$

Similarly, we can define a cumulative measure of the utility of the first k features, ordered by the size of their eigenvalues:

$$\hat{\Pi}(k) = \sum_{j=1}^k \hat{Q}_j \quad (9)$$

which we will call the *cumulative utility*. It takes values $0 \leq \hat{\Pi}(k) \leq 1$. Note that typically, $\dim(\hat{\mathcal{H}}) = C$, since the entries of \hat{f} are likely to be linearly independent. Additionally, the entries of the output function typically exhibit similar norms after training. (i.e. $\|\hat{f}_i\| \approx \|\hat{f}_j\|$). By definition, the *total utility* $\hat{\Pi}(p) = 1$. The smallest k for which $\hat{\Pi}(p) \approx 1$ provides a measure for the effective number of features used by the DNN. By contrast, the total cumulative quality $\Pi^*(p)$ can still be much smaller than 1 if the training leads to a function \hat{f} that significantly differs from the ground truth f^* .

2.4 Eigenvalues and effective dimensions

The eigenvalues determine the speed of coefficient learning under MSE loss in a linear model, as shown in Equation (3). They can also be written in the following way:

$$\rho_k = \langle e_k | T[e_k] \rangle = \langle e_k | \sum_{j=1}^p |\Phi_j\rangle \langle \Phi_j | e_k \rangle = \sum_{j=1}^p \langle \Phi_j | e_k \rangle^2, \quad (10)$$

which shows that they are a measure of the projection of Φ along e_k in function space. It is therefore of interest to plot the distribution of the p eigenvalues as a function of index k .

It can also be useful to define scalar measures to characterize these distributions. For any vector a of positive numbers a_i , the exponential of Shannon entropy [Hill, 1973] can be used as a spectral dimension or effective dimension measure:

$$D_{eff}(a) = \exp \left(- \sum_i \frac{a_i}{\sum_j a_j} \ln \left(\frac{a_i}{\sum_j a_j} \right) \right). \quad (11)$$

If the vector a has d components, then $D_{eff}(a)$ has a maximal value of d when all components are equal (and non-zero). If the distribution of its components is non-uniform, then the effective dimension will be lower than d , with a minimum of 1 if a only has one non-zero component.

The effective dimension or effective rank of T can be measured via $D_{eff}(\rho)$ where $\rho = [\rho_1, \dots, \rho_p]$. In a way that is analogous to the way that entropy quantifies the average number of bits for a symbol in the source coding theorem, this measure implies that although T has a rank of p , it can in principle be compressed to an operator of rank $D_{eff}(\rho) \leq p$. From the perspective of Φ , $D_{eff}(\rho)$ measures how many e_k you need in

expectation to describe $\Phi(x)$ for $x \sim q$. As a practical note, because the first eigenfunction of T upon full training is typically a constant, as discussed in Section 5.1, $D_{eff}(\rho)$ in our study is computed without the first eigenvalue before reintroducing a single dimension (i.e. $D_{eff}(\rho) := 1 + D_{eff}([\rho_2, \dots, \rho_p])$).

We can also use Equation (11) to measure the effective dimension $D_{eff}(Q^*)$ of the set of feature qualities $Q^* = [Q_1^*, \dots, Q_p^*]$. This provides a measure of the effective number of features needed to express the target function. Because the target function may not always be completely expressible by features, this measure can be interpreted as the effective number of features required for the best possible approximation of the target function, given Φ .

Similarly, we can define $D_{eff}(\hat{Q})$ for the feature utilities $\hat{Q} = [\hat{Q}_1, \dots, \hat{Q}_p]$, which describes the effective number of features used to describe the learned function. We expect that $D_{eff}(\hat{Q})$ is roughly the number of features needed to achieve $\hat{\Pi}(k) \approx 1$, which is one measure of the effective number of features used by the DNN to express the learned function \hat{f} .

2.5 Approximating the eigenfunctions and eigenvalues in practice

To calculate the eigenfunctions and eigenvalues using Equation (2) for a given parameter-function map Φ , we also need the true input distribution q , which is in principle inaccessible. However, we assume that for a large enough training set $S_{tr} \in \mathcal{X}$ we can use its n datapoints to obtain n feature vectors of size p , and that these provide a good enough estimate of q that we can use the discrete Nyström method [Baker and Taylor, 1979; Williams and Rasmussen, 2006] to extract eigenvalues and eigenfunctions from the integral equation Equation (2) with sufficient accuracy. We perform singular value decomposition (SVD) on the feature matrix $\Phi(S_{tr}) \in \mathbb{R}^{p \times n}$ to obtain singular values $s \in \mathbb{R}^p$ and p left column eigenvectors $u_k \in \mathbb{R}^p$. We can approximate empirical eigenvalues of T by squaring s and using the left column eigenvectors $u_k \in \mathbb{R}^p$, s_k , and feature map $\Phi : \mathcal{X} \rightarrow \mathbb{R}^p$ to obtain k^{th} eigenfunction $e_k(x) = u_k^T \Phi(x) / s_k$. Note that the eigenfunctions can be used on any data point beyond the training set. Also, we have implicitly assumed $n > p$, but when $n < p$, we can only approximate up to n eigenfunctions and eigenvalues. The algorithm is summarized in Algorithm 1.

Algorithm 1 Empirical eigenfunctions and eigenvalues

- 1: Φ, S_{tr}, x
 - 2: $\phi \leftarrow \Phi(S_{tr})$ (forward transform the training set into the feature space)
 - 3: $u, s, v \leftarrow SVD(\phi)$ (find the eigenvalues and eigenvectors via SVD)
 - 4: $[u_1, u_2, \dots, u_p] \leftarrow u$ (find the column vectors of u)
 - 5: **for** k in $1, 2, \dots, p$ **do**
 - 6: $\rho_k \leftarrow s_k^2$ (approximate eigenvalues)
 - 7: $e_k(x) \leftarrow u_k^T \Phi(x) / s_k$ (approximate eigenfunctions)
 - 8: **end for**
-

To calculate the inner product in Equation (6) involving f^* or \hat{f} in Equation (9) we cannot use the training set, because if one trains to zero training error, both functions will be equivalent on S_{tr} . So instead, given the eigenfunctions, we use the test set S_{te} to approximate the relevant inner products as follows:

$$\frac{\langle e_k | f_j \rangle^2}{\|e_k\|_2^2 \|f_j\|_2^2} = \frac{(\int_{\mathcal{X}} e_k(x) f_j(x) q(x) dx)^2}{\int_{\mathcal{X}} e_k(x)^2 q(x) dx \int_{\mathcal{X}} f_j(x)^2 q(x) dx} \approx \frac{(\sum_{x^{(i)} \in S_{te}} e_k(x^{(i)}) f_j(x^{(i)}))^2}{\sum_{x^{(i)} \in S_{te}} e_k(x^{(i)})^2 \sum_{x^{(i)} \in S_{te}} f_j(x^{(i)})^2}. \quad (12)$$

In Appendix H, we discuss the validity and limits of our approximation methods in more detail. Briefly, to check how well our approximation to q works we used significantly smaller subsets of the training set and found that for scenarios we typically care about, where only a subset of all the eigenfunctions are relevant, this makes no meaningful difference to our measures. For large training and test sets (e.g. $n_{train} = 5 \times 10^4$ and $n_{test} = 10^4$ for CIFAR10) the approximation of the true distribution q with a finite sample as done in Algorithm 1 and Equation (12) should be fairly accurate. The Nyström method becomes less accurate for eigenfunctions with relatively small eigenvalues ρ_k (typically for large k). Furthermore, cumulative projection measures such as $\Pi^*(k)$ suffer from finite size errors when $k \approx n_{test}$ because we use S_{te} in Equation (12). Neither of these sources of error is typically that important for two reasons. Firstly, we normally work in the limit $p \ll n_{test}$. Secondly, we will see that typically a relatively small number $k \ll p$ eigenfunctions dominate our measures. Nevertheless, due to these finite size effects, we exercise caution and present plots only up to $k \sim \mathcal{O}(10^3) \ll n_{test}$.

2.6 Summary of definitions

Term	Notation	Definition
(Forward) Feature map	$\Phi : \mathcal{X} \rightarrow \mathbb{R}^p$	A map that transforms – through all intermediate modules – the raw data to a (feature) vector that is fed to the last linear layer of a DNN. A neural network expresses the function $f(x) = W^T \Phi(x) + b$ on data x where W, b are the last layer weights and biases (Equation (1), Figure 1(a))
(k^{th}) Feature	$e_k(x)$	A random variable where $e_k : \mathcal{X} \rightarrow \mathbb{R}$ is the k^{th} eigenfunction of the feature map (Definition 3)
(k^{th}) Eigenvalue	$\rho_k \in \mathbb{R}$	The eigenvalue of the operator T (Equation (10)).
Coefficient Learning		Only W, b change during training (Definition 2)
Feature Learning		Φ changes during training (Definition 1)
Target function	$f^* : \mathcal{X} \rightarrow \mathbb{R}^C$	The function that describes the true labels on all $x \in \mathcal{X}$.
Learned (expressed) function	$\hat{f} : \mathcal{X} \rightarrow \mathbb{R}^C$	The function expressed by the DNN at a given time t . The default value is the function expressed once training has completed.
Quality	$Q^*(k) \in \mathbb{R}$	The amount the k^{th} eigenfunction $e_k(x)$ aligns to the target function f^* , given by $Q^*(k) = \sum_{i=1}^C \langle e_k f_i^* \rangle^2$ (Equation (6))
Utility	$\hat{Q}(k) \in \mathbb{R}$	The amount the k^{th} eigenfunction $e_k(x)$ aligns to the learned function \hat{f} , given by $\hat{Q}(k) = \sum_{i=1}^C \langle e_k \hat{f}_i \rangle^2$ (Equation (8))
Cumulative quality	$\Pi^*(k) \in \mathbb{R}$	Cumulative quality (up to the k^{th} largest aligning eigenfunction) to target function, given by $\Pi^*(k) = \sum_{j=1}^k Q^*(k)$ (Equation (7))
Cumulative utility	$\hat{\Pi}(k) \in \mathbb{R}$	Cumulative quality (up to the k^{th} largest aligning eigenfunction) to the expressed function, given by $\hat{\Pi}(k) = \sum_{j=1}^k \hat{Q}(k)$ (Equation (9))
Effective dimension	$D_{eff}(a) \in \mathbb{R}$	Exponential of entropy with $[a_1 / \sum_i a_i, a_2 / \sum_i a_i, \dots]$ as probability distribution. Typically used to measure the dimension of $[Q_1^*, \dots, Q_p^*], [\hat{Q}_1, \dots, \hat{Q}_p]$, or $[\rho_1, \dots, \rho_p]$. (Equation (11))
Extended feature (EF) regime		Features are learned, but more than the minimum number are needed to express the final learned function. (Section 2.8)
Minimum Feature (MF) regime		Only the minimum number of features are required to express the learned function. (Section 2.8)
CKA measure	$\kappa_{CKA} \in \mathbb{R}$	A scalar measure of how close a DNN is to expressing the learned function \hat{f} with only C features. A DNN is in MF regime if $1 - \text{CKA}(T, T_{MP}) = \kappa_{CKA} < 0.1$ and smaller κ_{CKA} indicate tighter MF regime (Definition 5)

2.7 Two simple examples of feature learning analysed with our feature learning measures

To illustrate how our measures can be used to capture feature learning, we present two simple examples in this section that also illustrate some basic principles of feature learning in DNNs that we also observe for more complex DNN-data combinations.

First, in Figure 2 we treat a 1-dimensional toy example of a 4-layer FCN learning a Heaviside function with SGD and MSE loss. The advantage of this simple system is that the eigenfunctions can be directly visualised. In sub-figures (a–c), we show the first three eigenfunctions for epochs 0, 10, and 100, respectively. At epoch 100, the MSE loss is less than 10^{-5} , and we consider training to have converged. Note that the rather dramatic feature learning is reflected in changes to the eigenfunctions (thus features) during training of the DNN with SGD.

Interestingly, a similar MSE loss can quite easily be achieved without any feature learning by using fixed hidden layers, e.g. a fixed parameter-function map. However, when we train with full SGD, the DNN does not converge to this coefficient learning solution, which needs on the order of 100 eigenfunctions to reach our

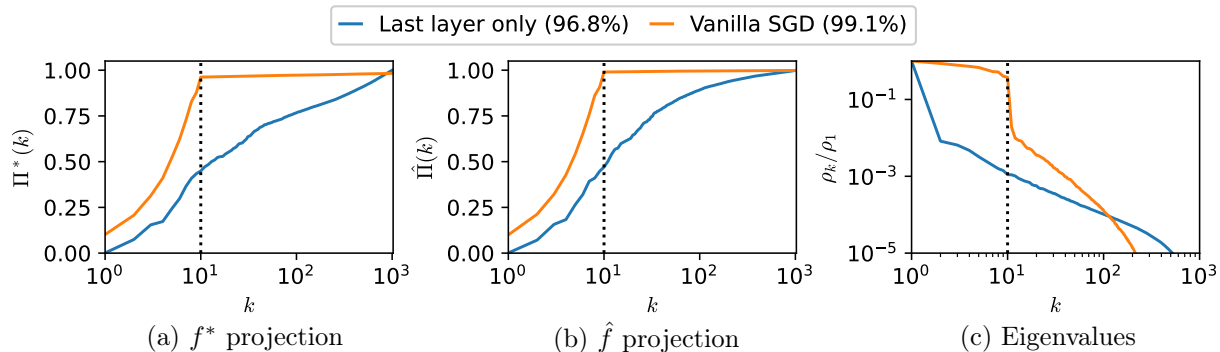


Figure 3: **Comparing feature learning to coefficient learning for a wide CNN on MNIST:** A CNN of width $p = 1024$ can be trained to 100% training accuracy on the full MNIST training set in two different ways. If the hidden layers are fixed at initialization, and only the last linear layer is trained (coefficient learning), then all 1024 initial features are needed, as shown by the blue line, to (a) express the target function and (b) express the learned function. In addition, (c) the eigenvalue spectrum beyond the first eigenvalue follows an approximate power-law decay. By contrast, for vanilla SGD (orange lines in (a-c)), feature learning changes the forward feature map Φ such that only a minimal number ($C = 10$) of features are used. The eigenvalues ρ_k for $k \leq 10$ are significantly larger than the other eigenvalues (note the log scale on the y-axis). Even though both methods achieve reasonably good test accuracy (in brackets), the features used by the DNNs are dramatically different with the SGD-trained network using only 10 features, whereas the last-layer-only training uses all 1024 features.

desired loss value. Instead, the DNN changes the feature map until only one eigenfunction, the one with the biggest eigenvalue, dominates the fit to the target function.

To illustrate how our projection measures $\Pi^*(k)$, $\hat{\Pi}(k)$ and the eigenvalue distributions ρ_k can be used to monitor and visualise feature learning, we plot them in Figure 2(d-f), at 0, 10, and 100 epochs. For example, $\Pi^*(k)$ provides a 1-dimensional visualisation of the observation from Figure 2(a-c) that fewer eigenfunctions are needed in describing the target function as training progresses. This reduction in the number of required eigenfunctions is also reflected in $D_{eff}(Q^*)$, which decreases from 3.2 at epoch 0 to 1.1 at epoch 200. Similarly, $\hat{\Pi}(k)$ helps visualise how many eigenfunctions were used to describe the learned function with $D_{eff}(\hat{Q})$ decreasing from 1.8 to 1.0 after training. Finally, the normalized eigenvalues ρ_k/ρ_1 exhibit faster decay after training, or equivalently a decrease in the effective number of features, as measured by $D_{eff}(\rho)$ which is 1.6 at initialization but 1.2 after training².

For our second example, shown in Figure 3, we compare a CNN trained on MNIST in two ways with a fairly wide last layer ($p = 1024$): In method 1, we fix the hidden layers at initialization and train only the last layer³, which corresponds to coefficient learning. In method 2, We train the same system, but now with SGD.⁴ Both methods achieve zero training error and converge to a reasonably good generalization error⁵, but the projection measures in Figure 3(a,b) allow us to see that the two training methods achieve this similar performance with a marked difference in the quality and utilization of the features. While at initialization, the two systems are identical, the SGD-trained DNN converges to a solution that uses a minimal $C = 10$ number of features, whereas the fixed feature-map system uses all of the available $p = 1024$ features. This marked difference is reflected in the effective dimensions which are $D_{eff}(Q^*) = 120.9$ and $D_{eff}(Q^*) = 68.40$ for the fixed feature-map system, and $D_{eff}(Q^*) = 11.7$ and $D_{eff}(\hat{Q}) = 10.5$ for the SGD trained system. The minimal character of the features is also reflected in the eigenvalue spectrum in Figure 3(c) where the DNN trained with SGD exhibits a much faster drop (note the logarithmic scale), reflecting the fact that the

2. Note that this is the only case where we do not make exceptions regarding the first eigenvalue when calculating $D_{eff}(\rho)$.
3. For last-layer-only training, all other layers are frozen and the last layer is solved using matrix inversion, similar to what is done for linear models
4. The learning rate was 0.05, momentum 0.9, and weight decay was 10^{-3} . The model was trained for 200 epochs during which both training and test loss converged.
5. The fixed feature-map system generalizes slightly less well than the SGD-trained DNN. However, if the layer widths are taken to infinity with the appropriate parameterization, then the fixed feature-map system can be described by a Gaussian process, which can achieve generalization performance that is closer to that of the CNN for MNIST [Lee et al., 2018; Matthews et al., 2018; Lee et al., 2020].

output of feature map Φ is much lower-dimensional. Indeed $D_{eff}(\rho)$ is 118.8 v.s. 11.2 for the last layer only trained and SGD-trained DNNs respectively.

For MNIST, a rather modest width of $p = 1024$ was enough to achieve zero training error for a fixed feature map. In Appendix A we provide further experiments exploring the relationship between the width of the last layer and performance for CNN, ResNet18 and VGG architectures on CIFAR10 and CIFAR100. For these more complex datasets, we estimate that a final layer width on the order of the size of the training set will be needed to achieve zero training error.

2.8 The minimum feature (MF) regime and the extended feature (EF) regime

In the simple examples shown in Figures 2 and 3, a DNN trained with SGD converges on a solution where the number of used features and the number of significant eigenvalues are both close to C . In other words, $D_{eff}(\hat{Q}) \approx C$ and $D_{eff}(\rho) \approx C$ respectively. For the C -way balanced classification task, we will say that a DNN is in the “minimum feature (MF) regime” if the following qualitative properties are satisfied:

1. $\hat{\Pi}_{\hat{f}}(k)$ increases linearly until $k = C$ with $\hat{\Pi}(C) \approx 1$. ($D_{eff}(\hat{Q}) \approx C$).
2. The first eigenfunction e_1 (which is a constant function, see Section 5.1 for further discussion) has an eigenvalue of $a_1 > 0$, while the next $(C - 1)$ -eigenfunctions e_2, \dots, e_C all have eigenvalues of $a_2 > 0$. In addition, all other eigenvalues decrease significantly for $k > C$ ($D_{eff}(\rho) \approx C$).

It would also be useful to derive a quantitative scalar measure of the MF regime. To that end, we first define the state of the operator T in which the above conditions are satisfied exactly.

Definition 4 (Minimum Projection (MP) operator). *For a DNN on a balanced C -way classification task, the integral operator T is an MP-operator T_{MP} if it has two nontrivial eigenspaces, one being the span of constant function $\mathbf{1}$ and the other orthogonal complement of $\mathbf{1}$ inside $\hat{\mathcal{H}}$, where $\hat{\mathcal{H}}$ is C -dimensional function space spanned by entries of the learned function $\hat{f} : \mathcal{X} \rightarrow \mathbb{R}^C$ expressed by the DNN. This is equivalent to that T_{MP} is given as*

$$T_{MP}[u] = a_1 \langle \mathbf{1}, u \rangle \mathbf{1} + a_2 P_{\hat{\mathcal{H}}}(u) \quad \text{for all } u \quad (13)$$

where a_1, a_2 are positive scalars, and $P_{\hat{\mathcal{H}}}$ denotes the orthogonal projection onto $\hat{\mathcal{H}}$.

Ignoring the constant function, whose discussion is deferred to Section 5.1, the MP-operator is a simple projection onto $\hat{\mathcal{H}}$. It is easy to see that the operator $P_{\hat{\mathcal{H}}}$ satisfies the qualitative properties above. First, $P_{\hat{\mathcal{H}}}$ has only C eigenfunctions, and $\hat{Q} = C^{-1}$ by Equation (9), satisfying the first property⁶. The second property follows since $P_{\hat{\mathcal{H}}}$ has C equal non-zero eigenvalues. We note that the T_{MP} operator is closely related to the phenomenon of NC [Papayan et al., 2020]. Indeed, in Section 5 we prove that T_{MP} leads to NC under mild conditions.

Having defined T_{MP} , we will use the centered kernel alignment (CKA) measure (see e.g. [Kornblith et al., 2019]) to calculate how close an empirically measured T is to the idealised operator T_{MP} :

$$CKA(T, T_{MP}) = \frac{\text{Tr}(c(T)c(T_{MP}))}{\|c(T)\|_F \|c(T_{MP})\|_F}, \quad (14)$$

where $c(A)$ is centering operator $(I - |\mathbf{1}\rangle\langle\mathbf{1}|)A(I - |\mathbf{1}\rangle\langle\mathbf{1}|)$, I is identity and $|\mathbf{1}\rangle\langle\mathbf{1}|$ is the constant function $\mathbf{1}$ in $L^2(\mathcal{X})$, and $\|\cdot\|_F$ is the Frobenius norm. CKA has been used for comparing features of DNNs [Kornblith et al., 2019], and also for studying the evolution of the NTK [Baratin et al., 2021; Lou et al., 2022]. Notably, it has the advantage that the measure is invariant to isotropic scaling.

The CKA measure allows us to define a scalar quantitative criterion to measure whether a DNN is in the MF regime, which we can use as an additional layer of assessment to complement our more qualitative definitions 1. and 2. above:

Definition 5 (CKA Minimum Feature Regime Measure κ_{CKA}). *For a distribution q and a class-balanced learned function \hat{f} , a DNN is in MF regime if $\kappa_{CKA} = 1 - CKA(T, T_{MP}) < \epsilon$, where T is the feature kernel (operator) of a DNN and T_{MP} is the MP-operator.*

⁶ This assumes that $[\hat{f}_1, \dots, \hat{f}_C]$ are C linearly independent, which is typically true for DNN trained on a balanced dataset.

The advantage of this scalar measure is that it gives a single number that can be reproducibly used to distinguish regimes. There is some arbitrariness with the choice of ϵ , but we find that $\epsilon = 0.1$ correlates well with more informal visual measures of the MF regime using the criteria above. Needless to say, these measures do not exhaust all the information that can be gleaned from observing the eigenvalue distributions, and the two projection measures as a function of k .

We can also define an **extended feature (EF) regime** for the case where, on the one hand $\kappa_{CKA} > 0.1$, and on the other hand the coefficient learning regime has not been reached so that $\Phi_{(t)}(x) \neq \Phi_{(0)}(x)$ for at least one $x \in \mathcal{X}$. Therefore the EF regime encompasses everything between strict coefficient learning and the MF regime. We note that it could be interesting to also define a scalar measure similar to κ_{CKA} of how far the EF regime is from the strict coefficient learning regime, but we leave that for future work. We have also focused on balanced C-class classification. It would also be interesting to extend these definitions to datasets that are not class-balanced, which we leave to future work.

2.9 Architectures and Datasets used in experiments

In this paper, we mainly confine ourselves to classification on standard datasets such as MNIST, CIFAR10, and CIFAR100, and use MSE loss. Where not explicitly stated, we use the SGD with a momentum of 0.9, weight decay of 10^{-3} , and a learning rate of 0.05 which is decayed by a factor of 0.2 at every 60 epochs. For CIFAR10, all models are trained for 200 epochs, in which both the training and test loss converged, using standard data augmentation (random crops and horizontal flips). For CIFAR100, all models are trained for 600 epochs without a learning rate scheduler, using standard data augmentation (random crops and horizontal flips). The training accuracy is over 99.5% for all models unless explicitly stated. For further details on the experimental setups, see Appendix G.

3. Analysing feature learning using projection measures and eigenvalue distributions

In this section, we treat several examples that illustrate in more detail how our measures can shed light on the phenomenology of feature learning. First, we explore how feature learning changes as the training set size n increases. By comparing with a neural network Gaussian process (NNGP) we show that feature learning can induce a significant change in the scaling exponent for learning curves, consistent with prior work [Geiger et al., 2021; Vyas et al., 2022]. Next, we show how feature learning develops with epochs, comparing convergence to two different regimes: the MF regime for a ResNet18 on the full CIFAR10 dataset, and the EF regime for an FCN on the same dataset. We then explore how our measures can shed light on the role of features in some standard transfer-learning scenarios. We also study how scaling the network output by a positive constant $\alpha > 1$ weakens feature learning, and how this change relates to the concepts of lazy and rich regimes of feature learning. Finally, we use the CIFAR100 dataset to provide examples of feature learning for larger numbers of classes in the MF regime.

3.1 Feature learning as a function of training set size

In Figure 4 (a) we show how our measures change as a function of training-set size for our standard implementation of ResNet18 on CIFAR10 (details in Section 2.9). For smaller training sets, the system is clearly in the EF regime, as can be seen, for example, by the difference between the cumulative quality at $k = C$, $\Pi^*(k = 10)$, and the final alignment/quality $\Pi^*(p)$, by the fact that the eigenvalue distribution does not have a clear plateau for $1 < k \leq C = 10$, and by the scalar κ_{CKA} measure. There is clearly a transition from the EF regime to the MF regime between $n = 1000$ and $n = 5000$, as can be seen by examining these same measures.

For this ResNet18 the final layer width is $p = 512$. If the amount of training data $n \lesssim p$, a DNN should be able to reach zero training error by coefficient learning (Definition 2). For larger training set sizes feature learning will be a precondition for reaching zero training error due to the limited expressivity of the random feature model for such a relatively narrow last layer where $n \gg p$ (see also Appendix A). Coefficient learning alone will not be enough. While more work is needed to understand exactly why a DNN converges to the EF or the MF regime, it may not be surprising that a DNN will use more features if the system is closer to a regime where it could also achieve zero training error with only coefficient learning.

There has been a lot of recent interest in scaling laws for DNNs. These include how generalisation performance as a function of model size, training set size, or simply the cost of computational resources, see

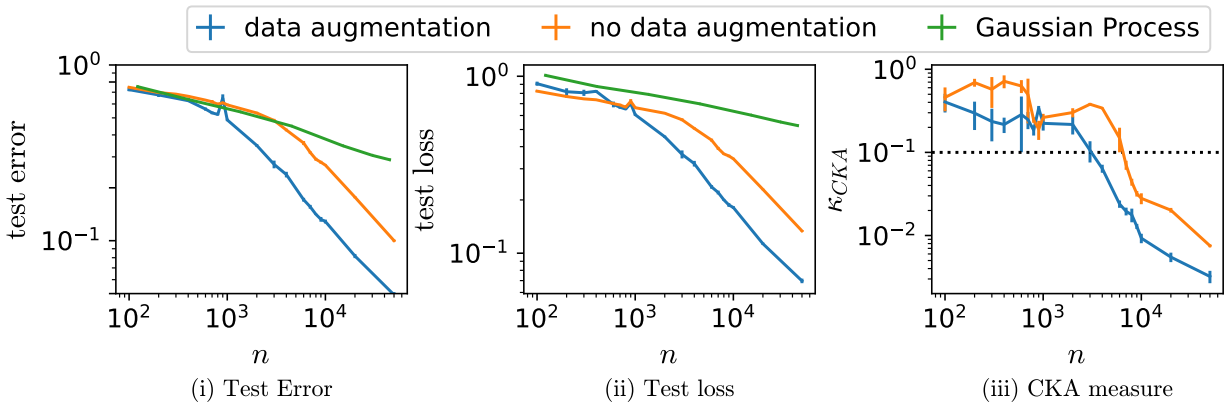
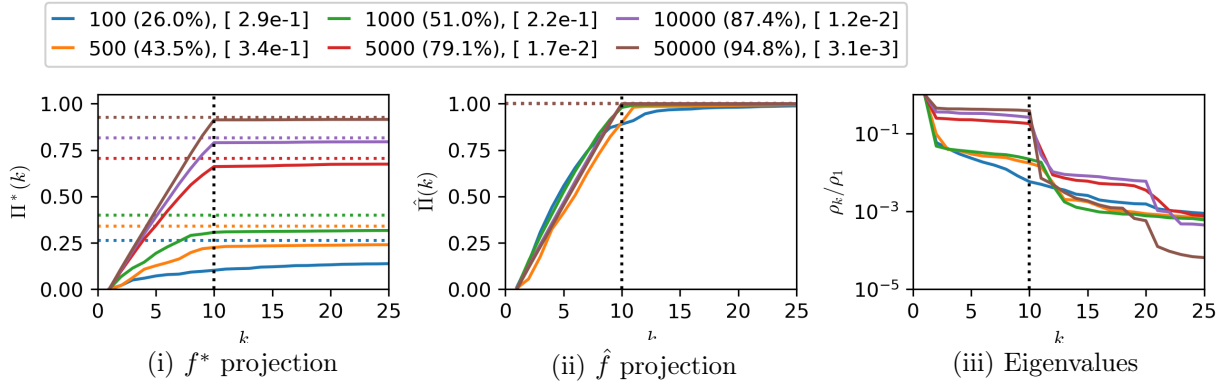


Figure 4: **Feature learning as a function of training set size n .** a) For a ResNet18 on CIFAR10 using our standard hyperparameters with data augmentation (Section 2.9) we show (i) the cumulative quality (Equation (7)), horizontal dotted lines denote the final quality/alignment $\Pi^*(p)$; (ii) the cumulative utility (Equation (9)) and (iii) the eigenvalue distribution (Equation (2)) with a vertical dotted line at $k = C$. Above the figure, the test accuracy is shown in curved brackets, while the CKA measure κ_{CKA} (5) is shown in square brackets. The MF regime is defined to occur when $\kappa_{CKA} \leq 0.1$. Both the final quality/alignment $\Pi^*(p)$ and the generalisation performance increase with increasing training size n , as expected. Between training set sizes $n = 1000$ and $n = 5000$ there is a clear transition from the EF regime to the MF regime, observable both in κ_{CKA} and in the eigenvalue distribution. (b) Shows the associated learning curves for (i) the test error, and (ii) the MSE loss for the ResNet18 model used in (a), and also for an NNGP for the same ResNet18 architecture which has no feature learning, and the ResNet18 model without data augmentation that matches the NNGP setup. The two feature learning models show a marked shift in the rate of decrease of test error and test loss accompanied by a drop in κ_{CKA} at roughly the same values of m , as shown in (iii). The NNGP shows a more constant decay rate in error and loss.

e.g. [Hestness et al., 2017; Kaplan et al., 2020; Spigler et al., 2020; Hoffmann et al., 2022; Valle-Pérez and Louis, 2020; Bahri et al., 2021; Nam et al., 2024] and references therein. It is interesting to ask what the impact of feature learning is on these scaling laws. To that end, we plot, in Figure 4(b), the learning curves for the test accuracy (i) and test loss (ii) for the ResNet18 from Figure 4(a). We also show the learning curves for the NNGP corresponding to the same ResNet18 architecture. Because it is computationally difficult to use the NNGP with augmented data, we also include the ResNet18 for non-augmented data for a more direct comparison to the NNGP. The NNGP will by definition not feature-learn, so comparing the two machine-learning methods can shed light on how feature learning affects performance as a function of training set size n . For the NNGP we observe a scaling law with close to a fixed exponent over the domain. For the two ResNet18 variants, we find that after an initial lower exponent, there is a clear transition from a slower decay rate in the EF regime, similar to that of the NNGP, to a faster decay with a larger exponent once full feature learning to the MF regime sets in.

Interestingly, prior work has also shown that kernel regime (infinite-width DNNs with NTK or NNGP parameterisation) has a smaller exponent in the decay of learning curves, see e.g. [Geiger et al., 2021; Vyas et al., 2023]. Here we explicitly show that the change in scaling exponent correlates with a change in feature learning. Whether this correlation is causal is left for future work. As can be seen in Figure 4(b)(iii), the κ_{CKA} measure shows that the MF regime occurs for smaller n for the ResNet18 with augmented data, than for the case of no data augmentation. The point at which $\kappa_{\text{CKA}} \lesssim 0.1$ is also roughly the point at which a different higher exponent kicks in for the learning curves. Both learning curves have very similar exponents in the MF regime. Prior results comparing the scaling exponents from marginal-likelihood PAC-Bayes bound to full DNN calculations in [Valle-Pérez and Louis, 2020] suggest that the effect of feature learning on the decay rate will be larger for more complex datasets. More work needs to be done to fully understand the effect of feature learning on scaling exponents.

3.2 Feature learning as a function of epoch for the MF and EF regimes

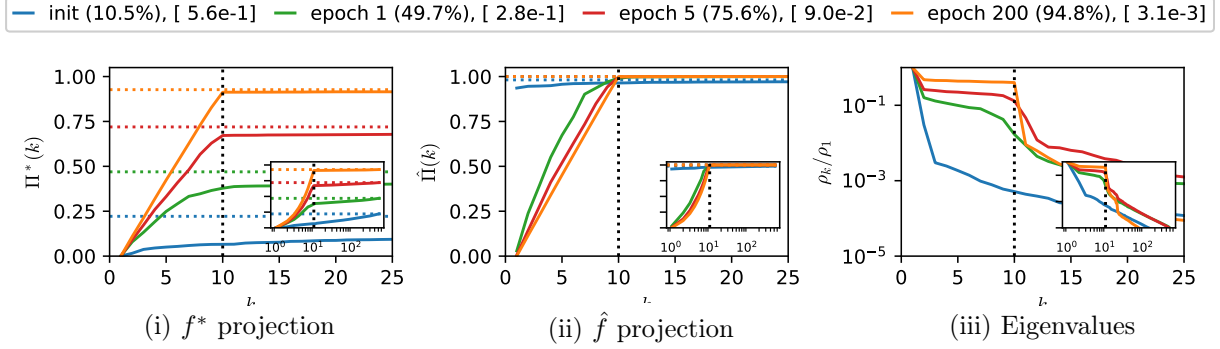
In Figure 5(a) we show data for ResNet18 on the full CIFAR10 dataset as a function of epochs. There is already a significant change in $\Pi^*(k)$, $\hat{\Pi}(k)$ and the eigenvalue distribution after just one epoch (In Figure 16 we plot data during the first epoch, showing in more detail how significant changes happen very early in training). Indeed, in (a,ii), we observe that the first C features dominate the learned function as early as epoch 1. Such rapid increases in alignment with training time are consistent with previous research, see e.g. [Atanasov et al., 2021; Ba et al., 2022] and references therein. After just 5 epochs, the system is already in the MF regime, as can be seen by the value of κ_{CKA} and also in (a,iii), where the eigenvalues flatten for $1 < k \leq C$ and then drop at C leading to $\rho_C \gg \rho_{C+1}$ and that $D_{\text{eff}}(\rho) \approx C$. Test performance continues to improve significantly up to epoch 200.

By contrast, we show in Figure 5(b) that an FCN trained on the same dataset exhibits weaker feature learning and remains firmly in the EF regime, even when both training and test accuracies converged. When compared to the ResNet18, $\Pi^*(k)$ is significantly lower for all k , indicating poorer quality features. This is also reflected in the significantly lower generalisation accuracy. In Figure (b,ii), we observe that significantly more than C features are needed to express the learned function. This is also reflected in $D_{\text{eff}}(\hat{Q})$ at epoch 200 where the values are 10.07 for ResNet18 and 34.60 for FCN. In (b, iii), we observe that the eigenvalues show a much more gradual drop. Using a scalar measure, $D_{\text{eff}}(\rho)$ at epoch 200 is 10.47 for ResNet18 and 129.9 for FCN, respectively. In Figure 16 we also show how the same measures change during the first epoch. Not surprisingly, for the FCN on CIFAR10, the change is less pronounced in the first epoch than it is for the ResNet18.

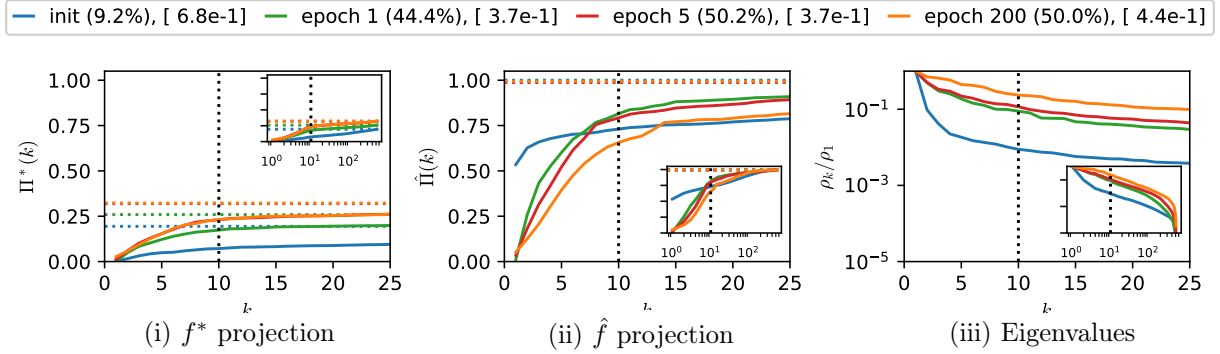
Finally, we note that, in contrast to the CIFAR10 case, an FCN can reach the MF regime in just a few epochs when trained on a simpler dataset such as MNIST, see Figure 6, and also Figure 17. This result suggests that the EF regime, is a function of the particular architecture-data combination, and not of the architecture alone. Note also that for the FCN, it has been shown that the lazy regime without feature-learning can lead to better generalisation error for smooth target functions Petrini et al. [2023].

3.3 Feature learning and inducing the lazy regime at finite width by rescaling the output

The trend of training ever larger models has inspired much theoretical work on the training dynamics of models in the limit of infinite width. Recent progress has included the identification of two distinct training regimes in the infinite width limit. In the first, the so-called ‘lazy’ or NTK limit [Jacot et al., 2018; Lee et al., 2019], the weights only change infinitesimally so that no feature learning occurs, and the training dynamics can be approximated by a linear model. In the second so-called ‘rich’ or mean-field limit [Mei et al.,



(a) ResNet18 on CIFAR10 (MF regime)



(b) FCN on CIFAR10 (Extended Feature (EF) Regime)

Figure 5: **Feature-learning as a function of epochs for the MF and EF regimes** (a) ResNet18 is in the MF regime with optimal hyperparameters for CIFAR10. Projections onto the target function, $\Pi^*(k)$ (i) and the learned function, $\hat{\Pi}(k)$ (ii), as well as the normalized eigenvalue distributions ρ_k/ρ_1 (iii) are shown as a function of epochs. The parenthesis in the labels indicate the test accuracy at a given epoch, and the square brackets denote the scalar CKA-based measure κ_{CKA} from Definition 4. The insets show the same plots for all $p = 512$ features instead of the first 25. At initialization, the learned function is dominated by the first eigenfunction, but after just one epoch, it is dominated by the first 10 eigenfunctions, and is nearly in the MF regime as measured by κ_{CKA} . A related pattern can be seen in (iii) for the eigenvalues, where there is a substantial change already present at epoch 1, and upon full training, the distributions become nearly flat for eigenvalues 2 to 10 (eigenvalue 1 is the constant function, see Section 5.1), after which the distribution drops off rapidly. (b) A 4-layer FCN with a width of 512 is trained on CIFAR10 and provides a typical example of the EF regime. In contrast to the MF regime case for the ResNet18, (i) $\Pi^*(C) < 0.25$ and $\Pi^*(p) < 0.5$ indicates that neither the first C features nor all $p = 512$ features could model the target function accurately. (ii) The FCN requires more features to express the learned function, as reflected in $D_{eff}(\hat{Q})$ at epoch 200 (34.60 for FCN and 10.07 for ResNet18). (iii) Moreover, the eigenvalues do not drop nearly as sharply as in (a). For example, $D_{eff}(\rho)$ at epoch 200 is 129.9 for FCN compared to 10.46 for ResNet18.

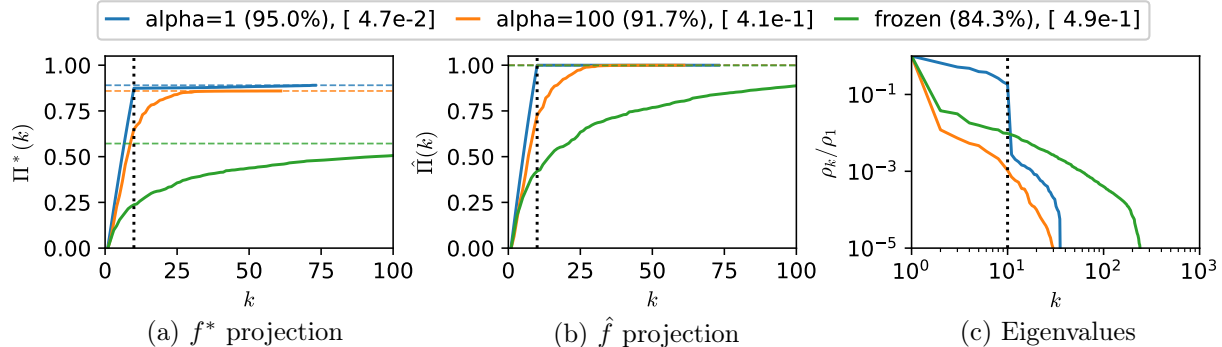


Figure 6: **Features with rescaled output layer compared to fixed features** A 4-layer FCN with a width $p = 256$ is trained on 10,000 images of MNIST, with the rescaling from Equation (15). We compare The standard $\alpha = 1$, to the case where $\alpha = 100$, which is well above the threshold $\alpha/\sqrt{p} > 1$ thought to induce the so-called lazy regime of training. We also treat the coefficient learning regime, where the feature map is kept fixed. For the standard case (blue lines) we observe reasonably good generalization accuracy (in brackets), and MF regime behaviour, both qualitatively, and with our scalar CKA measure κ_{CKA} (square brackets). By contrast, for the large α case (orange lines), many more features are needed to express the learned and target functions, and the system is now clearly in the EF regime. There is also a modest decrease in the generalization error. However, this regime still uses only a modest fraction of all 256 features ($D_{\text{eff}}(\hat{Q}) = 18.70$). This contrasts with the case of a fixed feature map (green lines), which appears to use all 256 features and for which $D_{\text{eff}}(\hat{Q}) = 72.22$. Therefore, in this example, significant feature learning still occurs even for a large constant α .

2018; Rotskoff and Vanden-Eijnden, 2018; Chizat et al., 2019], the DNN does significantly re-arrange its internal representations, even at infinite width. It was shown that in the infinite limit, the latter regime can be achieved by the so-called maximum-update parameterization (μP) [Yang and Hu, 2021; Yang et al., 2023]. Importantly, this method allows one to directly transfer hyperparameters from computationally cheaper narrow models to larger models [Yang et al., 2021].

In [Chizat et al., 2019] it was argued that scaling the output of the function by a sufficiently large constant α and descaling the loss in the following manner

$$\mathbb{L}(x) = \frac{1}{\alpha^2 n} \sum_i^n \ell(\alpha(f(x^{(i)}) - f^*(x^{(i)}))), \quad (15)$$

together with a rescaling of the learning rate allows a DNN to be trained in the lazy limit where the dynamics of GD stay close to that of the corresponding NTK model at initialization. They also argued that $\alpha \propto 1/p$ leads to a feature learning limit (which does not admit a kernel description). Furthermore, in [Geiger et al., 2020, 2021], it was argued that the transition from the rich to lazy regimes depends on width p through the scaling ratio α/\sqrt{p} . This rescaling has been used to approximate the lazy limit in finite-sized DNNs [Geiger et al., 2020, 2021; Vyas et al., 2023]. For MSE loss, Equation (15) reduces to a simple rescaling of the target function by α^{-1} .

In Figure 6 we compare the rich regime ($\alpha = 1$) to what is predicted to be the lazy regime ($\alpha/\sqrt{p} \approx 6.25$). We also compare to a fixed feature map that can only undergo coefficient learning (Definition 2), and so cannot feature learn. Increasing α well above the threshold from [Geiger et al., 2020] indeed changes the way that features are learned, and the dynamics transition from the MF regime to the EF regime. Nevertheless, significant feature learning is still observed when compared to fixed features. This behaviour is not surprising for this problem because we know that significant feature learning is needed no matter what value of α is used, since the final layer is too narrow to be expressive enough to fit the training data without changing the feature map. Indeed, we observe that the training accuracy for frozen features after training is 85%, and as can be seen in In other words, feature learning is inevitable if 100% training accuracy is achieved for narrower widths.

Finally, we note the lazy regime typically refers to the NTK limit, while our way of fixing the feature map will reduce to (a sample from) an NNGP in the limit of infinite width. The features of NTK are defined via gradients, and while for linear models they are the same as our forward features, that is no longer the

case for non-linear models. Further work is needed to clarify the connection between forward features, the backward features of the NTK, and what happens, for example, under the μP scaling of parameters Yang and Hu [2021]. It would also be interesting to perform our experiment above for widths wide enough so that the DNN can reach zero training error for a fixed feature map. While there is much left to do regarding this particular question, we hope our initial investigation has shown the value of using our measures to explore this aspect of feature learning.

3.4 Transfer Learning

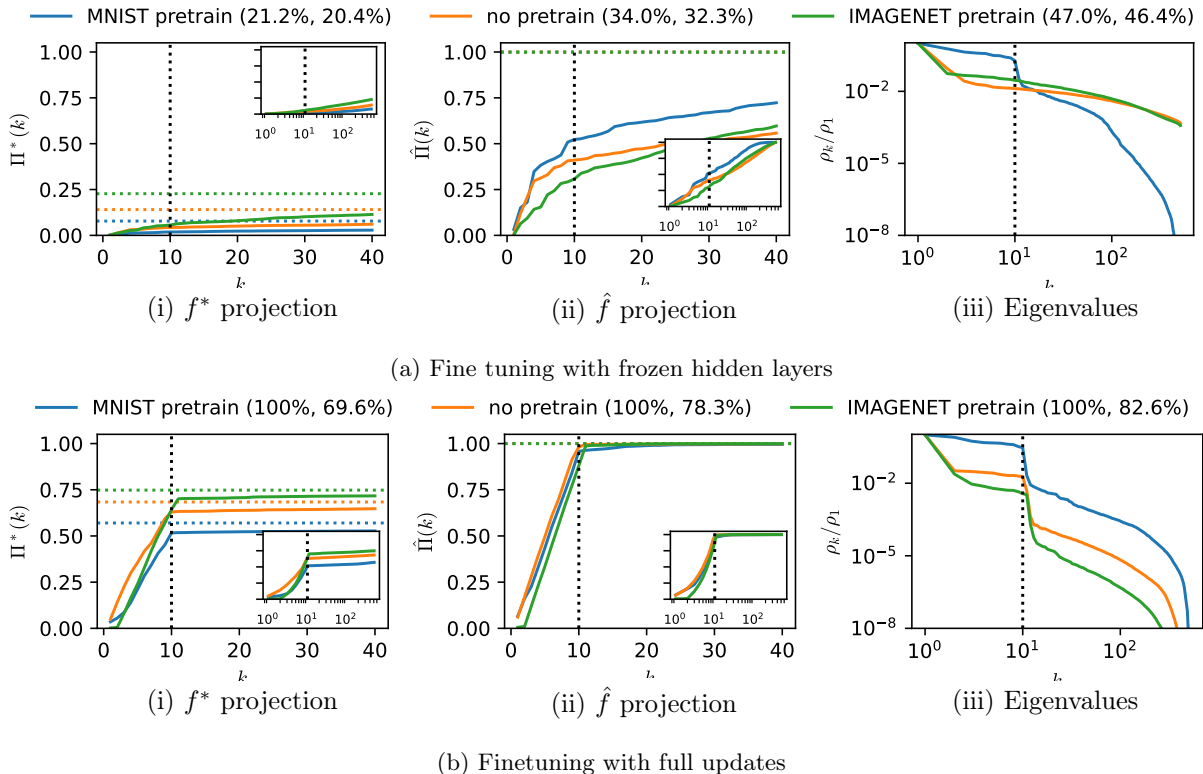


Figure 7: **Visualizing the quality of transferred features after fine-tuning.** We use our measures to compare features from ResNet18 for three cases: (1) pre-trained on MNIST, (2) initialized in the standard way with no pre-training, and (3) pre-trained on IMAGENET. Each is transferred to a ResNet18 on the CIFAR10 classification task. The parenthesis shows (training accuracy, test accuracy) after 200 epochs, by which time both accuracies converged. (a) Comparing features of the models fine-tuned with frozen hidden layers, meaning the features remain fixed throughout training. The features can be visually compared in (i) by how well the feature quality matches the target function; we observe that higher final quality directly correlates with generalization performance. In (ii) we observe that all features are used for the final learned function, but that the system cannot reach 100% training accuracy due to the limited quality and the relatively small width $p = 512$ compared to the dataset size $n = 50,000$. All insets denote the same plot but with all 512 features on a logarithmic x-axis scale. (b) Features of the models fine-tuned with full training with SGD show that while the features evolve significantly during full fine-tuning, their final quality correlates with the quality of the initially transferred features, which is reflected in the generalization performance. In both scenarios, the quality of features is the best for the model pre-trained on IMAGENET and the worst for the model pre-trained on MNIST, suggesting that our measures accurately capture key aspects of transferred features. Finally, in contrast to other figures, the ResNet18 used in this figure follows standard PyTorch implementation which is different from ResNet18 used in Figure 5(a). See Appendix G.1 for further details.

Transfer learning is the practice of training a model with one task and then using (transferring) the learned features to a new task, with the goal of boosting performance [Pan and Yang, 2009; Zhuang et al., 2020]. It is thought to play a key role in facilitating the remarkable performance of foundation models Bommasani et al. [2021]. Nevertheless, the theory of transfer learning remains under-explored.

Further training on a new task, which is often called fine-tuning, can then be performed either by keeping the hidden layers fixed, which corresponds to a fixed forward feature map Φ , or else by using the pre-trained network as the initialization for a conventional SGD based training process on the new task. Typically, the quality of the transferred features is measured by the generalization accuracy of the new task. Here we will illustrate how our feature learning measures can provide additional information about transfer learning.

Transfer learning in our language is the transfer of the feature map Φ , but not the features themselves as these also depend on the true data distribution q of the new task. Assuming that the true underlying distributions of tasks are related, then the transferred feature map should also provide appropriate features for the new task. In Figure 7, we compare the performance of different kinds of transfer learning for ResNet18 (the default Pytorch version for Imagenet) on CIFAR10. The feature map is taken from 1) a ResNet18 pre-trained on MNIST, which is simpler than CIFAR10, 2) a baseline without pre-training, and 3) a model pre-trained on IMAGENET, which is more complex than CIFAR10. We then fine-tune the model by either fixing the pre-trained feature map and only learning the last layer, or by taking the pre-trained feature map as the initialization for a standard SGD optimization. As expected, the performance is worse for pre-training on MNIST, and best for pre-training on IMAGENET, with the standard baseline case in between. Note that, in contrast to the ResNet18 used previously in Figure 5, the default Pytorch implementation of ResNet18 has significantly lower performance. For further details of the different implementations, see Appendix G.1.

As shown in Figure 7, our measures provide a more fine-grained picture of what transfer learning does to the features of the DNN trained on the new task. Figure 7(a,i) depicts the alignment/quality measure, $\Pi^*(k)$, for the pre-trained networks, with $\Pi^*(p)$ being larger for better performing models. For fine-tuning with fixed hidden layers, the $\Pi^*(p)$ is directly linked to the generalization performance since the fine-tuning process is a simple linear regression on the last layer features. The fact that $\Pi^*(p) < 0.25$ for all three scenarios indicates the limited quality of the features in expressing the target function. Moreover, with $p = 512 \ll n = 50,000$, there is an insufficient number of features to fit all training data points.

On the other hand, during fine-tuning with full training, further feature learning occurs, which complicates any analysis of how much the transferred features influence the outcomes. Nevertheless, we observe the quality of initial features (Figure 7(a,i)) and trained features (Figure 7(b,i)) correlate with one another, and with generalisation performance. These results raise further questions, such as the exact relationship between initial features and final performance which will depend, for example, on details such as the learning rate and other hyperparameters. Nevertheless, we believe that this simple exercise points to the potential fruitfulness of using our feature learning measures to study transfer learning.

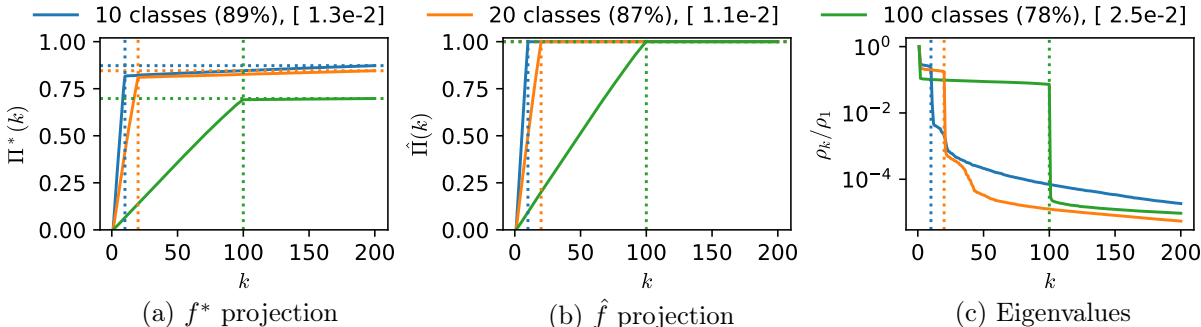


Figure 8: **Minimum feature regime for different number of classes** ResNet18 trained on 10, 20, and 100 classes from CIFAR100 for 600 epochs (until convergence). (a) All models show that the first C features capture most of the alignment to the target function (i.e. $\Pi^*(C) \approx \Pi^*(p)$) where $\Pi^*(p)$ is plotted as dotted horizontal line. Note that $\Pi^*(p)$ decreases as the number of classes increases, reflecting the relative difficulty of the tasks. (b) All models are in the MF regime with only C features being used to express the learned function (i.e. $\hat{\Pi}(C) \approx 1$). (c) All three cases show a typical MF regime behaviour of the eigenvalue distribution, a flattening of eigenvalues for $1 < k \leq C$, and then a rapid drop for $\rho_{k>C}$.

3.5 Multiple classes and the MF regime

In Figure 8, we show how the MF regime changes for CIFAR100 while varying the number of classes C in 10, 20 and 100. From (b), we observe that only the first C features are utilized. Additionally, in (c), we note

that the first $1 < k \leq C$ eigenvalues are flat and significantly larger than ρ_{C+1} . These results show that the basic MF regime phenomenology is consistent for different numbers of classes. We note that in the eigenvalue distributions, there is a small feature at $k = 2C$ for the $C = 10$ and $C = 20$ cases, but have not explored this further.

4. Hyperparameter tuning, generalization performance and the MF regime

In practice, significant effort and computational resources are dedicated to tuning hyperparameters to optimize the performance of deep neural networks (DNNs). Can our approach to measuring feature learning provide additional signals—beyond directly assessing generalization performance—that indicate when optimal performance is being approached during hyperparameter tuning?

Throughout this paper, we observe empirically that the MF regime typically leads to better generalization performance than the EF regime. For example, in Figure 5(b) we observe that an FCN on CIFAR10 in the EF regime learns low-quality features. One could consider this a kind of overfitting since more features are used than are strictly necessary. There are also theoretical arguments in the NC literature suggesting that minimal features in the full NC regime correlate with better performance due to their max-margin nature [Papayan et al., 2020; Kothapalli et al., 2022]. Indeed, there are some close similarities between the MF regime and NC. We explore some of these connections more formally in Section 5, using our T_{MP} operator. However, these arguments that NC implies good generalization have recently been criticized in [Hui et al., 2022] on the grounds that NC is a function of the training data only, so it would be surprising if NC by itself can guarantee generalization. By extension, we expect that the MF regime—which is measured on training data—cannot, on its own, guarantee generalization either. Indeed, while we find in this paper that the MF regime frequently correlates with better performance than the EF regime, we will also present examples of poor performance within the MF regime. The purpose of this section will then be to empirically explore the connections between our measures of feature learning, the MF regime, and generalisation performance.

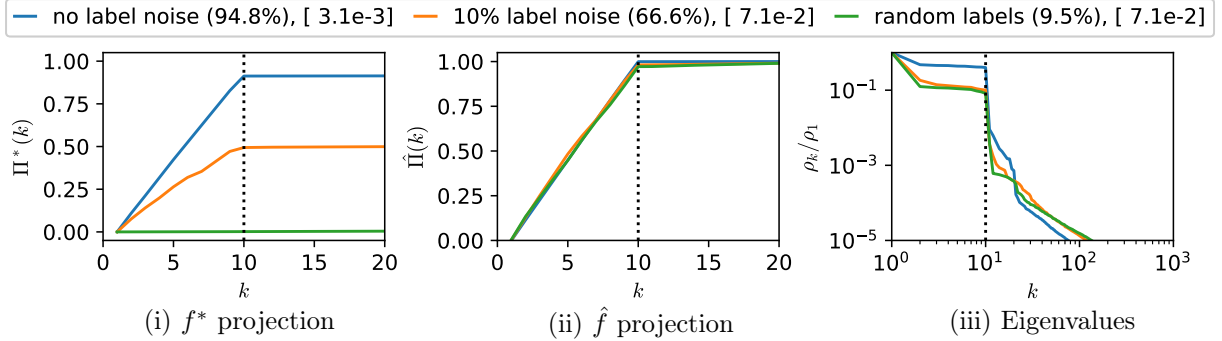
4.1 The MF regime can be obtained even for poor generalization

In Figure 9, we illustrate several scenarios where a strong MF regime is obtained, but where generalization error varies significantly. The first, in Figure 9(a), shows that training a ResNet18 on CIFAR10 with no noise, 10% label noise, or entirely random labels still maintains a strong MF regime, even though, not surprisingly, generalization performance decays significantly with increasing noise. The system is in the MF regime but does not differentiate between noise and signal. It simply learns the minimum number of features that fit the training data. These experiments suggest that the primary driver of the MF regime is the training dynamics rather than an inherent signal in the CIFAR10 dataset.

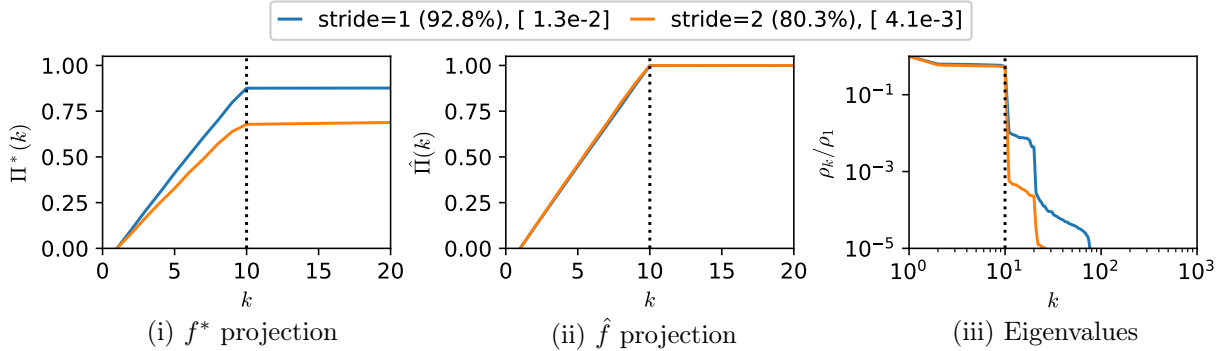
In Figure 9(b), we present a more subtle example. Two ResNet18 variants with different strides in the initial convolution module are compared.⁷ Even though the model with stride=2 has a strong MF regime with a smaller CKA measure, its performance is significantly worse than the model with stride=1. This is due to the differences in the quality of the features as visualised in Figure 9(b,i). Note that it may still be the case the MF regime signals that other hyperparameters are set in a fashion that gives close to the optimal performance for the particular value of stride. However, the presence or absence of the MF regime cannot be used here to say much about the optimal value of stride.

These examples demonstrate that the quality of the features, measured on the test set by $\Pi^*(k)$, rather than just their minimal number, is critical if a connection to generalization is to be made. This observation is similar to the case for overparameterised linear models, including those inspired by DNNs [Canatar et al., 2021; Jacot et al., 2020; Cui et al., 2021; Harzli et al., 2021; Simon et al., 2021], where it can be shown explicitly that the quality of features is the key for good generalization performance. These prior works also raise the question of whether one could derive similar analytic results for this underparameterized problem.

7. Keen readers may wonder about the lower performance (80% test accuracy) of ResNet18 with stride=2 on CIFAR10. The stride=2 model with an initial max-pooling was originally proposed by [He et al., 2016] and is the default Pytorch [Paszke et al., 2017] implementation. Studies using the same architecture achieve similar performance, for example, [Zhu et al., 2021]. A more widely used ResNet18 variant, often under the same name, but with a smaller stride and no max-pooling, achieves significantly improved performance on CIFAR10, see for example, [Nakkiran et al., 2021], but many other papers do this. For further details of the role of stride, see Appendix G.1.

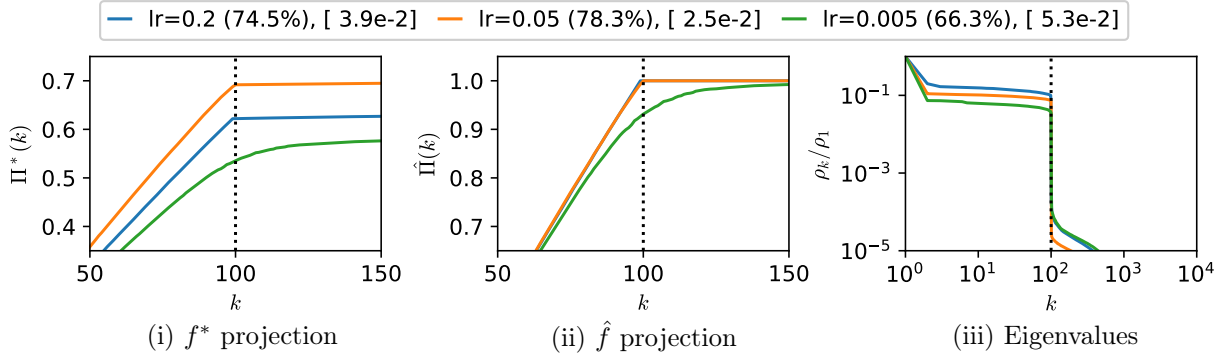


(a) ResNet18 on CIFAR10 with label randomization

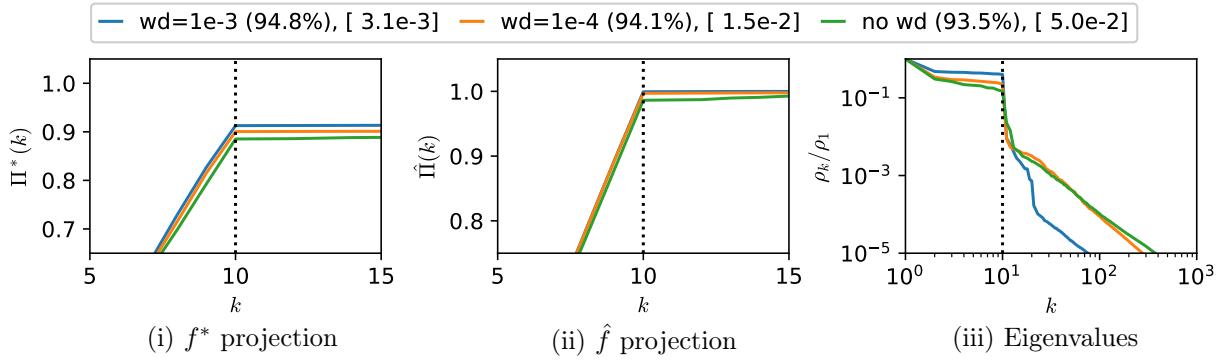


(b) ResNet18 on CIFAR10 with different stride values

Figure 9: **MF regime for ResNet18 with randomised data and differences in stride.** In (a) we trained a ResNet18 on CIFAR10 with 0%(blue) 10%(orange) and 100%(green) label noise. All three cases converge to the MF regime, but differ markedly in performance. (b) ResNet18 trained on full CIFAR10 with stride=1,2 at the initial convolutional module. Both models are in the MF regime, but their performance differs significantly. While the stride = 2 (orange) has a more distinct drop of eigenvalues at $k = C$, the cumulative quality of the first C features, as well as the generalisation performance, is significantly larger for stride = 1 model (blue). Note that in this plot, the stride=1 and stride=2 models have additional max pooling after initial convolution making the model with stride=1 slightly different from the one used elsewhere in this paper.



(a) ResNet18 on CIFAR100 with different learning rates



(b) ResNet18 on CIFAR10 with different weight decay rates

Figure 10: **Effects of learning rates and weight decay on feature learning and generalization** In (a) we explore the effect of changing the learning rate for a ResNet18 on CIFAR100. Note that the lower learning rate leads to the EF regime, and poorer performance. The best performance is for the intermediate learning rate, which is in the MF regime. The higher learning rate, with slightly less good performance, is also in the MF regime. In (b) we study the effect of weight-decay for a ResNet18 on CIFAR10 where we observe that a tighter MF regime correlates with a larger weight-decay and better performance.

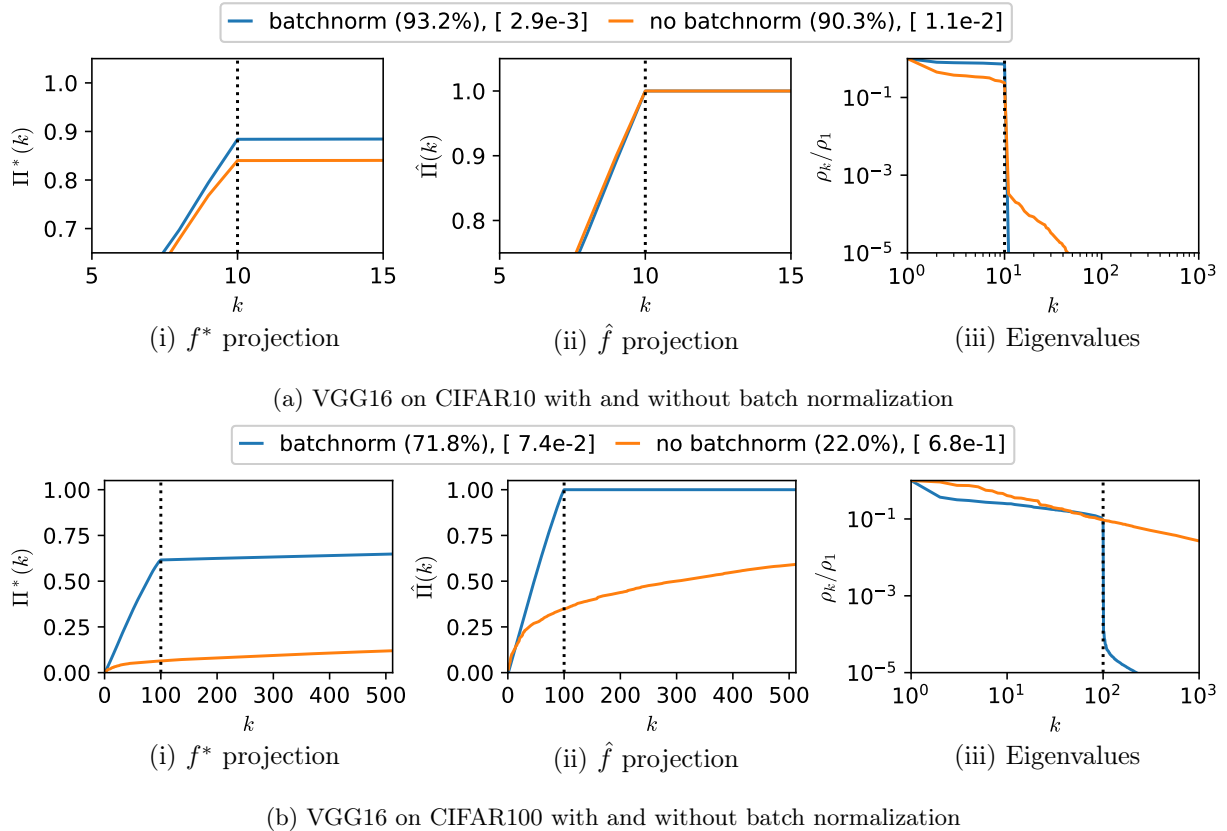


Figure 11: **Effect of batch normalisation on feature learning and generalization** In (a) we explore the effect of turning off batch normalization for the VGG16 architecture on CIFAR10. While both cases exhibit MF regime behaviour according to our CKA measure, we observe that including batch normalization results in a tighter MF regime, including a flatter first C eigenvalues and a wider gap between ρ_C and ρ_{C+1} . In (b) we explore the effect of batch normalization on a more extreme case of VGG16 on CIFAR100. The difference in performance is large, as is the difference in how features are learned. The system with batch normalisation is clearly in the MF regime, while without batchnorm the system is deep in the EF regime. This difference is there, despite both models achieving training accuracy of over 94%.

4.2 Exploring the effect of hyperparameter tuning in feature learning

In Figure 10 we explore two examples of how hyperparameter tuning affects performance and feature learning. One of the most common hyperparameters to tune is the learning rate. As expected, we find that performance is affected by the learning rate. In Figure 10 (a) we observe that the two better-performing learning rates are in the MF regime. For the smallest learning rate, which also performs significantly less well, we observe the EF regime.

In Figure 10(b), we show that weight decay also flattens the distribution of first C eigenvalues. It has been argued in [Galanti et al., 2022] that weight decay contributes to finding a low-rank solution. However, we note that here MF regime is also achieved without weight decay.

In Figure 11 we study another popular trick, batch normalization. For this particular case, batch normalization leads to better generalization on CIFAR10 and a slightly tighter MF regime. Indeed, the flatter distribution of eigenvalues in Figure 10(a, iii) is consistent with batch normalization’s rescaling property. VGG16 on CIFAR100 is a famous case where batch normalization has a dramatic effect on generalisation Santurkar et al. [2018]. Here we show that this large difference in performance is reflected in how the features are learned. With batch normalisation, the VGG converges to the MF regime, and exhibits good performance. Without batch exnormalisation, feature learning is much less strong, and the VGG16 converges to solution in the EF regime.

The upshot of these experiments is that we typically see a slight tightening of the MF regime for hyperparameters that lead to better generalization, but as shown for the example of stride in Figure 10, this is not universal, and the effect is generally quite small. We also observe the EF regime, for small learning rate, and more dramatically for the case of no batch normalisation for the VGG on CIFAR100. In these examples, the EF regime is typically associated with the poorest generalisation performance. Nevertheless, these are only a handful of examples, and further work is needed to confirm how widely and under what conditions these trends hold. It may be that to analyse the effect of hyperparameter tuning on feature learning, more detailed measures are needed, including ones that track earlier layers in the DNN. This will be the subject of an upcoming paper.

5. The relationship between the MP-operator T_{MP} and neural collapse

Neural Collapse (NC) [Papayan et al., 2020] refers to a fascinating state in a DNN that can arise during the terminal phase of training (TPT), when the system continues training beyond the point where the training error has vanished, aiming to further minimize the loss. This interesting phenomenon has inspired many theoretical studies, see e.g. [Kothapalli et al., 2022] for a review.

NC is characterised by the emergence of four interconnected phenomena upon TPT: NC1) collapse of within-class variability, NC2) convergence of features to a rigid simplex equiangular tight frame (ETF) structure, NC3) alignment of the last layer and features, and NC4) simplified decision by nearest class. We provide more formal measures of these phenomena in Appendix F, following the approach of [Han et al., 2021].

In this section, we recast NC in the language of kernels, an approach similar in spirit to that taken in [Seleznova et al., 2023]. In particular, we explore the relationship between the MP operator T_{MP} defined in Definition 4, and NC. A key observation is that the first eigenfunction of T_{MP} is close to a constant function, and we first discuss what this implies for NC. Subsequently, we present some propositions demonstrating that substituting the true data distribution q with the empirical distribution results in the NC conditions. Finally, we illustrate how our kernel-based formalism allows us to treat regression, where the classical NC picture is not well-defined. Throughout this section, we will assume a balanced C -way classification unless explicitly stated.

5.1 The first eigenfunction of the T_{MP} operator is a constant

MP-operators (Definition 4) include a constant function in addition to a more conventional projection operator onto \mathcal{H} , the C -dimensional function space spanned by entries of the learned function $\hat{f} : \mathcal{X} \rightarrow \mathbb{R}^C$. This difference with simple projection operators means that an MP-operator uniformly rescales all function components in \mathcal{H} in an isotropic manner, with the exception of the direction of the constant function. The fact that the constant function exists in the feature kernel’s reproducing kernel Hilbert space (RKHS) or simply the function space is not surprising as the final output function space typically includes the constant

function.⁸ More importantly, a bias term in the last layer on a DNN adds a constant function to the entries of the output, which necessitates the existence of a constant function in the RKHS of its kernel.

What is perhaps more surprising is that the constant function is the first eigenfunction of T_{MP} with the largest eigenvalue. Interestingly, this function is often disregarded in other analyses, for example in principal component analysis (PCA) and in measurements of CKa. We also observe that the first eigenfunction of T often closely resembles the constant function (even when not at its limit T_{MP}). Across all our experiments, except for the 1-D toy model in Figure 2, we consistently observe $\langle e_1 | \mathbf{1} \rangle > 0.95$. Due to this observation, we handle the first eigenvalue ρ_1 as an exception, for example when calculating $D_{eff}(\rho)$ or defining the MF regime.

We also find that at initialization, the first eigenfunction tends to dominate the initialized function (i.e. $\Pi(\hat{1}) \approx 1$) for architectures such as ResNet18 (Figure 5(a,ii)) and VGG16. Moreover, these architectures have $\langle e_1 | \mathbf{1} \rangle \approx 1$ even at initialization. One possible explanation for this behaviour is simplicity bias [Dingle et al., 2018; Valle-Pérez et al., 2018; Mingard et al., 2019, 2023], which predicts that simple (low Kolmogorov complexity) outputs (functions) are more exponentially likely to appear if the input-output map is simple enough. However, the exact reason why the constant function is the first eigenfunction of the feature kernel requires further study. For the purposes of this paper, we accept this observation as a given.

The constant function also helps explain why the simplex equiangular tight frame (ETF) emerges in NC as the ideal max-margin feature for classification, instead of an orthonormal basis: A $(C - 1)$ -dimensional simplex ETF can be obtained as the projection of the standard basis onto the orthogonal complement of $[\frac{1}{C}, \frac{1}{C}, \dots, \frac{1}{C}]$, which is the average vector of all basis vectors, inside \mathbb{R}^C . For example, projecting $[0, 0, 1]$, $[0, 1, 0]$, and $[1, 0, 0]$ onto the orthogonal complement of $[\frac{1}{3}, \frac{1}{3}, \frac{1}{3}]$ gives three vertices $[-\frac{1}{3}, -\frac{1}{3}, \frac{2}{3}]$, $[-\frac{1}{3}, \frac{2}{3}, -\frac{1}{3}]$, $[\frac{2}{3}, -\frac{1}{3}, -\frac{1}{3}]$ which forms an (ordinary plane) equilateral triangle. We will show in Equation (20) that a constant function maps to a global average vector of features, which transforms an orthogonal structure into a simplex ETF structure in an analogous manner.

5.2 The relationship between the MP-operator and NC

To show how the MP-operator describes NC, we first present the following proposition.

Proposition 1. *If T_{MP} is MP-operator and $\hat{f}_i(x) = \mathbf{1}_{A_i}(x)$ for a balanced partition $\{A_1, \dots, A_C\}$ of \mathcal{X} , then $\langle C\hat{f}_i | T_{MP}[C\hat{f}_j - \mathbf{1}] \rangle = a_2(\delta_{ij} - C^{-1})$ and $\langle \mathbf{1} | T_{MP}[C\hat{f}_j - \mathbf{1}] \rangle = 0$, where C is the number of classes.*

Proof See Appendix F ■

Proposition 1 follows straightforwardly from the MP operator from Definition 4. Note that the conditions for \hat{f} are met for balanced classification tasks. Importantly, if we take the data distribution q to be the empirical distribution of the training set, then \hat{f} – the label function for the training set – also fulfils the conditions for Proposition 1.

We next present two propositions showing that the MP-operator leads to the mathematical statements of NC1 (collapse of within-class variability) and NC2 (convergence of features to a rigid simplex equiangular tight frame (ETF) structure), respectively. For the two propositions below, the class feature map $h_i : \mathcal{X} \rightarrow \mathbb{R}^p$ is a feature map to the last layer features for given class i , and class mean vector $\mu_i \in \mathbb{R}^p$ is the expectation of $h_i(x)$ over A_i . The global mean vector $\mu_g \in \mathbb{R}^p$ is the average of all class means.

Proposition 2. *Let T_{MP} be MP-operator, the inputs x are taken from q the empirical distribution of the training set, and \hat{f} the empirical output function of balanced C -way classification task. The following NC1 condition holds:*

$$\text{Tr} \left(\left(\sum_i \sum_{x \in A_i} (h_i(x) - \mu_i)(h_i(x) - \mu_i)^T \right) \left(\sum_j (\mu_j - \mu_g)(\mu_j - \mu_g)^T \right)^T \right) = 0 \quad (16)$$

Proof See Appendix F ■

⁸. Unless it is centered to 0.

Proposition 3. Let T_{MP} be the MP-operator on data taken from the empirical distribution of the training set, and \hat{f} the empirical output function of balanced C -way classification task; The following NC2 condition holds:

$$(\mu_i - \mu_g)^T (\mu_j - \mu_g) \propto \delta_{ij} - \frac{1}{C} \quad (17)$$

Proof See Appendix F ■

Since Theorem 2 of [Papayan et al., 2020] states that NC3 and NC4 follow from NC1 and NC2 by using a proposition from [Webb and Lowe, 1990], the propositions above are sufficient to guarantee NC from the MP-operator. Therefore, the MP-operator from Definition 4 is a kernel that naturally leads to NC.

Note that the only challenge in proving Proposition 2 and Proposition 3 is the change of language from kernel operators into class means and global mean. The class feature map function h_i is

$$h_i(x) = \hat{f}_i(x)\Phi(x), \quad (18)$$

where $\Phi : \mathcal{X} \rightarrow \mathbb{R}^p$ is the full forward feature map and \hat{f}_i is the indicator function for class i . Using h_i for class i , the class mean of the features μ_i is

$$\mu_i = \frac{1}{A_i} \int_{\mathcal{X}} h_i(x)q'(x)dx = C \int_{\mathcal{X}} \hat{f}_i(x)\Phi(x)q'(x)dx. \quad (19)$$

and the global mean μ_g is

$$\mu_g = \frac{1}{C} \sum_i^C \mu_i = \int_{\mathcal{X}} \Phi(x)q'(x)dx, \quad (20)$$

where we have used that $\sum_i^C \hat{f}_i(x) = \mathbf{1}$. Using the definitions above, the inner products between class or global means and class functions can be expressed by T . For example,

$$\mu_i^T \mu_j = C^2 \left(\int_{\mathcal{X}} \hat{f}_i(x)\Phi(x)q'(x)dx \right)^T \int_{\mathcal{X}} \hat{f}_j(x')\Phi(x')q'(x')dx' \quad (21)$$

$$= C^2 \int_{\mathcal{X}} \hat{f}_i(x)q'(x) \int_{\mathcal{X}} \Phi(x)^T \Phi(x')\hat{f}_j(x')q'(x')dx' \quad (22)$$

$$= C^2 \int_{\mathcal{X}} \hat{f}_i(x)q'(x)T[\hat{f}_j](x)dx \quad (23)$$

$$= \langle \hat{f}_i | T[\hat{f}_j] \rangle \quad (24)$$

where we used the definition of the integral operator T (Equation (2)) in the third line.

5.3 Extending beyond NC to regression

Even though NC and the MP-operator are closely related, our use of a kernel framework means our definition can be extended to broader tasks such as regression. An MP-operator can be defined for any vector output function as long as we know the dimension of the function space spanned by its entries, which is typically just the dimension of the output vector. For example, in Figure 12, we compare a ResNet18 on MNIST trained by classification and by regression. For regression, the output function is a scalar output function $f : \mathcal{X} \rightarrow \mathbb{R}$ with the target value being the digit itself. In other words, an image x is classified as class i if $i - 0.5 < f(x) < i + 0.5$. Then as seen in Figure 12, the regression problem has reached the MF regime (except the first constant function) using only a single feature since a scalar output function requires only one linearly independent function. This is in contrast to the classification task (dashed) with vector output function $f : \mathcal{X} \rightarrow \mathbb{R}^{10}$, which is in the MF regime using 10 features. The example clearly illustrates that the dimensionality of the output function is the key factor in setting the minimal number of features, rather than the number of classes.

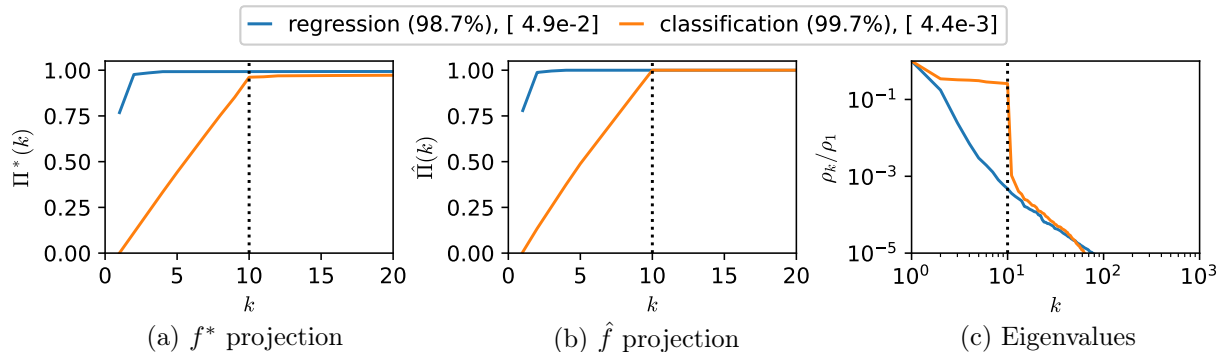


Figure 12: **MFR for regression problem with scalar output.** ResNet18 was trained on MNIST via regression (blue) and classification (orange). While regression has scalar output target function $f : \mathcal{X} \rightarrow \mathbb{R}$, classification has a 10-dimension vector output target function $f : \mathcal{X} \rightarrow \mathbb{R}^{10}$. It can be seen that both models are in the MF regime, using the minimum number of features.

6. Discussion

In this paper, we analyse feature learning by calculating, at each time step, the eigenvalues and eigenfunctions of the forward feature map Φ of a DNN, treating it as if it were a fully linear system trained via gradient descent. Since a DNN is non-linear, these eigenfunctions and eigenvalues change during training. This allows us to monitor feature learning by tracking how the eigenvalues and projections of the eigenfunctions onto both the target function f^* and the learned function f , change with time.

Our methods are computationally efficient enough to enable detailed analysis of classification tasks on standard image datasets such as MNIST, CIFAR10 and CIFAR100. We observe that, in some cases, a DNN can collapse down to a minimal feature (MF) regime in just a few epochs, consistent with the neural collapse (NC) regime typically studied at later stages of training. However, in other cases such as for an FCN on CIFAR10, we observe an extended feature (EF) regime, where the network uses significantly more than the minimal number of features. We contrast these two feature-learning regimes with the *coefficient learning regime*, in which the features remain unchanged during training, and only the coefficients of the learned function—expanded in the basis of eigenfunctions at initialization—are adjusted.

While it has long been recognized that a key factor behind the success of deep neural networks (DNNs) lies in their capacity to automatically learn features [Bengio et al., 2013; LeCun et al., 2015; Schmidhuber, 2015], the precise mechanisms by which feature learning enhances performance remains unresolved. On the one hand, because the final layer of a DNN is typically much smaller than the training set, achieving low loss or low training error requires adjusting intermediate layers—effectively, feature learning. This inherent expressivity constraint ensures that any training method capable of reaching near-zero error training error will induce feature learning. The question, then, is not whether feature learning aids generalization but what specific properties of an algorithm and data combination lead to learning features that enhance generalization performance.

If a DNN is made wider so that the expressivity constraint lifts, a second mode of achieving zero training error or low loss will emerge, characterized by coefficient learning with frozen features. In situations where both modes are possible, one can meaningfully ask whether feature learning itself leads to better performance than no feature learning. This question has been extensively explored in the infinite width limit, where NTK models do not learn features, while other infinite-width limits do [Mei et al., 2018; Rotskoff and Vanden-Eijnden, 2018; Chizat et al., 2019; Yang et al., 2021; Yang and Hu, 2021; Yang et al., 2023; Bordelon and Pehlevan, 2022, 2023]. Nevertheless, it remains unclear how relevant these studies are to more conventional narrower DNNs, where the feature learning always occurs due to expressivity constraints, and the key questions revolve around how the learned features can enhance performance. On the other hand, the more recent trend toward using much larger models [Brown, 2020; Bommasani et al., 2021] may provide a more promising context for applying insights from the infinite-width limit.

Another approach to analysing feature-learning is to move beyond the infinite-width kernel limit, for example by expanding in $1/p$ Halverson et al. [2021]; Daniel A. Roberts [2021]; Naveh and Ringel [2021]; Bordelon and Pehlevan [2023]; Seroussi et al. [2023]. While again, much progress has been made, it remains unclear whether these methods can capture the strong feature-learning behaviour observed in the MF regime

or if they are limited to describing the EF regime. It would be interesting to explore whether these expansions around the infinite width kernel limit can be connected to our kernel-based description of the pure MF/NC limit discussed in Section 5.

We used our analysis methods to examine how changing certain properties of a DNN, such as the stride in a ResNET18, batch normalisation in a VGG, or varying hyperparameters such as the learning rate or weight decay, affect feature learning as well as generalisation. While we observe that a tighter MF regime typically corresponds to better generalisation, it is no guarantee. For example, the MF regime also obtains for completely random labelling of the data, where generalisation is poor.

We also find for the example of ResNet18 on CIFAR10, that the scaling exponent of learning curves appears to increase around the training set size where the feature-learning moves from the EF regime to the MF regime. It will be interesting to study whether or not this finding is more general.

These results likely only scratch the surface of what may be more complex phenomenology. More empirical and theoretical work is needed to establish causal links between different regimes of feature learning and generalisation performance. Addressing these questions will likely require going beyond only analysing the final layer features. It is straightforward to extend our projection and effective dimension measures to probe feature-learning in intermediate layers, as was done for example in [Alain and Bengio, 2016; Montavon et al., 2011; Lou et al., 2022]. Indeed, in Appendix D we provide some preliminary examples of applying these methods to intermediate layers, which will be further developed and extended in a companion paper.

Future work will also include a more detailed exploration of other loss functions (see Figure 20) and optimisation methods. Moreover, much of the recent excitement has centered around LLMs, which differ from the ResNet18, VGG, and FCN architectures and the image datasets examined in this study. These models not only use different architectures and datasets but are also typically much wider than the simpler architectures discussed here.

Our work raises important questions about the mechanisms driving feature learning. The presence of the MF regime even with random data suggests that feature learning may be influenced more by the dynamics of training than by specific properties of the data.

Finally, a central goal of research on DNNs is to move beyond the black-box nature of these models and to understand how they make predictions. Working out how DNNs extract and process features from raw data plays a key role in this quest. While our findings demonstrate, for instance, that DNNs can reduce the number of features to a minimal set, understanding what these final-layer features capture is not straightforward. Further research is needed to distil these features into something more human-interpretable.

7. Acknowledgements

SL was supported by the National Research Foundation of Korea (NRF) grant funded by the Korean government (MSIT) (No.2020R1A5A1016126).

References

- G. Alain and Y. Bengio. Understanding intermediate layers using linear classifier probes. *arXiv preprint arXiv:1610.01644*, 2016.
- Z. Allen-Zhu and Y. Li. What can resnet learn efficiently, going beyond kernels? *Advances in Neural Information Processing Systems*, 32, 2019.
- S. Arora, S. S. Du, W. Hu, Z. Li, R. R. Salakhutdinov, and R. Wang. On exact computation with an infinitely wide neural net. In *Advances in Neural Information Processing Systems*, pages 8139–8148, 2019.
- A. Atanasov, B. Bordelon, and C. Pehlevan. Neural networks as kernel learners: The silent alignment effect. *arXiv preprint arXiv:2111.00034*, 2021.
- J. Ba, M. A. Erdogdu, T. Suzuki, Z. Wang, D. Wu, and G. Yang. High-dimensional asymptotics of feature learning: How one gradient step improves the representation. *Advances in Neural Information Processing Systems*, 35:37932–37946, 2022.
- Y. Bahri, E. Dyer, J. Kaplan, J. Lee, and U. Sharma. Explaining neural scaling laws. *arXiv preprint arXiv:2102.06701*, 2021.

- C. T. Baker and R. Taylor. The numerical treatment of integral equations. *Journal of Applied Mechanics*, 46(4):969, 1979.
- A. Baratin, T. George, C. Laurent, R. D. Hjelm, G. Lajoie, P. Vincent, and S. Lacoste-Julien. Implicit regularization via neural feature alignment. In *International Conference on Artificial Intelligence and Statistics*, pages 2269–2277. PMLR, 2021.
- E. Belilovsky, M. Eickenberg, and E. Oyallon. Greedy layerwise learning can scale to imagenet. In *International conference on machine learning*, pages 583–593. PMLR, 2019.
- Y. Bengio, A. Courville, and P. Vincent. Representation learning: A review and new perspectives. *IEEE transactions on pattern analysis and machine intelligence*, 35(8):1798–1828, 2013.
- R. Bommasani, D. A. Hudson, E. Adeli, R. Altman, S. Arora, S. von Arx, M. S. Bernstein, J. Bohg, A. Bosselut, E. Brunskill, et al. On the opportunities and risks of foundation models. *arXiv preprint arXiv:2108.07258*, 2021.
- B. Bordelon and C. Pehlevan. Self-consistent dynamical field theory of kernel evolution in wide neural networks. *Advances in Neural Information Processing Systems*, 35:32240–32256, 2022.
- B. Bordelon and C. Pehlevan. Dynamics of finite width kernel and prediction fluctuations in mean field neural networks. *arXiv preprint arXiv:2304.03408*, 2023.
- e. a. Brown, Tom B. Language models are few-shot learners. *arXiv preprint arXiv:2005.14165*, 2020.
- A. Canatar and C. Pehlevan. A kernel analysis of feature learning in deep neural networks. In *2022 58th Annual Allerton Conference on Communication, Control, and Computing (Allerton)*, pages 1–8. IEEE, 2022.
- A. Canatar, B. Bordelon, and C. Pehlevan. Spectral bias and task-model alignment explain generalization in kernel regression and infinitely wide neural networks. *Nature communications*, 12(1):2914, 2021.
- A. Caticha. The basics of information geometry. *arXiv preprint arXiv:1412.5633*, 2014.
- L. Chizat, E. Oyallon, and F. Bach. On lazy training in differentiable programming. *Advances in neural information processing systems*, 32, 2019.
- N. Cristianini, J. Shawe-Taylor, A. Elisseeff, and J. Kandola. On kernel-target alignment. *Advances in neural information processing systems*, 14, 2001.
- H. Cui, B. Loureiro, F. Krzakala, and L. Zdeborová. Generalization error rates in kernel regression: The crossover from the noiseless to noisy regime. *Advances in Neural Information Processing Systems*, 34:10131–10143, 2021.
- A. Damian, J. Lee, and M. Soltanolkotabi. Neural networks can learn representations with gradient descent. In *Conference on Learning Theory*, pages 5413–5452. PMLR, 2022.
- B. H. Daniel A. Roberts, Sho Yaida. *The Principles of Deep Learning Theory*. arXiv preprint arXiv:2106.10165, 2021.
- A. Daniely and E. Malach. Learning parities with neural networks. *Advances in Neural Information Processing Systems*, 33:20356–20365, 2020.
- J. Devlin, M.-W. Chang, K. Lee, and K. Toutanova. Bert: Pre-training of deep bidirectional transformers for language understanding. *arXiv preprint arXiv:1810.04805*, 2018.
- K. Dingle, C. Q. Camargo, and A. A. Louis. Input–output maps are strongly biased towards simple outputs. *Nature Communications*, 9(1):1–7, 2018.
- T. Galanti, Z. S. Siegel, A. Gupta, and T. Poggio. Sgd and weight decay provably induce a low-rank bias in neural networks. *arXiv preprint arXiv:2206.05794*, 2022.
- M. Geiger, S. Spigler, A. Jacot, and M. Wyart. Disentangling feature and lazy training in deep neural networks. *Journal of Statistical Mechanics: Theory and Experiment*, 2020(11):113301, 2020.

- M. Geiger, L. Petrini, and M. Wyart. Landscape and training regimes in deep learning. *Physics Reports*, 924: 1–18, 2021.
- R. Girshick, J. Donahue, T. Darrell, and J. Malik. Rich feature hierarchies for accurate object detection and semantic segmentation. In *Proceedings of the IEEE conference on computer vision and pattern recognition*, pages 580–587, 2014.
- I. Goodfellow, J. Pouget-Abadie, M. Mirza, B. Xu, D. Warde-Farley, S. Ozair, A. Courville, and Y. Bengio. Generative adversarial nets. *Advances in neural information processing systems*, 27, 2014.
- I. Goodfellow, Y. Bengio, and A. Courville. *Deep learning*. MIT press, 2016.
- F. Graetz. How to visualize convolutional features in 40 lines of code, Jan 2019. URL <https://towardsdatascience.com/how-to-visualize-convolutional-features-in-40-lines-of-code-70b7d87b0030>.
- J. Halverson, A. Maiti, and K. Stoner. Neural networks and quantum field theory. *Machine Learning: Science and Technology*, 2(3):035002, 2021.
- X. Han, V. Pappayan, and D. L. Donoho. Neural collapse under mse loss: Proximity to and dynamics on the central path. *arXiv preprint arXiv:2106.02073*, 2021.
- O. E. Harzli, G. Valle-Pérez, and A. A. Louis. Double-descent curves in neural networks: a new perspective using gaussian processes. *arXiv preprint arXiv:2102.07238*, 2021.
- K. He, X. Zhang, S. Ren, and J. Sun. Deep residual learning for image recognition. In *Proceedings of the IEEE conference on computer vision and pattern recognition*, pages 770–778, 2016.
- J. Hestness, S. Narang, N. Ardalani, G. Diamos, H. Jun, H. Kianinejad, M. Patwary, M. Ali, Y. Yang, and Y. Zhou. Deep learning scaling is predictable, empirically. *arXiv preprint arXiv:1712.00409*, 2017.
- M. O. Hill. Diversity and evenness: a unifying notation and its consequences. *Ecology*, 54(2):427–432, 1973.
- J. Hoffmann, S. Borgeaud, A. Mensch, E. Buchatskaya, T. Cai, E. Rutherford, D. d. L. Casas, L. A. Hendricks, J. Welbl, A. Clark, et al. Training compute-optimal large language models. *arXiv preprint arXiv:2203.15556*, 2022.
- L. Hui, M. Belkin, and P. Nakkiran. Limitations of neural collapse for understanding generalization in deep learning. *arXiv preprint arXiv:2202.08384*, 2022.
- A. G. Ivakhnenko and V. G. Lapa. *Cybernetic Predicting Devices*. CCM Information Corporation, 1965.
- A. Jacot, F. Gabriel, and C. Hongler. Neural tangent kernel: Convergence and generalization in neural networks. In *Advances in neural information processing systems*, pages 8571–8580, 2018.
- A. Jacot, B. Simsek, F. Spadaro, C. Hongler, and F. Gabriel. Kernel alignment risk estimator: Risk prediction from training data. *Advances in Neural Information Processing Systems*, 33:15568–15578, 2020.
- A. Jacot, E. Golikov, C. Hongler, and F. Gabriel. Feature learning in l_2 -regularized dnns: Attraction/repulsion and sparsity. *Advances in Neural Information Processing Systems*, 35:6763–6774, 2022.
- Y. Jing, Y. Yang, Z. Feng, J. Ye, Y. Yu, and M. Song. Neural style transfer: A review. *IEEE transactions on visualization and computer graphics*, 26(11):3365–3385, 2019.
- J. Kaplan, S. McCandlish, T. Henighan, T. B. Brown, B. Chess, R. Child, S. Gray, A. Radford, J. Wu, and D. Amodei. Scaling laws for neural language models. *arXiv preprint arXiv:2001.08361*, 2020.
- R. Karakida, S. Akaho, and S.-i. Amari. Pathological spectra of the fisher information metric and its variants in deep neural networks. *Neural Computation*, 33(8):2274–2307, 2021.
- D. P. Kingma and J. L. Ba. Adam: A method for stochastic optimization. In *Proc. 3rd Int. Conf. Learn. Representations*, 2014.
- S. Kornblith, M. Norouzi, H. Lee, and G. Hinton. Similarity of neural network representations revisited. In *International conference on machine learning*, pages 3519–3529. PMLR, 2019.

- V. Kothapalli, E. Rasromani, and V. Awatramani. Neural collapse: A review on modelling principles and generalization. *arXiv preprint arXiv:2206.04041*, 2022.
- A. Krizhevsky, I. Sutskever, and G. E. Hinton. Imagenet classification with deep convolutional neural networks. *Communications of the ACM*, 60(6):84–90, 2017.
- Y. LeCun, B. Boser, J. Denker, D. Henderson, R. Howard, W. Hubbard, and L. Jackel. Handwritten digit recognition with a back-propagation network. *Advances in neural information processing systems*, 2, 1989.
- Y. LeCun, Y. Bengio, and G. Hinton. Deep learning. *Nature*, 521(7553):436, 2015.
- J. Lee, J. Sohl-dickstein, J. Pennington, R. Novak, S. Schoenholz, and Y. Bahri. Deep neural networks as gaussian processes. In *International Conference on Learning Representations*, 2018. URL <https://openreview.net/forum?id=B1EA-M-OZ>.
- J. Lee, L. Xiao, S. Schoenholz, Y. Bahri, R. Novak, J. Sohl-Dickstein, and J. Pennington. Wide neural networks of any depth evolve as linear models under gradient descent. In *Advances in neural information processing systems*, pages 8572–8583, 2019.
- J. Lee, S. Schoenholz, J. Pennington, B. Adlam, L. Xiao, R. Novak, and J. Sohl-Dickstein. Finite versus infinite neural networks: an empirical study. *Advances in Neural Information Processing Systems*, 33: 15156–15172, 2020.
- Y. Lou, C. E. Mingard, and S. Hayou. Feature learning and signal propagation in deep neural networks. In *International Conference on Machine Learning*, pages 14248–14282. PMLR, 2022.
- E. Malach, P. Kamath, E. Abbe, and N. Srebro. Quantifying the benefit of using differentiable learning over tangent kernels. In *International Conference on Machine Learning*, pages 7379–7389. PMLR, 2021.
- A. G. d. G. Matthews, M. Rowland, J. Hron, R. E. Turner, and Z. Ghahramani. Gaussian process behaviour in wide deep neural networks. *arXiv preprint arXiv:1804.11271*, 2018.
- S. Mei, A. Montanari, and P.-M. Nguyen. A mean field view of the landscape of two-layer neural networks. *Proceedings of the National Academy of Sciences*, 115(33):E7665–E7671, 2018.
- C. Mingard, J. Skalse, G. Valle-Pérez, D. Martínez-Rubio, V. Mikulik, and A. A. Louis. Neural networks are a priori biased towards boolean functions with low entropy. *arXiv preprint arXiv:1909.11522*, 2019.
- C. Mingard, H. Rees, G. Valle-Pérez, and A. A. Louis. Do deep neural networks have an inbuilt occam’s razor? *arXiv preprint arXiv:2304.06670*, 2023.
- C. Molnar. *Interpretable machine learning*. Lulu. com, 2020.
- G. Montavon, M. L. Braun, and K.-R. Müller. Kernel analysis of deep networks. *Journal of Machine Learning Research*, 12(9), 2011.
- A. Mordvintsev, C. Olah, and M. Tyka. Deepdream—a code example for visualizing neural networks. *Google Research*, 2(5), 2015.
- A. Mousavi-Hosseini, S. Park, M. Girotti, I. Mitliagkas, and M. A. Erdogdu. Neural networks efficiently learn low-dimensional representations with sgd. *arXiv preprint arXiv:2209.14863*, 2022.
- P. Nakkiran, G. Kaplun, Y. Bansal, T. Yang, B. Barak, and I. Sutskever. Deep double descent: Where bigger models and more data hurt. *Journal of Statistical Mechanics: Theory and Experiment*, 2021(12):124003, 2021.
- Y. Nam, N. Fonseca, S. H. Lee, and A. Louis. An exactly solvable model for emergence and scaling laws. *arXiv preprint arXiv:2404.17563*, 2024.
- G. Naveh and Z. Ringel. A self consistent theory of gaussian processes captures feature learning effects in finite cnns. *Advances in Neural Information Processing Systems*, 34:21352–21364, 2021.
- R. M. Neal. Priors for infinite networks (tech. rep. no. crg-tr-94-1). *University of Toronto*, 1994.

- S. J. Pan and Q. Yang. A survey on transfer learning. *IEEE Transactions on knowledge and data engineering*, 22(10):1345–1359, 2009.
- V. Pappayan, X. Han, and D. L. Donoho. Prevalence of neural collapse during the terminal phase of deep learning training. *Proceedings of the National Academy of Sciences*, 117(40):24652–24663, 2020.
- A. Paszke, S. Gross, S. Chintala, G. Chanan, E. Yang, Z. DeVito, Z. Lin, A. Desmaison, L. Antiga, and A. Lerer. Automatic differentiation in pytorch. 2017.
- L. Petrini, F. Cagnetta, E. Vanden-Eijnden, and M. Wyart. Learning sparse features can lead to overfitting in neural networks. *Journal of Statistical Mechanics: Theory and Experiment*, 2023(11):114003, 2023.
- A. Radhakrishnan. Lecture 4: Nngp, dual activations, and over-parameterization, Jan 2022. URL <https://web.mit.edu/modernml/course/lectures/MLClassLecture4.pdf>.
- M. Raghu, J. Gilmer, J. Yosinski, and J. Sohl-Dickstein. Svcca: Singular vector canonical correlation analysis for deep learning dynamics and interpretability. *Advances in neural information processing systems*, 30, 2017.
- M. Refinetti, S. Goldt, F. Krzakala, and L. Zdeborová. Classifying high-dimensional gaussian mixtures: Where kernel methods fail and neural networks succeed. In *International Conference on Machine Learning*, pages 8936–8947. PMLR, 2021.
- G. M. Rotskoff and E. Vanden-Eijnden. Trainability and accuracy of neural networks: An interacting particle system approach. *arXiv preprint arXiv:1805.00915*, 2018.
- S. Santurkar, D. Tsipras, A. Ilyas, and A. Madry. How does batch normalization help optimization? *Advances in neural information processing systems*, 31, 2018.
- J. Schmidhuber. Deep learning in neural networks: An overview. *Neural networks*, 61:85–117, 2015.
- M. Seleznova, D. Weitzner, R. Giryes, G. Kutyniok, and H.-H. Chou. Neural (tangent kernel) collapse. *arXiv preprint arXiv:2305.16427*, 2023.
- I. Seroussi, G. Naveh, and Z. Ringel. Separation of scales and a thermodynamic description of feature learning in some cnns. *Nature Communications*, 14(1):908, 2023.
- J. B. Simon, M. Dickens, and M. R. DeWeese. A theory of the inductive bias and generalization of kernel regression and wide neural networks. *arXiv e-prints*, pages arXiv–2110, 2021.
- K. Simonyan and A. Zisserman. Very deep convolutional networks for large-scale image recognition. *arXiv preprint arXiv:1409.1556*, 2014.
- A. J. Smola and B. Schölkopf. On a kernel-based method for pattern recognition, regression, approximation, and operator inversion. *Algorithmica*, 22:211–231, 1998.
- S. Spigler, M. Geiger, and M. Wyart. Asymptotic learning curves of kernel methods: empirical data versus teacher–student paradigm. *Journal of Statistical Mechanics: Theory and Experiment*, 2020(12):124001, 2020.
- G. Valle-Pérez and A. A. Louis. Generalization bounds for deep learning. *arXiv preprint arXiv:2012.04115*, 2020.
- G. Valle-Pérez, C. Q. Camargo, and A. A. Louis. Deep learning generalizes because the parameter-function map is biased towards simple functions. *arXiv preprint arXiv:1805.08522*, 2018.
- A. Vaswani, N. Shazeer, N. Parmar, J. Uszkoreit, L. Jones, A. N. Gomez, Ł. Kaiser, and I. Polosukhin. Attention is all you need. *Advances in neural information processing systems*, 30, 2017.
- N. Vyas, Y. Bansal, and P. Nakkiran. Limitations of the ntk for understanding generalization in deep learning. *arXiv preprint arXiv:2206.10012*, 2022.
- N. Vyas, A. Atanasov, B. Bordelon, D. Morwani, S. Sainathan, and C. Pehlevan. Feature-learning networks are consistent across widths at realistic scales. *arXiv preprint arXiv:2305.18411*, 2023.

- A. R. Webb and D. Lowe. The optimised internal representation of multilayer classifier networks performs nonlinear discriminant analysis. *Neural Networks*, 3(4):367–375, 1990.
- K. Weiss, T. M. Khoshgoftaar, and D. Wang. A survey of transfer learning. *Journal of Big data*, 3(1):1–40, 2016.
- C. K. Williams and C. E. Rasmussen. *Gaussian processes for machine learning*, volume 2. MIT press Cambridge, MA, 2006.
- G. Yang and E. J. Hu. Tensor programs iv: Feature learning in infinite-width neural networks. In *International Conference on Machine Learning*, pages 11727–11737. PMLR, 2021.
- G. Yang, E. Hu, I. Babuschkin, S. Sidor, X. Liu, D. Farhi, N. Ryder, J. Pachocki, W. Chen, and J. Gao. Tuning large neural networks via zero-shot hyperparameter transfer. *Advances in Neural Information Processing Systems*, 34:17084–17097, 2021.
- G. Yang, J. B. Simon, and J. Bernstein. A spectral condition for feature learning. *arXiv preprint arXiv:2310.17813*, 2023.
- M. D. Zeiler and R. Fergus. Visualizing and understanding convolutional networks. In *Computer Vision—ECCV 2014: 13th European Conference, Zurich, Switzerland, September 6–12, 2014, Proceedings, Part I 13*, pages 818–833. Springer, 2014.
- Z. Zhu, T. Ding, J. Zhou, X. Li, C. You, J. Sulam, and Q. Qu. A geometric analysis of neural collapse with unconstrained features. *Advances in Neural Information Processing Systems*, 34:29820–29834, 2021.
- F. Zhuang, Z. Qi, K. Duan, D. Xi, Y. Zhu, H. Zhu, H. Xiong, and Q. He. A comprehensive survey on transfer learning. *Proceedings of the IEEE*, 109(1):43–76, 2020.

Appendix A. DNN performance for a fixed feature map as a function of width

In this section, we expand on the experiment in Figure 1(b) where we explore the width p needed for a DNN with a frozen feature map (random features) to reach (near) zero training error. We compare a CNN, ResNet18 and VGG16 on both CIFAR10 and CIFAR100. In Figure 13 we observe that to first order, a width on the order of $p \approx n$ is needed to train a CNN to zero training error on CIFAR10. To second order, this width depends on depth as well, with larger widths needed for deeper CNNs. We explore a much smaller range of widths for ResNet18 and VGG16 architectures for CIFAR10 in Figure 14, and for CIFAR100 in Figure 15. We observe that if the DNN is trained with SGD, both these architectures can reach zero training error for very narrow final layer widths p , but much larger widths are needed for DNNs with a frozen feature map.

In the main text, we did not study the effects of the widths of the intermediate layers. One could imagine the extreme case of a bottleneck layer inserted just before the penultimate layer, that would greatly reduce expressivity. Here we keep the overall width constant, but it would be interesting to vary the width of intermediate layers.

In more detail: Figure 13 shows a CNN with kernels of size 3×3 , a max-pooling layer with kernel size 2×2 , and a final linear layer on the flattened output. The output dimension is controlled by the size of this flattened output, meaning that the number of filters per layer determines p . When the last layer has $p = 90000$ for the depth 2 CNN, we have 500 filters per layer (increasing depth decreases p slightly for a fixed number of filters as the image is shrunk by 2 pixels on each dimension with each convolutional layer). Depth counts the number of matrices in the CNN (so a single convolutional layer plus the final layer has depth 2). Figure 13(a) shows that $p \sim 10^4$ is enough to fit the training data for the depth 2 and 5 models, but for depth 10 and for the maximum width, the model cannot do better than 70% train accuracy. Note also that even when 100% train accuracy can be achieved, generalisation continues to improve with increasing width for the depth 2 and 5 models. Figure 13(b) explores the generalisation error with training set size for the depth 5 model at two different widths. It illustrates how narrower frozen feature models can fit less training data to 100% accuracy, as expected.

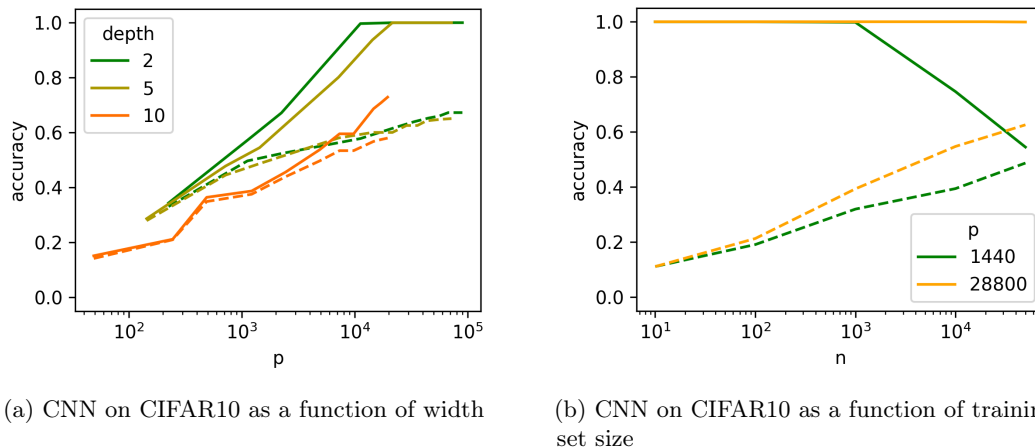


Figure 13: **CNN performance for frozen layers** (a) The training error (solid) and test error (dashed) for CNNs with a frozen feature map and different depths, trained on CIFAR10, as a function of the intermediate/last layer widths p . The training set size is fixed at the standard $n = 50000$. (b) Training error (solid) and test error (dashed) for a 5-layer CNN with widths $p = 1440$ and $p = 28800$, trained on different training set sizes n . Note that to first order, the training error reaches zero for widths on the order of the training set size for this data set.

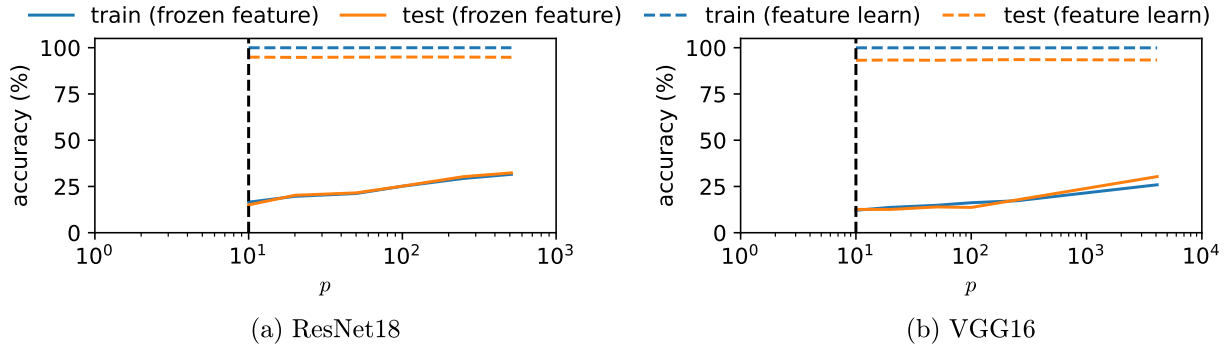


Figure 14: **Performance by the width of the input for the last layer for CIFAR10** Two widely used models (a) ResNet18 and (b) VGG16 are trained on CIFAR10 with two different methods. The models were trained with SGD, allowing full feature learning (solid), or trained with all layers except the last layer fixed. Performance is plotted across various widths of the last layer, sampled between its original width and $C = 10$. First, we observe that feature learning models outperform last layer-only trained models by a significant margin. Furthermore, the performance of feature learning models remains independent of the width of the last layer, in contrast to the correlation observed in last layer-only trained DNNs.

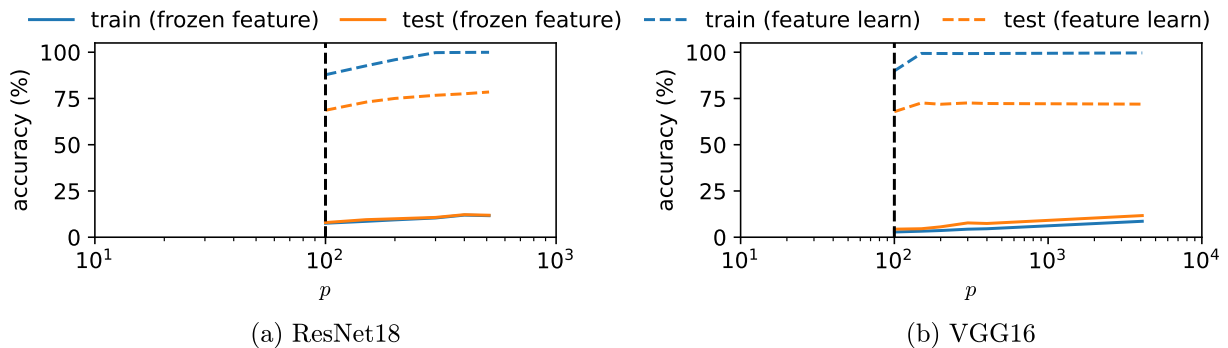


Figure 15: **Performance by the width of the input for the last layer for ResNet18 and VGG16 on CIFAR100** (a) ResNet18 and (b) VGG16 on CIFAR100. Similar results are obtained in Figure 14, but the performance of feature learning models now changes more with the width than it does for CIFAR10. This difference can be attributed to the difficulty that intermediate layers face in learning features for a more challenging task.

Appendix B. On the definition of features

In the main text, we defined the eigenfunctions, $e_k(x)$, and eigenvalues, ρ_k , of the operator $T[f](x')$. How do these eigenfunctions relate to the basis functions $\phi_k(x)$? One way one can rewrite $f(x) = \sum_{k=1}^p \theta_k \Phi_k(x)$ in $|e_k\rangle$ is as:

$$f(x) = \sum_{j=1}^{j=p} \theta_j \left[\frac{1}{\sqrt{\rho_k}} \int dx' q(x') \Phi_j(x') e_k(x') \right]_{jk} \sqrt{\rho_k} |e_k\rangle, \quad (25)$$

Where U_{jk} will denote the matrix in the square brackets. We note that the rows of U can be written as $\sqrt{\rho_i} e_i(x) = (U_i)_j \Phi_j(x) = U_i^T \Phi(x)$, meaning

$$\delta_{ij} = \int e_i(x) e_j(x) q(x) dx = (U_i)^T \sqrt{\frac{\rho_j}{\rho_i}} \left[\frac{1}{\sqrt{\rho_j}} \int \Phi(x) e_j(x) q(x) dx \right] = \sqrt{\frac{\rho_j}{\rho_i}} (U_i)^T (U_j), \quad (26)$$

demonstrating that $U^T U = U U^T = I$, and thus U is orthogonal. This argument shows that

$$f(x) = \sum_{k=1}^p [U_{kj} \theta_j] [\sqrt{\rho_k} e_k(x)]$$

where U preserves the norm of θ . This would mean the norm of a perturbation $\|\Delta\theta\|_2 = \|\Delta\theta'\|_2$ where $\theta' = U\theta$. This fact means gradient descent on θ' would find the same solutions as on θ . For more information on the importance of model parameterisation, see e.g. [Caticha, 2014]. Given this property, it would arguably be desirable to call $\sqrt{\rho_k} e_k(x)$ the features, as we could write $f(x) = \sum_{k=1}^p \theta'_k z_k$ where the features $z_k = \sqrt{\rho_k} e_k(x)$.

Furthermore, when the model is overparameterised, the solution found is strongly influenced by ρ_k – so incorporating ρ_k into the definition of features would mean two models with the same features would always find the same solutions. It would be entirely consistent to call features $\sqrt{\rho_k} |e_k\rangle$, and then study its two components separately. However, one could also argue that as the eigenfunctions $e_k(x)$ are correctly normalized, it would not make sense to call features rescaled eigenfunctions – two models with the same $e_k(x)$ but different eigenvalues ρ_k, ρ'_k would disagree on how much the k 'th feature is present in the input. This also seems undesirable.

As a result of these issues, and given that our measures use the correctly normalized $e_k(x)$, or ρ_k separately, we find it easier to call $|e_k\rangle$ the features and ρ_k the associated eigenvalue.

It is also worth briefly discussing exactly how the eigenfunctions $e_k(x)$ relate to more intuitive pictures of features – as abstract properties of the input (for example, the edge of an object, or the object itself, in image data). It has been shown in e.g. [Krizhevsky et al., 2017] that early layers of CNNs do indeed pick up on edges, and later layers pick up on more abstract features (like chain links) [Graetz, 2019]. It is at present less clear how to make similar interpretations of our final layer features. Future work on intermediate layer features (see also Appendix D) may help bring some insight, however.

Appendix C. Further Experiments

In this section, we present a series of further experiments that complement various points made in the main text.

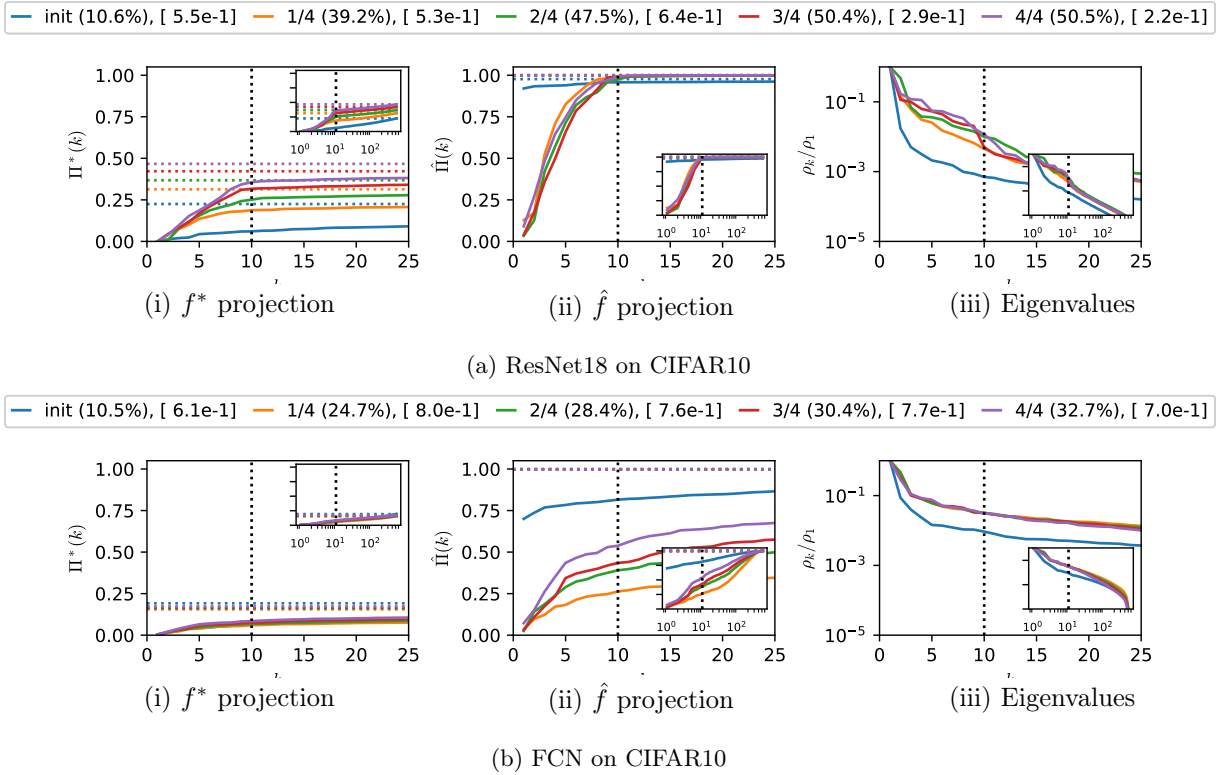


Figure 16: **Feature learning during the first epoch** This figure depicts our measures of feature-learning during the first epoch of the experiment in Figure 5 where we compare a ResNet18 and an FCN, both trained on CIFAR10. The fractions denote the fraction of the first epoch (so 1/4 means 1/4 of the total iterations in the first epoch were complete). The batch size was 512, so each quarter is about 25 iterations. For both the ResNet18, which eventually converges to the MF regime, and the FCN, which converges to the EF regime, we observe that the largest relative change happens within the first 1/4 epoch. Insets are the same data but for the full set of $k = 512$ features.

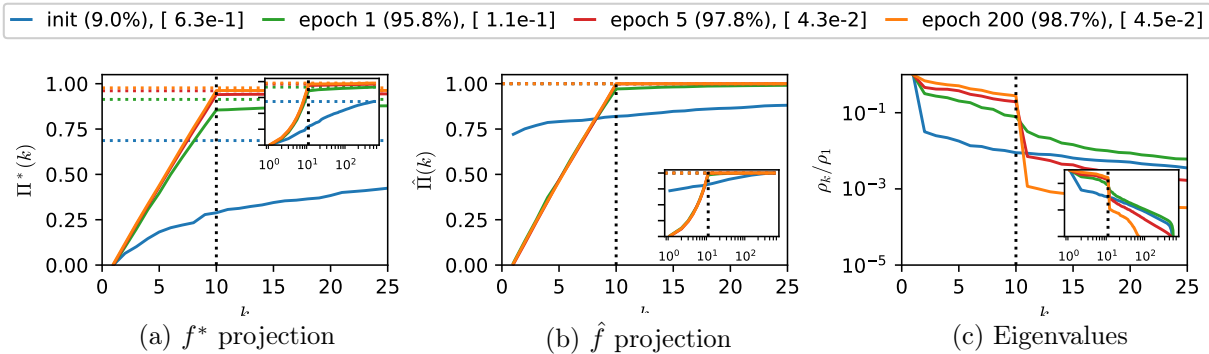


Figure 17: **FCN on MNIST quickly converges to the MF regime** Here we trained a 4-layer ReLU activated FCN on MNIST to demonstrate that MF regime can be (rapidly) achieved for this architecture, in fact, it is almost fully in the MF regime according to the κ_{CKA} criterion after just one epoch. This behaviour is in contrast to what we demonstrate in Figure 5(b), where the same FCN remains in the EF regime at convergence when trained on CIFAR10. The insets show the data for the full range of k .

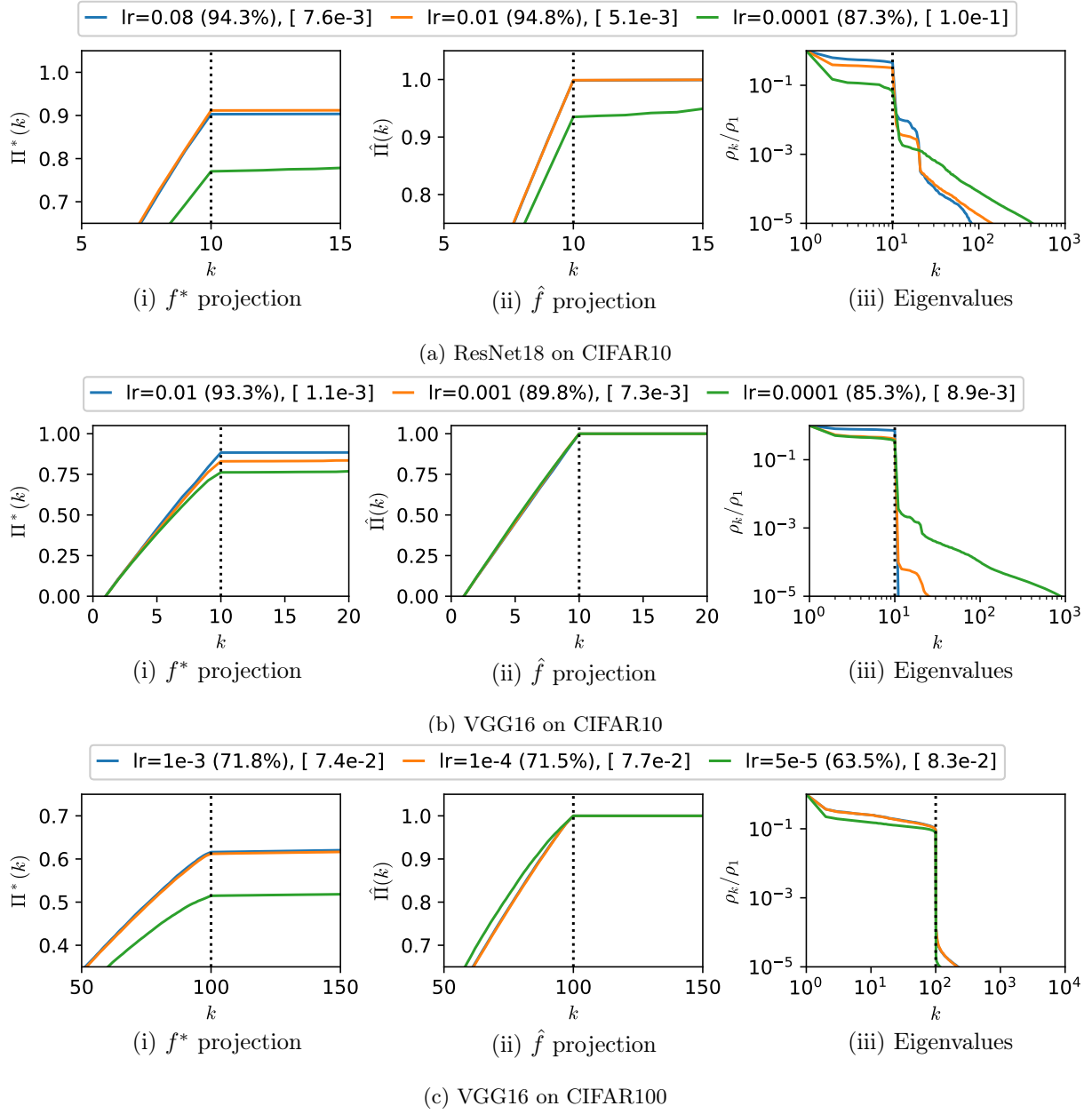
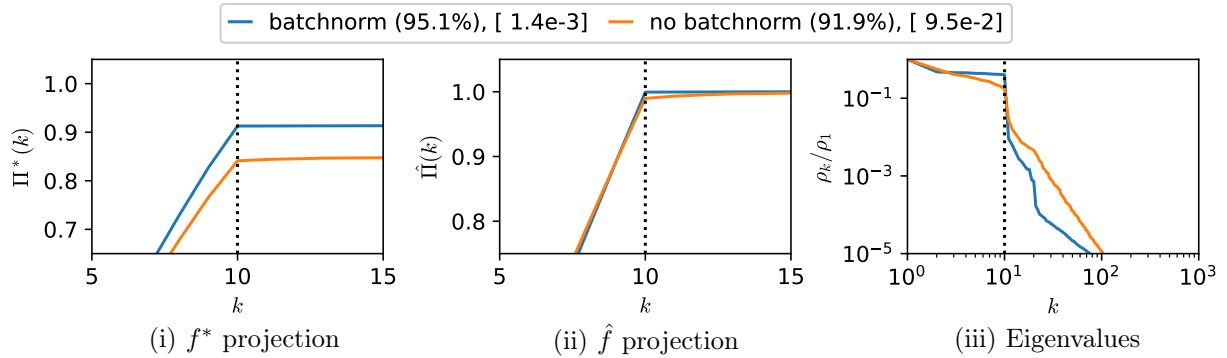
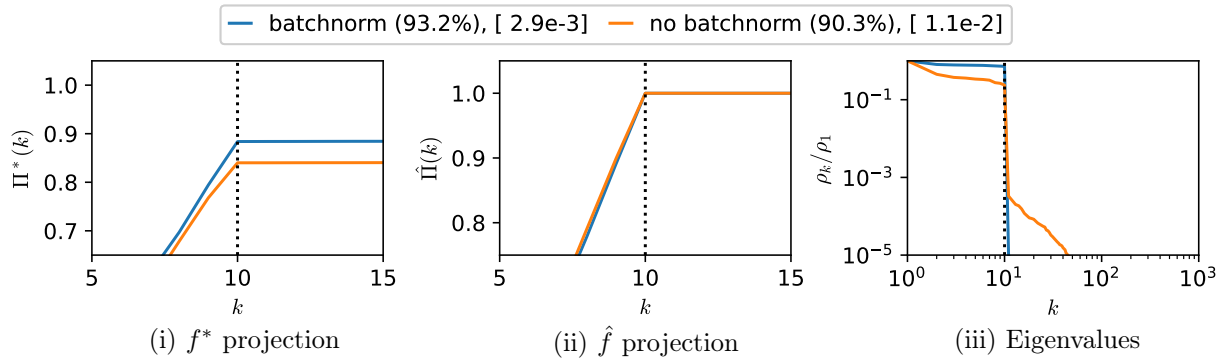


Figure 18: **Further examples comparing learning rates** The top legend shows the learning rate, (test accuracy), and $[\kappa_{CKA}]$. In support of what we find in Section 4, a stricter MF regime characterised by a smaller κ_{CKA} , a flatter ρ_k for $2 \leq k \leq C$, and larger eigenvalue gap at $k = C$ correlates with better performance for all these examples.



(a) WideResNet18 on CIFAR10



(b) VGG16 on CIFAR10

Figure 19: **Effect of batch normalization on feature learning** The top legend shows batch normalization (test accuracy) and $[\kappa_{CKA}]$. Batch normalization leads to flatter ρ_k for $2 \leq k \leq C$, a larger eigenvalue gap at $k = C$, and better performance. Note that the effect of batch normalization for VGG on CIFAR100, shown in the main text, is much more dramatic than the smaller effects shown here.

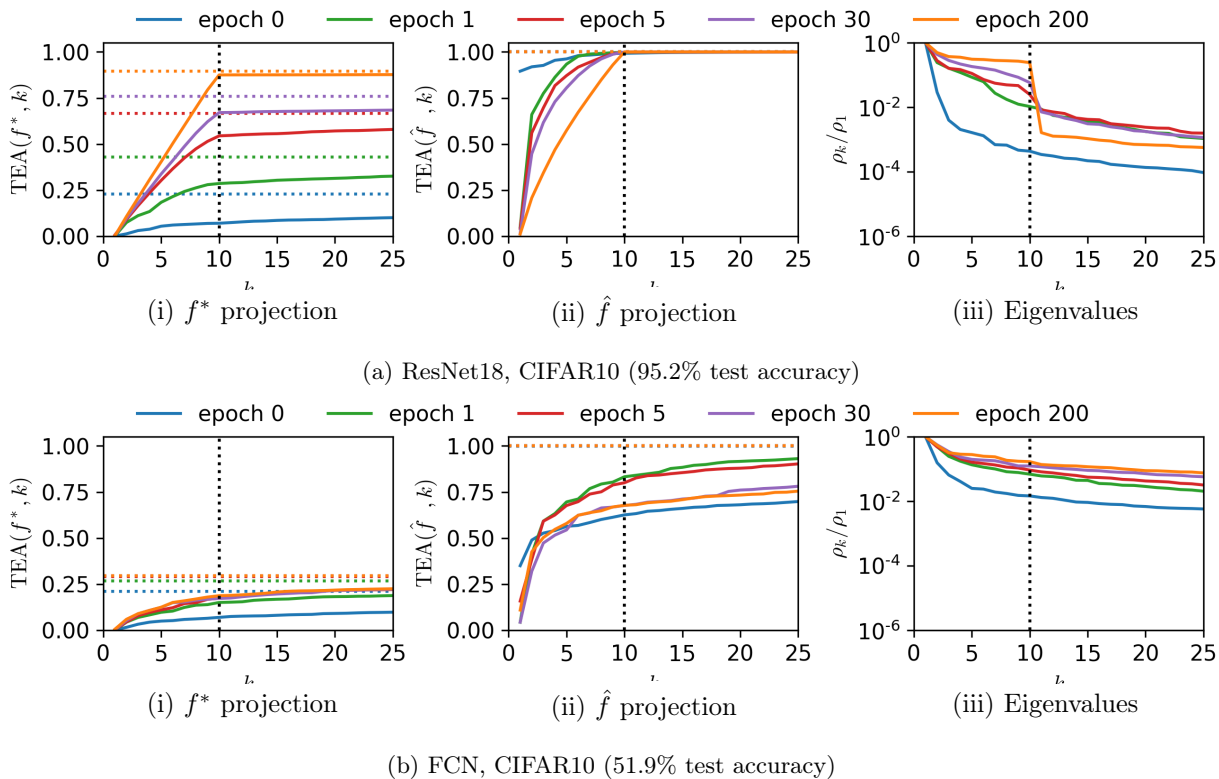


Figure 20: **Training with cross-entropy loss** This figure is equivalent to Figure 5, with (a) a ResNet18 and (b) an FCN trained on CIFAR10, but instead of MSE, we trained with CE loss. The qualitative behaviour closely follows that of Figure 5 with a few notable differences. (a) The discrepancy in the speed of alignment for $k \leq C$ compared to $k > C$ is more significant, with small k features aligning considerably faster. (b) For the FCN, the eigenvalue gap at $k = C$ at epoch 200 has disappeared.

Appendix D. Intermediate layer features

In the main text, we only study the final layer features. Analysing the middle layers is necessary for a complete understanding of feature learning. This appendix shows how we can straightforwardly apply measures outlined in Section 2, and discusses the problems with doing this. See e.g. [Alain and Bengio, 2016; Montavon et al., 2011; Lou et al., 2022] for related work.

Intermediate layers have an intermediate feature map in the same way the last layer does. The feature map of the l 'th layer is $\Phi^{(l)} : \mathcal{X} \rightarrow \mathbb{R}^{p_l}$, where p_l is the number of features for layer l . This induces a feature kernel for the l 'th layer, $\Phi^{(l)}(x)^T \Phi^{(l)}(x')$. Its eigenvalues, eigenfunctions and all projection measures in Section 2 can be defined in exactly the same way that they are for the last layer. When the output of the feature map $\Phi^{(l)}$ is multidimensional (e.g. the output from a 2D convolutional module), the output is flattened to a vector (similarly to [Montavon et al., 2011; Alain and Bengio, 2016; Raghu et al., 2017]).

The interpretation of $\Phi^{(l)}$ as an intermediate feature map and measuring its change with training to monitor feature learning in intermediate layers is straightforward. We use the measures Π^* and $\hat{\Pi}$, which capture how aligned a layer is to the target function and learned function respectively. It is straightforward to simply consider these as probes that help quantify the amount of feature learning that occurs under training. However, more care is needed in their direct interpretation. In contrast to the final-layer features these layers are not used to directly produce measured output, but rather are fed into the next layer. If well-trained early layers are strongly aligned to the final target, that may not be a good thing. We illustrate this in Figure 21 where a greedy layerwise training method leads to stronger alignment in earlier layers, but less good performance than normal SGD with backpropagation for a ResNet18 on CIFAR10.

In more detail, to generate Figure 21, we use a version of greedy layerwise training [Ivakhnenko and Lapa, 1965]. We append an auxiliary classification layer to the first layer, training that system, before removing the auxiliary layer, freezing the first layer, and repeating the process with the second layer. Even though it is sometimes possible to achieve near-SOTA accuracies with such a method [Belilovsky et al., 2019], the greedy layerwise training typically leads to worse performance than full backpropagation. In Figure 21(a), the layerwise training generates significantly greater alignment $\Pi^*(k)$ at lower k in layers 1 and 2, compared to full backpropagation. However, the feature quality does not continue to improve in layers 3 and 4, and $\Pi^*(p)$ for the last layer is significantly lower than for backpropagation. In Figure 21(b) we observe that layerwise training, compared to backpropagation, has a larger increment of $\hat{\Pi}(k)$ for the first 3 layers, but a negligible difference between the 4th and the last layer. In addition, both systems are very close to the full MF regime. This is another example where the MF regime holds for two training methods, but performance varies significantly, as discussed in Section 4.1. Finally, in Figure 21(c), we observe that the eigenvalue spectrum reflects how the standard backpropagation training only produces a clear MF regime structure in the final layer. In contrast, greedy training produces a more MF regime-like pattern in earlier layers, as all intermediate layers are treated as penultimate layers in the training process.

We also study the effect of batchnorm on the intermediate layer features in Figure 22 for two cases where it makes a big difference to generalisation performance. Subfigure (a) shows VGG16 on Cifar100 and (b) ResNet18 on Cifar100. In both cases, early layers barely align to the target function without batchnorm and perform significantly worse than the case with batch norm. This provides an example of how intermediate layers help diagnose the causes of the reduced performance. We leave further experiments and analysis to future work, including an upcoming companion paper on intermediate features.

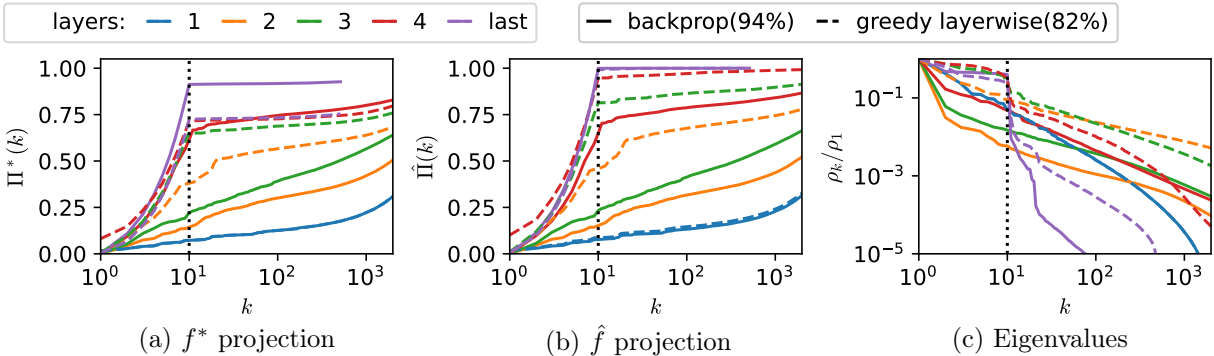


Figure 21: **Greedy layerwise training leads to a collapse of features in earlier layers.** In contrast to full backpropagation (solid), greedy layerwise training (dashed) leads to more pronounced alignment at lower k for earlier layers, as seen, for example in the value of $\Pi^*(C)$ for layers 2 and 3 in (a). However, there is only a minute enhancement in $\Pi^*(k)$ for subsequent layers for greedy layerwise training, leading to final poorer quality features compared to that of full backpropagation. Note that the difference in $\Pi^*(C)$ for the final layer directly correlates with the performance as both models are in a tight MF regime as seen in (b). Note that $\hat{P}i(k)$ of the last layer is almost identical for both models (purple solid and dashed lines in (b)). Similarly, at layers 3 and 4, the intermediate layer eigenvalues for greedy layerwise training in (c) are more MF regime-like with a larger gap between ρ_C and ρ_{C+1} . This is quantified in $D_{eff}(\rho)$ as 348 vs. 608 for layer 3 and 90.4 vs. 279 for layer 4 for layerwise training and full backpropagation, respectively.

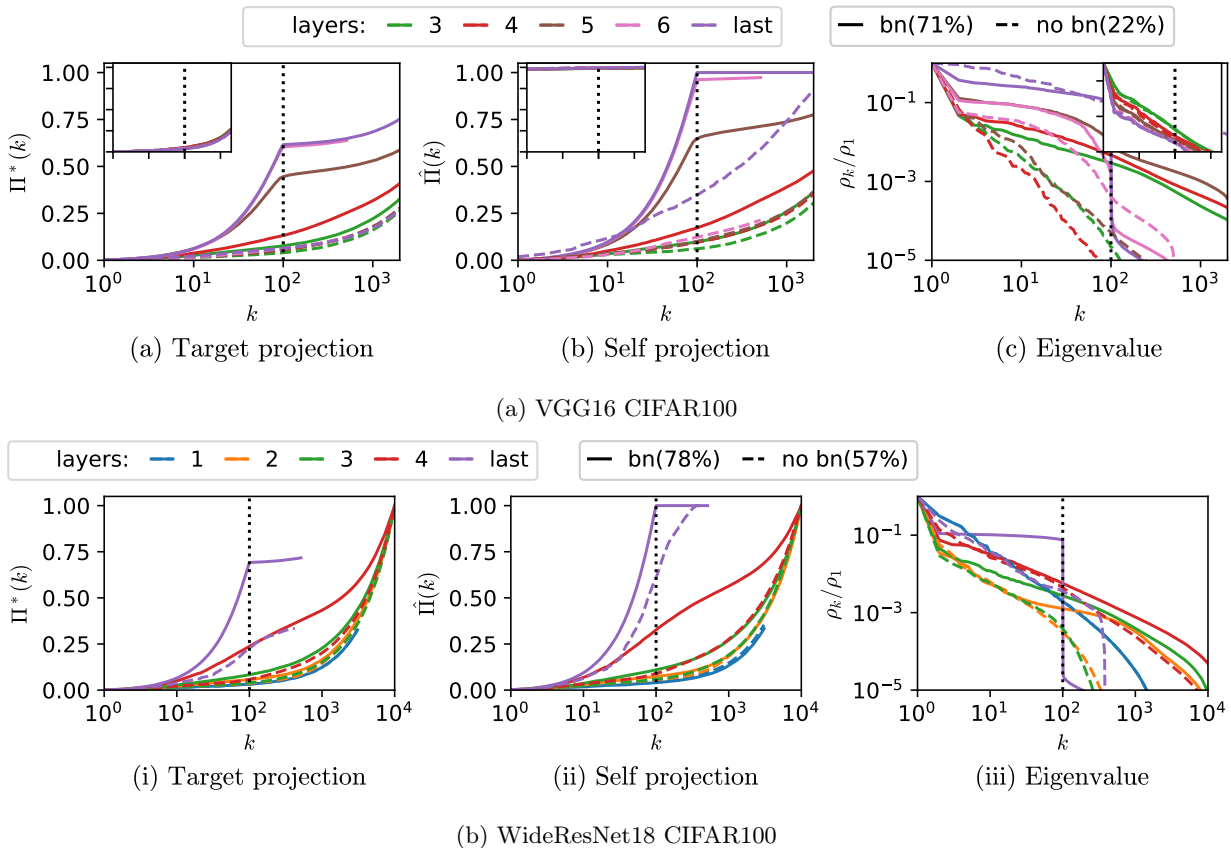


Figure 22: **Effect of batch normalization in CIFAR100.** We clearly observe more alignment in the intermediate layers, and the performance boost is more dramatic (22% to 72% for (a), 47% to 78% for (b)). Moreover, without batch normalization, neither model achieved over 99% training accuracy in 600 epochs, unlike other experiments in the paper. In this case, training was instead halted at 94% after 1200 epochs. (c) The key distinction lies in the eigenvalues, where the decay rate was slowed down after the application of batch normalization.

Appendix E. Two lemmas

In this section, we provide the proofs of two lemmas that are used in the main text. Throughout, we assume an infinite number of data and the following MSE loss.

$$\mathbf{L} = \int_{\mathcal{X}} (f(x) - f^*(x))^2 q(x) dx \quad (27)$$

Lemma 1. *The Gradient Flow (GF) dynamics of a linear model of the following form $f(x) = \sum_{i=1}^p \theta_i \Phi_i(x)$ is diagonalized into the following p independent equations:*

$$\langle f|e_k \rangle (t) = \langle f^*|e_k \rangle (1 - e^{-\eta \rho_k t}), \quad (28)$$

where ρ_k and e_k are the eigenvalues and eigenfunctions of the intergral operator T (Equation (2)), and η is the learning rate.

Proof By using the gradient descent equation ($\frac{d\theta_i}{dt} = -\eta \frac{d\mathbf{L}}{d\theta_i}$), we can write the change of f as

$$\frac{df}{dt}(x') = \sum_i^p \frac{d\theta_i}{dt} \Phi_i(x') = \sum_i^p -\eta \frac{d\mathbf{L}}{d\theta_i} \Phi_i(x') \quad (29)$$

$$= -2\eta \int_{\mathcal{X}} (f(x) - f^*(x)) \sum_i^p \frac{df}{d\theta_i}(x) q(x) dx \Phi_i(x') \quad (30)$$

$$= -2\eta \int_{\mathcal{X}} (f(x) - f^*(x)) \sum_i^p \Phi_i(x) \Phi_i(x') q(x) dx \quad (31)$$

$$= -2\eta T[f - f^*](x') \quad (32)$$

The equation mimics the form of a matrix differential equation. If we take the inner product of both sides with e_k ,

$$\frac{d\langle e_k|f \rangle}{dt} = -2\eta \langle e_k|T[f - f^*] \rangle \quad (33)$$

$$= -2\eta \rho_k (\langle e_k|f \rangle - \langle e_k|f^* \rangle), \quad (34)$$

where we used that fact that T is symmetric operator and $T[e_k] = \rho_k e_k$. Solving the differential equation for $\langle e_k|f \rangle$ with initial condition of $\langle e_k|f \rangle(0) = 0$ leads to

$$\langle f|e_k \rangle (t) = \langle f^*|e_k \rangle (1 - e^{-\eta \rho_k t}). \quad (35)$$

■

Lemma 2. *When $T = T_{MP}$ for a DNN, there is one-to-one mapping between $\Phi(x)$ and $\hat{f}(x)$ on the support of q .*

Proof The MP operator, by definition, maps from the expressed function space $\hat{\mathcal{H}}$ to $\hat{\mathcal{H}}$. The entries of the feature map $[\Phi_1, \dots, \Phi_p]$ span $\hat{\mathcal{H}}$, and entries of the expressed function $([\hat{f}_1, \dots, \hat{f}_C])$, by definition, also span $\hat{\mathcal{H}}$. Since $\Phi(x)$ and $\hat{f}(x)$ are related by a linear transform – ignoring the bias term as constant function is in $\hat{\mathcal{H}}$ – the map between $\Phi(x)$ and $\hat{f}(x)$ is one-to-one.

Assuming our input x is a discrete random variable, $\Phi(x)$ and $\hat{f}(x)$ are also discrete random variables. The one-to-one relationship then is sufficient to prove that mutual information between two random variables is 0 (i.e. $I(\Phi(x); \hat{f}(x)) = 0$). ■

Appendix F. Proofs related to Neural Collapse

In this section, we state the relevant terms and the four NC conditions given in [Han et al., 2021]. Please note that the current study assumes column-vectors for all vectors (e.g. $\mu_i \in \mathbb{R}^{p \times 1}$). The last layer can be defined in the following manner

$$\hat{f}_i(x) = w_i^T \Phi(x) + b_i \quad (36)$$

where $w_i \in \mathbb{R}^{p \times 1}$ is the parameter of the last that projects the feature onto the i^{th} entry of the output function. $b_i \in \mathbb{R}$ is the corresponding bias term. The feature class mean or the mean of features with label i is

$$\mu_i = \frac{C}{n} \sum_{x^{(j)} \in A_i} \Phi(x^{(j)}). \quad (37)$$

The global mean is

$$\mu_g = \frac{1}{C} \sum_i \mu_i. \quad (38)$$

The feature within-class covariance $\Sigma_W \in \mathbb{R}^{p \times p}$ is

$$\Sigma_W := \frac{1}{n} \sum_i^C \sum_{x^{(j)} \in A_i} (h_i(x^{(j)}) - \mu_i)(h_i(x^{(j)}) - \mu_i)^T. \quad (39)$$

The feature between-class covariance $\Sigma_b \in \mathbb{R}^{p \times p}$ is

$$\Sigma_b := \frac{1}{C} \sum_i^C (\mu_i - \mu_g)(\mu_i - \mu_g)^T. \quad (40)$$

The four NC conditions are the following Papyan et al. [2020]:

1. **Within class variance tends to 0**

$$\Sigma_W \Sigma_b^T \rightarrow 0 \quad (41)$$

2. **Convergence to simplex ETF**

$$\frac{(\mu_i - \mu_g)^T (\mu_j - \mu_g)}{\|(\mu_i - \mu_g)\|_2 \|(\mu_j - \mu_g)\|_2} \rightarrow \frac{C \delta_{ij} - 1}{C - 1} \quad (42)$$

3. **Convergence to self duality**

$$\frac{w_i}{\|w_i\|_2} - \frac{\mu_i - \mu_g}{\|(\mu_i - \mu_g)\|_2} \rightarrow 0 \quad (43)$$

4. **Simplification to nearest class center**

$$\arg \max_i w_i \Phi(x) + b_i \rightarrow \arg \min_i \|\Phi(x) - \mu_i\|_2 \quad (44)$$

Proposition 1. *If T_{MP} is MP-operator and $\hat{f}_i(x) = \mathbf{1}_{A_i}(x)$ for a balanced partition $\{A_1, \dots, A_C\}$ of \mathcal{X} , then $\langle C \hat{f}_i | T_{MP} [C \hat{f}_j - \mathbf{1}] \rangle = a_2 (\delta_{ij} - C^{-1})$ and $\langle \mathbf{1} | T_{MP} [C \hat{f}_j - \mathbf{1}] \rangle = 0$, where C is the number of classes.*

Proof By the definition of indicator functions of equal partitions,

$$\langle \hat{f}_i | \hat{f}_j \rangle = \frac{1}{C} \delta_{ij}, \quad \sum_i^C \hat{f}_i = \mathbf{1}, \quad \langle \mathbf{1} | \hat{f}_j \rangle = \frac{1}{C} \quad (45)$$

Since $C \hat{f}_j - \mathbf{1}$ is orthogonal to $\mathbf{1}$,

$$T_{MP} [C \hat{f}_j - \mathbf{1}] = a_2 (C \hat{f}_j - \mathbf{1}) \quad (46)$$

where we used the definition of MP operators Equation (13). Then from Equation (45) and Equation (46),

$$\langle C \hat{f}_i | T_{MP} [C \hat{f}_j - \mathbf{1}] \rangle = a_2 \langle C \hat{f}_i | C \hat{f}_j - \mathbf{1} \rangle = a_2 (C \delta_{ij} - 1) \quad (47)$$

Likewise,

$$\langle \mathbf{1} | T_{MP} [C \hat{f}_j - \mathbf{1}] \rangle = a_2 \langle \mathbf{1} | C \hat{f}_j - \mathbf{1} \rangle = 0. \quad (48)$$

■

Proposition 3. Let T_{MP} be the MP-operator on data taken from the empirical distribution of the training set, and \hat{f} the empirical output function of balanced C -way classification task; The following NC2 condition holds:

$$(\mu_i - \mu_g)^T (\mu_j - \mu_g) \propto \delta_{ij} - \frac{1}{C} \quad (17)$$

Proof From the translation of class mean function Equation (21),

$$\mu_i^T \mu_j = C^2 \left(\int_{\mathcal{X}} \hat{f}_i(x) \Phi(x) q(x) dx \right)^T \int_{\mathcal{X}} \hat{f}_j(x') \Phi(x') q(x') dx' \quad (49)$$

$$= C^2 \int_{\mathcal{X}} \hat{f}_i(x) q(x) \int_{\mathcal{X}} \Phi(x)^T \Phi(x') \hat{f}_j(x') q(x') dx' dx \quad (50)$$

$$= C^2 \int_{\mathcal{X}} \hat{f}_i(x) q(x) T[\hat{f}_j](x) dx \quad (51)$$

$$= C^2 \langle \hat{f}_i, T[\hat{f}_j] \rangle. \quad (52)$$

Likewise, using Equation (20), we get

$$\mu_i^T \mu_g = C \left(\int_{\mathcal{X}} \hat{f}_i(x) \Phi(x) q(x) dx \right)^T \int_{\mathcal{X}} \Phi(x') q(x') dx' \quad (53)$$

$$= C \int_{\mathcal{X}} \hat{f}_i(x) q(x) \int_{\mathcal{X}} \Phi(x)^T \Phi(x') q(x') dx' dx \quad (54)$$

$$= C \int_{\mathcal{X}} \hat{f}_i(x) q(x) T[\mathbf{1}](x) dx \quad (55)$$

$$= C \langle \hat{f}_i, T[\mathbf{1}] \rangle. \quad (56)$$

Then

$$(\mu_i - \mu_g)^T (\mu_j - \mu_g) = \langle C \hat{f}_i - \mathbf{1}, T[C \hat{f}_j - \mathbf{1}] \rangle \quad (57)$$

$$= C a_2 \left(\delta_{ij} - \frac{1}{C} \right) \quad (58)$$

which is the NC2 condition, where we used Equation (49) and Equation (53) in the first line and Proposition 1 in the second line. \blacksquare

Proposition 2. Let T_{MP} be MP-operator, the inputs x are taken from q' the empirical distribution of the training set, and \hat{f} the empirical output function of balanced C -way classification task. The following NC1 condition holds:

$$Tr \left(\left(\sum_i \sum_{x \in A_i} (h_i(x) - \mu_i)(h_i(x) - \mu_i)^T \right) \left(\sum_j (\mu_j - \mu_g)(\mu_j - \mu_g)^T \right)^T \right) = 0 \quad (16)$$

Proof Using the condition that \mathcal{X} is the training set, and q is its empirical distribution, and \hat{f} a class indicator function, we obtain

$$\begin{aligned} NC1 &= Tr \left(\sum_i \sum_{x \in A_i} (h_i(x) - \mu_i)(h_i(x) - \mu_i)^T \sum_j (\mu_j - \mu_g)(\mu_j - \mu_g)^T \right) \\ &= \sum_{i,j} \sum_{x \in A_i} Tr \left(((\Phi(x) - \mu_i)^T (\mu_j - \mu_g))^2 \right) \\ &= \sum_{i,j} \int_{\mathcal{X}} \hat{f}_i(x) \left((\hat{f}_i(x) \Phi(x) - \mu_i)^T (\mu_j - \mu_g) \right)^2 q(x) dx \\ &= \sum_{i,j} \int_{\mathcal{X}} \hat{f}_i(x) \left((\Phi(x) - \mu_i)^T (\mu_j - \mu_g) \right)^2 q(x) dx \end{aligned} \quad (59)$$

where we have used the fact that \hat{f}_i are indicator functions for class i in line 2, 3, and 4. From Equation (49) and Equation (53),

$$\mu_i^T(\mu_j - \mu_g) = \langle C\hat{f}_i | T[C\hat{f}_j - \mathbf{1}] \rangle \quad (60)$$

and from Equation (21) and Equation (20)

$$\Phi(x)^T(\mu_j - \mu_g) = T[C\hat{f}_j - \mathbf{1}](x). \quad (61)$$

Applying Proposition 1 into the two equations above, we obtain

$$(\Phi(x) - \mu_i)^T(\mu_j - \mu_g) = a_2 C(\hat{f}_j(x) - \delta_{ij}). \quad (62)$$

Plugging Equation (62) into Equation (59), we obtain

$$NC1 = a_2^2 C^2 \sum_{i,j} \int_{\mathcal{X}} \hat{f}_i(x) (\hat{f}_j(x) - \delta_{ij})^2 q(x) dx \quad (63)$$

$$= a_2^2 C^2 \sum_{i,j} \int_{\mathcal{X}} \hat{f}_i(x) (\hat{f}_j(x)(1 - 2\delta_{ij}) + \delta_{ij}) q(x) dx \quad (64)$$

$$= a_2^2 C \sum_{i,j} (\delta_{ij}(2 - 2\delta_{ij})) \quad (65)$$

$$= 0 \quad (66)$$

where in the third line, we used $\langle \hat{f}_i | \hat{f}_j \rangle = \delta_{ij} C^{-1}$ and $\langle \hat{f}_i | \mathbf{1} \rangle = C^{-1}$. ■

Appendix G. Experimental details

G.1 Architecture details

$k \times k$ Conv($\cdot, \cdot, \cdot, \cdot$) refers to the 2d convolutional module with a kernel of size $k \times k$, and arguments within parenthesis refer to the input channel, output channel, stride, and padding respectively. Linear(\cdot, \cdot) refers to the fully connected module with the arguments referring to input width and output width respectively. MaxPool(\cdot, \cdot, \cdot) refers to max pooling with the arguments as kernel size, stride, and padding respectively. Adaptive Avgpool(\cdot, \cdot) refers to adaptive average pooling where arguments are the size of the image after pooling. The curved arrow refers to the skip connection (identity), and any modules that appear in the arrow are applied. BN refers to batch normalization and (BN, ReLU) refers to the application of batch normalization and ReLU in respective order. The definition of the term “layer” for each model is also provided.

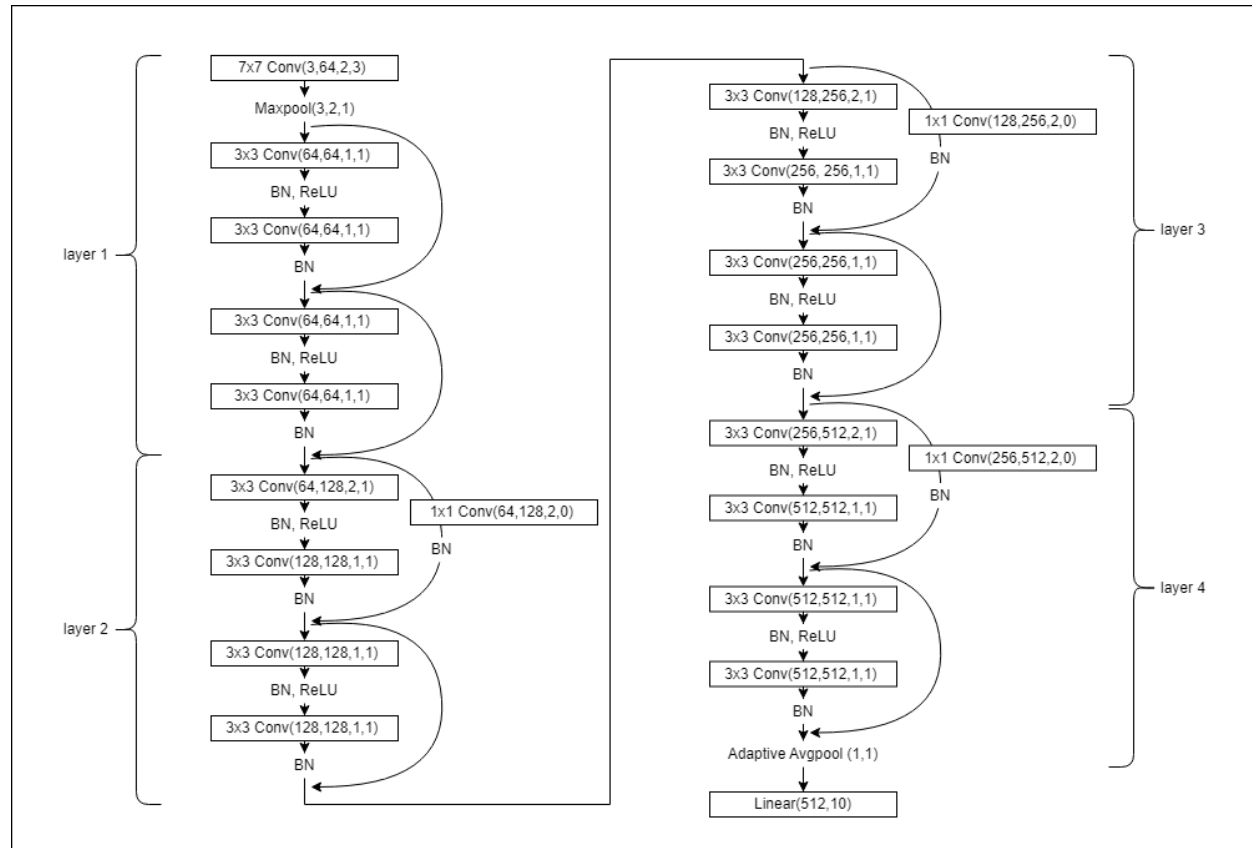


Figure 23: **ResNet18 architecture with max pooling** This is the ResNet proposed in [He et al., 2016]. The size of feature space(post-activation) for each layer is 4096, 2048, 1024, and 512 respectively. When the initial stride is decreased to 1 (i.e. 7×7 conv(3,64,1,3) for the initial convolution module), the feature space size increases to 16832, 8192, 4096, 512 respectively. The architecture was used in Figure 8, Figure 7, Figure 9(b).

G.2 Learning rate and hyperparameters

In our experiments, unless explicitly stated, SGD with a momentum of 0.9 and weight decay of 0.001 was used. Adam [Kingma and Ba, 2014] was used when the model did not converge with SGD. All models were trained for 200, 400, or 600 epochs: the earliest epoch that achieves above 99% training accuracy. For models trained for 200 epochs, a scheduler with 0.2 decay for every 60 epochs was used. For models that require 400 or more epochs, the scheduler was removed. If the model did not converge in 600 epochs or achieve below 99% training accuracy, it would be explicitly mentioned.

CIFAR10 and CIFAR100 were normalized to the mean of (0.4914, 0.4822, 0.4465) and standard deviation of (0.2023, 0.1994, 0.2010). For data augmentation, a random crop of 32 with padding of 4 and a random horizontal flip was used. No augmentation or whitening was applied to the MNIST dataset.

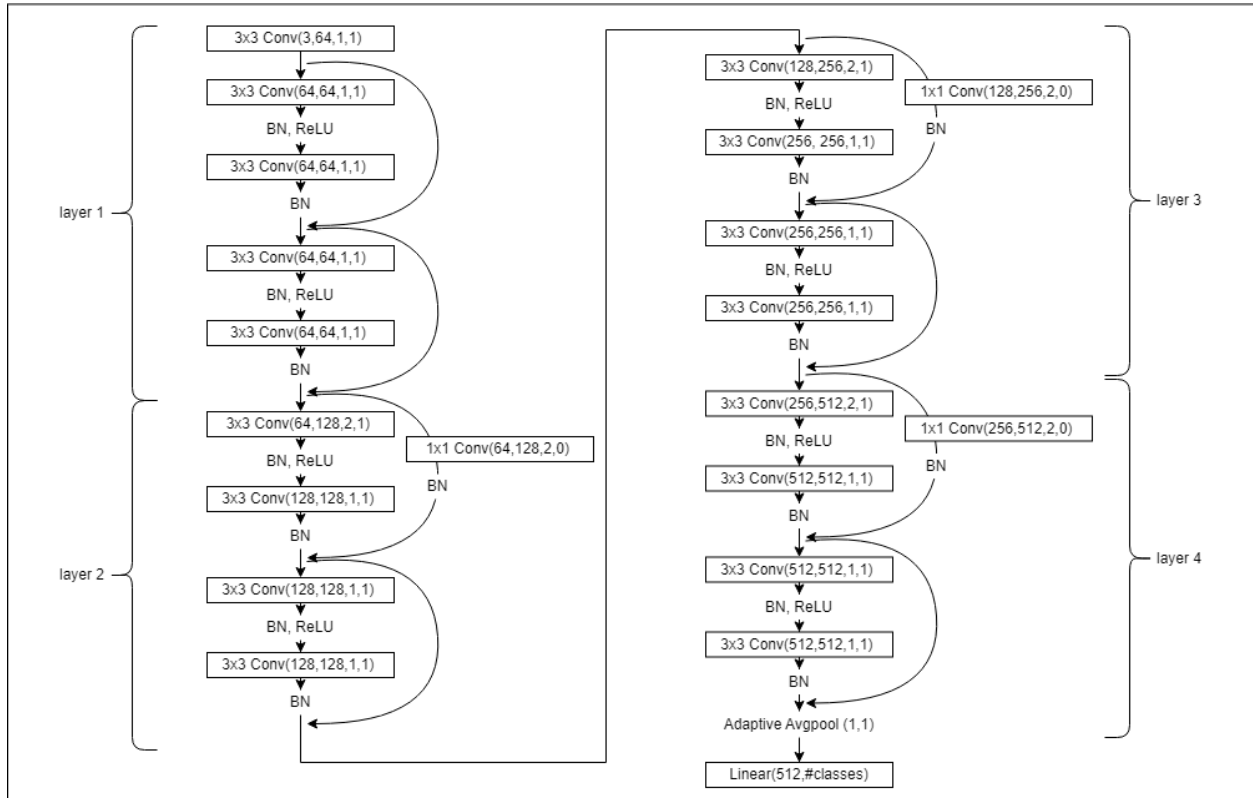


Figure 24: **ResNet18 architecture without max pooling** The architecture is similar to Figure 23 but lacks a max pooling module and has a smaller stride in the initial convolution module; The feature space is larger with the size of 65536, 32768, 16384, and 512. The architecture was used in Figure 5(a), Figure 9(a), Figure 10(a), Figure 10(c), and Figure 12.

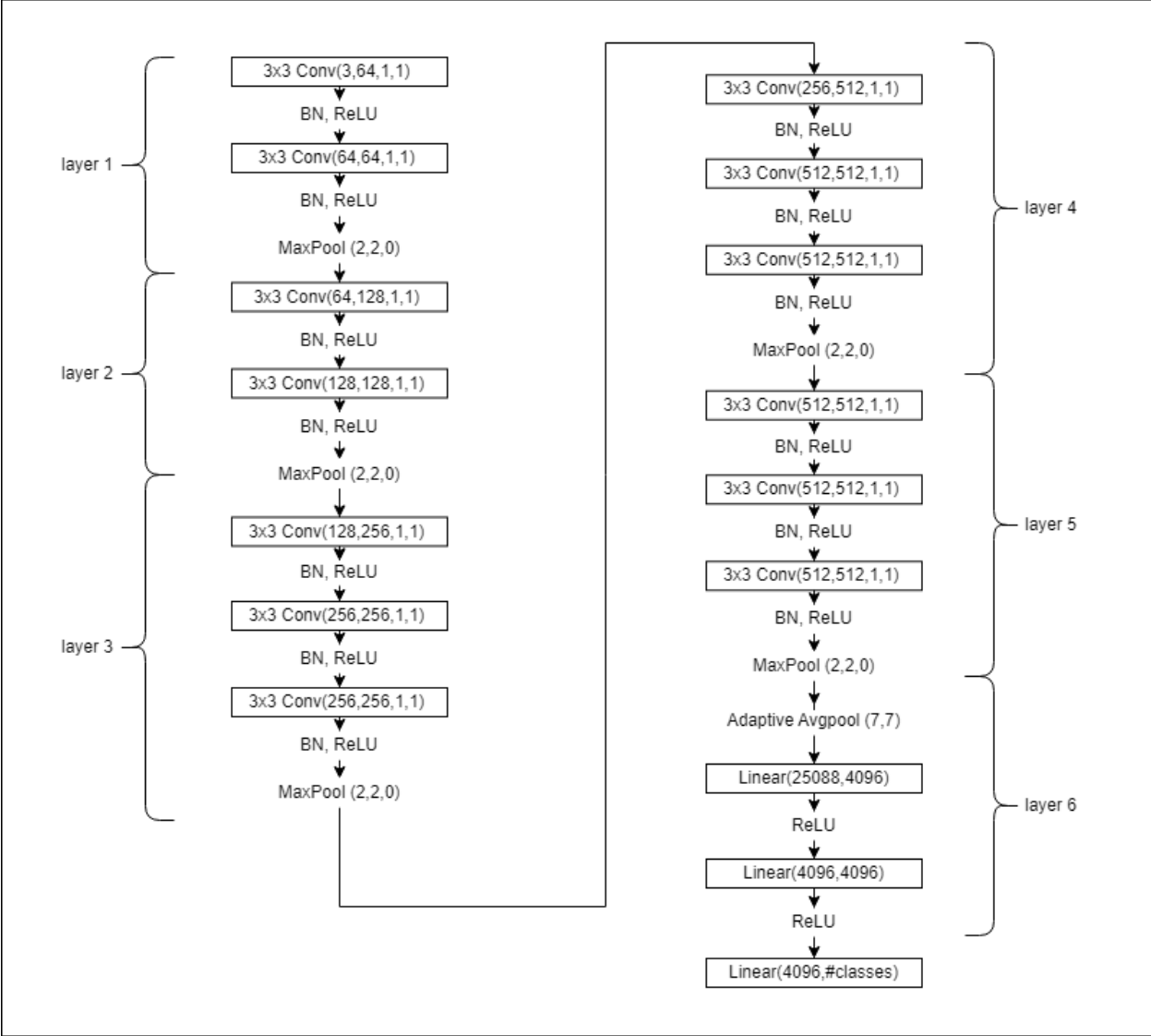


Figure 25: **VGG16 Architecture** The model has been segmented into layers by maxpooling. The feature space size for each layer is 16384, 8192, 4096, 2048, 512, and 4096. Note that the penultimate layer only consists of linear modules (fully connected) and non-linearities. The architecture was used in Figure 10(b)

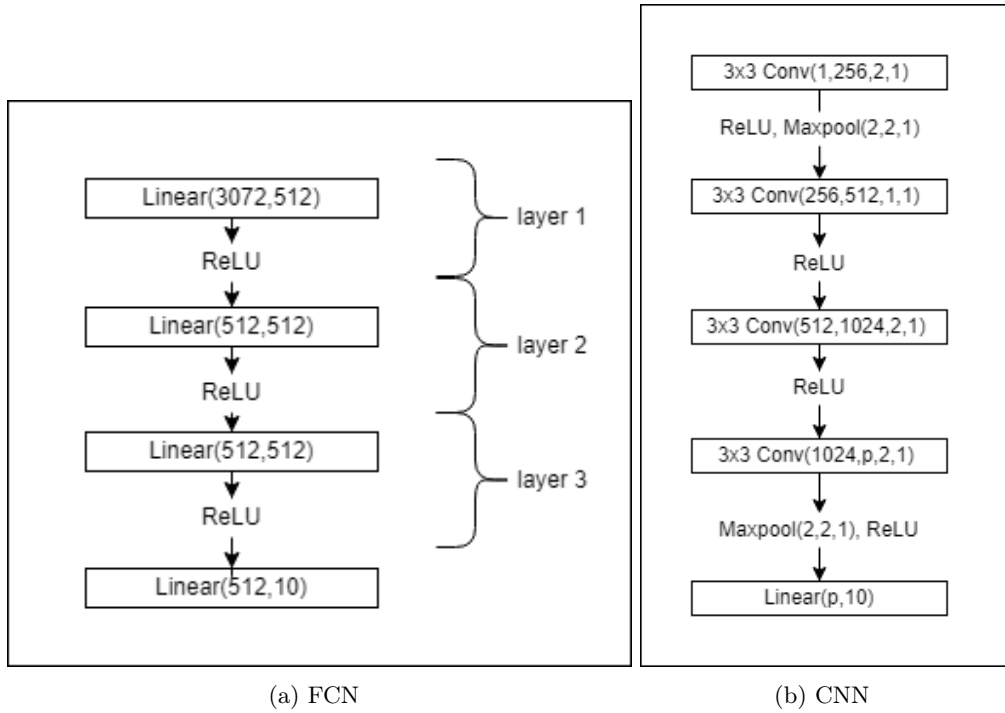


Figure 26: **FCN and CNN architecture** (a) FCN architecture used in Figure 5(b). A similar variant was used in Figure 2, Figure 6. For Figure 6, all widths were decreased to 200. (b) The CNN architecture used in Figure 3.

G.3 Loss

We use MSE loss with a centered one-hot vector (i.e. $\sum_i^C f_i^*(x) = 0$ for all $x \in \mathcal{X}$) as the C dimensional target function $f^* : \mathcal{X} \rightarrow \mathbb{R}^C$. Before centering, we have scaled the f^* by a factor of 3 for CIFAR10 and MNIST; and by 10 for CIFAR100.

Appendix H. Accuracy of approximation methods

In the main text, we proposed three main measures of features: quality Q^* , utility \hat{Q} , and eigenvalues (or intensity) ρ . These measures require the true input distribution q , which we cannot access in practice. The approximation method for these measures was described in Section 2.5 – the Nyström method for approximating e_k and the Riemann sum for the inner product in q . In this section, we use empirical methods - where the true eigenfunctions and eigenvalues are known- to assess the validity of Nyström method in approximating eigenvalues and eigenfunctions. We also discuss why quality and utility were presented in a cumulative manner (Π^* and $\hat{\Pi}$) while the eigenvalues (ρ_k) are presented directly.

H.1 The Nyström method

As discussed in Section 2.5, the Nyström method diagonalizes the empirical feature matrix $\Phi(X) \in \mathbb{R}^{p \times n}$ to approximate the eigenfunctions e_k and eigenvalues ρ_k . This is more explicitly written in lines 6 and 7 of Algorithm 1:

$$\rho_k \leftarrow s_k^2, \quad e_k(x) \leftarrow u_k^T \Phi(x) / s_k, \quad (67)$$

where u and s are the left orthogonal matrix and singular values obtained from singular value decomposition of $\Phi(X)$.

H.1.1 EXPERIMENT SETUP FOR TESTING NYSTRÖM METHOD

The accuracy of the Nyström method depends on the accuracy of singular values (s_k) and left eigenvectors (u_k) of a random matrix ($\Phi(X)$). To empirically assess the accuracy of the method, we will use p independent Gaussian random variables to sample our feature matrix. A power-law distribution with exponent α will be used as the eigenvalues:

$$\Phi_k(x) \sim \sqrt{\rho_k} \mathcal{N}(0, 1), \quad \rho_k = k^{-\alpha}. \quad (68)$$

Gaussian random variables serve as valid features since the features are random variables - $x \sim q$ is a random variable, and e_k is a fixed map, thus $e_k(x)$, $x \sim q$ is also a random variable - and are orthogonal to other eigenfunctions:

$$e_k(x) : Z_k \sim \mathcal{N}(0, 1), \quad \langle e_i | e_j \rangle = \frac{1}{2\pi} \int_{Z_i, Z_j} Z_i Z_j e^{-\frac{1}{2}(Z_i^2 + Z_j^2)} dZ_i dZ_j = \delta_{ij}. \quad (69)$$

Eigenfunctions can also be expressed with Φ as

$$e_k(x) = o_k^T \Phi(x) / \sqrt{\rho_k} \quad (70)$$

where $o_k \in \mathbf{p}$ is one-hot vector with its k^{th} entry equal to 1 and all other entries 0 (i.e. $o_k = [0, \dots, 0, 1, 0, \dots, 0]$). Indeed we can check that e_k is the eigenfunction of T with eigenvalue ρ_k

$$T\left[\frac{o_k^T \Phi(x)}{\sqrt{\rho_k}}\right] = \int \Phi(x')^T \Phi(x) \frac{o_k^T \Phi(x)}{\sqrt{\rho_k}} q(x) dx \quad (71)$$

$$= \Phi(x')^T \int Z_k^2 \sqrt{\frac{\rho_k}{2\pi}} e^{-\frac{Z_k^2}{2}} dZ_k \quad (72)$$

$$= \sqrt{\rho_k} \Phi(x')^T o_k \quad (73)$$

$$= \rho_k e_k, \quad (74)$$

where in the second line, we used that o_k^T is a one-hot vector.

H.1.2 ACCURACY MEASURES

With the underlying true features and eigenvalues defined, we propose measures for calculating the accuracy of approximated values obtained via Algorithm 1.

The error of eigenvalue is measured as square distance between ρ_k (true value) and $s_k^2(X)$ (approximation) normalized by ρ_k :

$$\mathbb{E}_X \left[\frac{(s_k^2(X) - \rho_k)^2}{\rho_k^2} \right], \quad (75)$$

Note that $\mathbb{E}_X[\cdot]$ means expectation over all possible features matrices $\Phi(X)$.

The error of eigenfunction is measured as 1 minus the inner product between $u_k(X) \in \mathbb{R}^p$ and o_k :

$$1 - \mathbf{E}_X [|u_k^T o_k|]. \quad (76)$$

The inner product $u_k^T o_k$ is proportional to the inner product between e_k^{approx} and e_k :

$$\langle e_k^{approx}, e_k \rangle = \int \left(\frac{u_k(X)^T \Phi(x)}{s_k(X)} \right)^T \frac{o_k^T \Phi(x)}{\sqrt{\rho_k}} q(x) dx \quad (77)$$

$$= \frac{u_k(X)^T}{s_k(X)} \int \Phi(x)^T \Phi(x) q(x) dx \frac{o_k}{\sqrt{\rho_k}} \quad (78)$$

$$= \frac{u_k(X)^T}{s_k(X)} \text{Diag}(\rho_k) \frac{o_k}{\sqrt{\rho_k}} \quad (79)$$

$$= \frac{u_k(X)^T o_k}{s_k(X) \sqrt{\rho_k}}, \quad (80)$$

where the denominator is not of interest as we are not particularly interested in the norm of the e_k^{approx} .

H.1.3 RESULTS

In Figure 27 we generate a feature matrix containing $n = 10,000$ datapoints and $p = 1000$ features with Gaussian random variables. We use the Nyström method to approximate the eigenvalues and eigenfunctions and assess their accuracy with the metrics in Equation (75) and Equation (76). We observe in Figure 27(a) that eigenvalues are approximated precisely except for eigenvalues with $k \approx p$. In Figure 27(b), we observe that the accuracy of the eigenfunctions correlates with the respective eigenvalues: the larger the eigenvalue (compared to the median eigenvalue), the better the accuracy. In the main text, we are often interested only in the first few eigenfunctions with large eigenvalues; We can conclude that the Nyström method is sufficiently accurate for our needs.

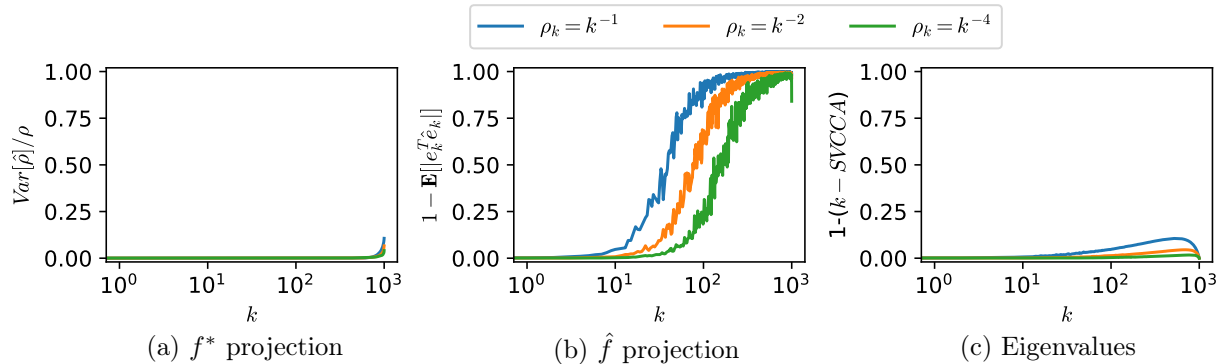


Figure 27: **Nyström approximation for different eigenvalue distributions** A feature matrix was sampled from Gaussian random variables and then approximated with Nyström method. Power law eigenvalue spectra with different decaying exponents were tested. (a) The eigenvalues are accurately predicted except for the tail eigenvalues with $k \approx p$. (b) The eigenfunctions are accurate only when the eigenvalues are large compared to the median eigenvalue. (c) The function space error below 0.25 for all k .

H.2 Function space approximation

The Nyström method’s prediction accuracy degrades for smaller eigenvalues. The spanned space of $[e_1^{approx}, \dots, e_k^{approx}]$, however, often accurately approximates that of $[e_1, \dots, e_k]$; The larger error of the e_k^{approx} is often due to the cumulation of error in predicting $e_{i < k}^{approx}$. Figure 28 illustrates an example where $[u_1, u_2, u_3]$ span the same space as $[o_1, o_2, o_3]$, and u_1 and u_2 (thus e_1 and e_2) are well approximated – the errors in predicting u_1 and u_2 accumulate to the error of predicting u_3 , and results in a poorer approximation for u_3 .

We can use the Gaussian random variable setup to check the error of the function space approximation. To measure the similarity between $span([e_1, \dots, e_k])$ and approximated function space $[e_1^{approx}, \dots, e_k^{approx}]$,

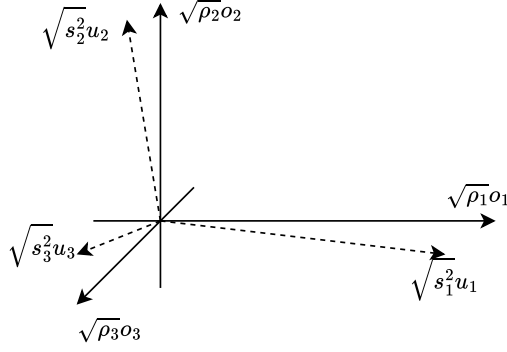


Figure 28: **Approximation on different eigenvalue distributions ...**

we can use k-SVCCA [Raghu et al., 2017] or the cumulative projection measure in Equation (9).

$$\frac{1}{k} \sum_{i=1}^k \sum_{j=1}^k \langle e_i | e_j^{approx} \rangle^2. \quad (81)$$

Since we can express the inner product between true and approximated eigenfunctions with u_k and o_k (Equation (77)), we can express the metric in terms of u_k and o_k :

$$1 - \frac{1}{k} \sum_{i=1}^k \sum_{j=1}^k (u_i^T o_j)^2, \quad (82)$$

where we subtracted the measure from 1 so the measure will be 0 when there is no error. In Figure 27(c), we observe that the function space can be approximated more accurately in comparison to individual eigenfunctions in Figure 27(b); This is why we often present the quality and utility in cumulative measure Π^* or $\hat{\Pi}$.

H.3 Error in projection measures

We now discuss the error in the projection measures like Π^* . The projection measure (Equation (7)) consists of the sum of squares of inner products between eigenfunctions and function of interest (target or expressed). The Riemann sum over the **test** set approximates the inner product – similar to how test loss approximates generalization loss.

$$\frac{\langle e_k, f_j \rangle^2}{\|e_k\|_2^2 \|f_j\|_2^2} = \frac{(\int_{\mathcal{X}} e_k(x) f_j(x) q(x) dx)^2}{\int_{\mathcal{X}} e_k(x)^2 q(x) dx \int_{\mathcal{X}} f_j(x)^2 q(x) dx} \approx \frac{(\sum_{x^{(i)} \in S_{te}} e_k(x^{(i)}) f_j(x^{(i)}))^2}{\sum_{x^{(i)} \in S_{te}} e_k(x^{(i)})^2 \sum_{x^{(i)} \in S_{te}} f_j(x^{(i)})^2}. \quad (83)$$

Using the Riemann sum, we can measure the correlation between spanned spaces (Equation (9)). Using the vector representation of eigenfunction in the test set $e_i^{approx}(X_{test}) \in \mathbb{R}^{n_{test}}$ and the vector representation of function of interest $f_i(X_{test})$, we can approximate Equation (9) as

$$\sum_{j=1}^C \sum_{i=1}^p \langle e_i | f_j \rangle^2 \approx \text{Tr}(EF^T F E^T) \quad , E_{ij} = \frac{e_i^{approx}(x^{(j)})}{\sum_j^n E_{ij}^2}, \quad F_{ij} = \frac{f_i(x^{(j)})}{\sum_j^n F_{ij}^2}. \quad (84)$$

where $x^{(j)}$ are iterated over the test set. If the rows of $E \in \mathbb{R}^{p \times n_{test}}$ and $F \in \mathbb{R}^{C \times n_{test}}$ are orthogonal, then Equation (84) is smaller than equal to 1: consistent with the definition of Equation (9).

However, Equation (84) is susceptible to error when: rows of E are not orthogonal and when $p \approx n_{test}$. We will discuss how we handled such problems in the paper.

H.3.1 NON ORTHOGONAL EIGENFUNCTIONS

As discussed earlier, approximated eigenfunctions are less accurate when their eigenvalues are smaller; they may not even be orthogonal in q or the empirical distribution of the test set. The inner product between two

approximated eigenfunctions is

$$\langle e_i^{approx} | e_j^{approx} \rangle = \frac{1}{s_i s_j} \int_{\mathcal{X}} u_i^T \Phi(x) \Phi^T(x) u_j q(x) dx \quad (85)$$

$$= \frac{1}{s_i s_j} u_i^T \left(\int_{\mathcal{X}} \Phi(x) \Phi^T(x) q(x) dx \right) u_j \quad (86)$$

$$= \frac{1}{s_i s_j} u_i^T J u_j, \quad (87)$$

where the Fisher information matrix $J \in \mathbb{R}^{p \times p}$ [Karakida et al., 2021] is defined as $\int_{\mathcal{X}} \Phi(x) \Phi^T(x) q(x) dx$. Equation (85) equals Kronecker delta if only if $[u_1, \dots, u_p]$ are the eigenvectors of J with eigenvalues $[s_1^2, \dots, s_p^2]$. Since we obtained u_i from the empirical feature matrix of the training set, the approximated eigenfunctions, especially those with small eigenvalues, are often not orthogonal in q (and in the test set).

To handle such an issue, we use QR decomposition on $E = [e_1^{approx}(X_{test}), \dots, e_p^{approx}(X_{test})] \in \mathbb{R}^{p \times n_{test}}$ before applying Equation (84): because QR decomposition orthogonalizes the rows; preserves the span of the first k vectors; handles overlapping vector between rows by conserving larger eigenvalue eigenvectors (eigenfunctions) - which are more accurate.

In Figure 29, we plot the cumulative measure with and without QR decomposition for ResNet18 on CIFAR10. We observe that Π^* and $\hat{\Pi}$ grow beyond 1 without QR decomposition, indicating that approximated eigenfunctions are not orthogonal; The inconsistent behaviour is removed when QR decomposition is applied. Note that the deviation between QR and no-QR plots emerges when the eigenvalues are sufficiently small (larger error in approximating the eigenfunction).

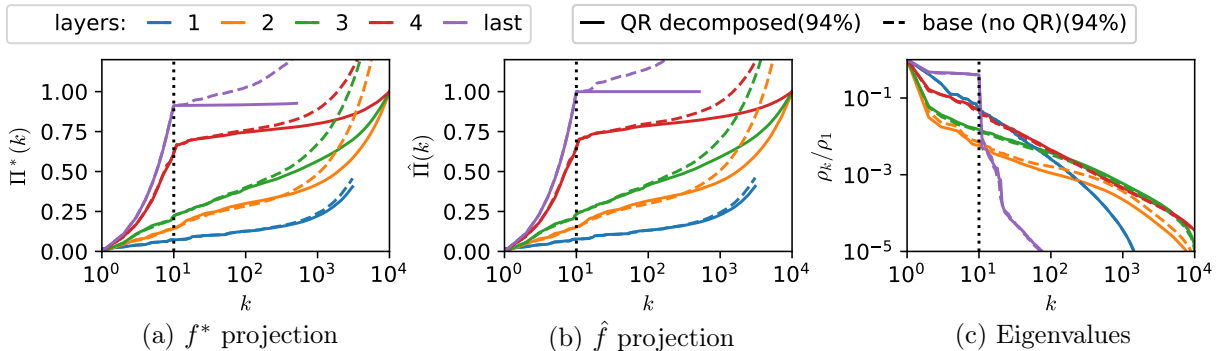


Figure 29: **Comparing approximation methods for the projection measures** ResNet18 on CIFAR10. For (a) and (b), the measures are calculated with – solid – and without – dashed – QR-composition. Note that QR decomposition removes the inconsistent behaviour of the cumulative projection measures (e.g. larger than 1). With QR decomposition, the projection measure for layers with $p \geq 10^4$ consistently equals 1 when $k = n_{test} = 10^4$.

H.3.2 FINITE SIZE EFFECT

For two sets of basis functions, increasing the number of bases to a large but finite value does not guarantee any overlap between the two function spaces: because functions are infinite-dimensional vectors. This is not the case for two finite-dimensional matrices: If $p = n_{test}$ in Equation (84) and E has full rank, then any F will be spanned by the rows of E .

In Figure 29(a,b), we observe that $\Pi^*(n_{test})$ and $\hat{\Pi}(n_{test})$ are equal to 1 for layers with $p > n_{test}$. This does not indicate that intermediate features can express the target/expressed function; It is achieved because n_{test} orthogonal vectors (E) can always span n_{test} dimensional vector space (and thus the row space of F).